Studies on droplet-microcantilever platform under fluid flow in mini wind tunnel

Keshava Praveena Neriya Hegade

A Thesis in the Department Of
Mechanical, Industrial and Aerospace Engineering

Presented in Partial Fulfilment of the Requirements for the Degree
of Master of Applied Science (Mechanical Engineering) at
Concordia University Montreal, Quebec, Canada

August 2018

CONCORDIA UNIVERSITY
School of graduate Studies

This is to certify that thesis prepared,

By: **KESHAVA PRAVEENA NERIYA HEGADE**

Entitled: **Studies on droplet-microcantilever platform under fluid flow in mini wind tunnel**

and submitted in the partial fulfilment of the requirements for the degree of

Master of Applied Science (Mechanical and Industrial Engineering)

Compiles with the regulation of the university and meets the accepted standards with respect to originality and quality.

Signed by final examining committee:

Dr. Charles Basenga Kiyanda	Chair
Dr. Javad Dargahi	Examiner
Dr. Xiaolie Wang	External to the department
Dr. Rama. B. Bhat	Co-supervisor
Dr. Muthukumaran Packirisamy	Co- supervisor

Approved by _____
Graduate Program Director

_____
Dean of Faculty

Date _____

ABSTRACT

Studies on droplet-microcantilever platform under fluid flow in mini wind tunnel

Keshava Praveena Neriya Hegade

Fluid interaction of micro structures find numerous applications in bio medical field. This thesis consists of experimental studies on fluid interaction of micro structures under laminar flow using a mini wind tunnel. The interaction of microstructures such as micro cantilever and oil coated water droplet with fluid flow were tested and the experimental results are reported. A mini wind tunnel to test microstructures is designed and built. Design of the mini wind tunnel is validated by performing tip deflection studies of micro cantilever beams of different sizes in millimeter range. The interaction of micro cantilever beam with fluid flow is recorded using a recording camera. An image processing method is developed to extract results from recordings. Results from micro cantilever experiments suggest that tip deflection is highly influenced by beam length and beam thickness.

Deformation of oil coated water droplets are tested under fluid flow. The micro structure is placed over a partially wetting surface and the deformation of the oil-droplet samples are tested using the mini wind tunnel. Effects of fluid velocity, droplet volume and oil concentration over droplet deformation are studied. Larger droplets deform more as compared to their smaller counterparts. Oil layer covers the water droplet entirely and reduces the influence of fluid force. Higher oil coating induces lesser deformation in droplets

Oil coated droplets are subjected to fluid velocities greater than critical air velocity of the droplets to study the droplet shedding phenomena. Oil coated droplet slip easily as compared to the droplet with no oil coatings for a given fluid velocity. Also, oil coating improve the droplet shedding phenomena. However much higher oil coating slows down droplet shedding and the water droplet floats over pool of oil.

Tip deflection of a microcantilever beam with a point load near the free end under the fluid flow is studied to develop fluid load augmented micro balance. Water droplets of various sizes are used to provide point load. The water droplet is placed over micro cantilever beam at dimensionless length ξ =0.8. An additional fluid load is provided using a mini wind tunnel. Tip deflection of the beam is tested for different fluid

velocities. Results suggest that fluid load augments the tip deflection of micro cantilever beam. This thesis also develops fluid load augmented micro balance.

Acknowledgment

I would like to express deep sense of gratitude and appreciation to my supervisors, Dr. Rama. B. Bhat and Dr. Muthukumaran Packirisamy for their continued support, encouragement and guidance during the course of this work.

Thanks are due to doctorate students of Optical Bio-microsystem lab Durai Chelvan Raju, Kiran Kuruvinashetti and Srinivas Bathini for their valuable suggestions during this work.

I would also like to thank my friend Hamid E. Orimi for his help.

Special thanks to my parents for their moral support.

Contents

List of Figures

List of Tables

List of Symbols

Symbol	
a	Position of droplet from fixed end
A	Area
b	Cytoskeleton base
B	Number of blades in the fan
C	Coefficient
cf	Conversion factor
D	Diameter
E	Young's modulus
f	Friction coefficient
F	Force
g	Acceleration due to gravity
h	Height
H	Shaft minimum input power
I	Unit matrix
Ixx	Moment of inertia about the neutral axis x
Iyy	Moment of inertia about the neutral axis y
K	Loss coefficient
k	Stiffness
l	Length
L	Lift
m	Mass
o	Origin
p	Pressure
P	Point load
po	Position
Pw	Wetted perimeter
px	Pixel
Q	Flowrate
r	radius
Re	Reynolds number
t	Time
T	Kinetic energy
th	Thickness
u	Velocity field
U	Potential energy
v	Velocity
V	Volume
Ve	Voltage
w	Width

X	Concentration
x	x coordinates
y	y coordinates
z	z coordinates

Subscripts

1	Initial value
2	Final value
a	Air
A	Advancing
Ad	Adhesive
avg	Average
b	Beam
c	Contact line
cr	Critical
cs	Cross section
D	Drag
d	Droplet
E	Equilibrium
ED	Exit diffuser
eq	Equivalent
ex	Exit
f	Fan
fluid	Fluid
h	Hydraulic
HC	Honeycomb
i	Any section named ‘i’
in	Initial
int	Interface
LV	Liquid-vapor
max	Maximum
n	Natural
oil	Oil
overall	Overall
p	Pressure
ps	Projected surface
R	Receding
ref	Reference
s	Static
s, avg	Average shedding
SC	Settling chamber
sf	Surface
shear	Shear

SL	Solid-liquid
solid	Solid
sp	Spring
ST	Surface tension
SV	Solid-vapor
tip	Tip
TS	Test section
W	Wetted
w	Water
wall	Wall
WD	Wide angle diffuser
x	x pixel value
y	y pixel value

Superscripts

"	Second derivative with respect to x
*	special
`	First derivative with respect to x
T	Tensor

Greek symbols

γ	Interfacial tension
δ	Deflection
η	Efficiency of the motor
θ	Contact angle
ι	Curvilinear coordinate along the contact line
μ	Absolute viscosity
ν	Kinematic viscosity of air
ξ	Dimensionless length
ρ	Density
σ	Stress tensor
υ	Velocity magnitude
φ	Dimensionless deformation
ϕ	Azimuthal angle
ψ	Angle normal to contact line
ω	Frequency

Abbreviations

BPF	Blade pass frequency
LPM	Liter per minute
RPM	Revolution per minute

Chapter 1| Introduction and thesis objective

Mechanical properties of biological cells have acquired prominence as they find numerous application such as in identifying the cell samples, detection of disease and developing bio devices etc. It is important to understand the response of the cell to applied forces in order to understand cellular behavior. Cells, in general, are of many types. Yet, the primary structure is the same. It was found that mechanical properties of the cell vary with the health of the cell. Basic mechanical properties of cell (shear modulus, spring constant etc.) can be found by studying cellular behavior such as bending/deformation/deflection and dislodgement. While studying cellular behavior it is logical to test these under drag force as cell mostly interacts with bodily fluids such as blood.

Cells undergo deformation, bending etc. to perform biological functions. These mechanical motion transduce biomechanical signals which eventually result in biological response [1] [2] [3] [4] For example, Red blood cells (RBCs), which are in biconcave disk shape undergo deformation while flowing through blood vessels. Leucocytes, white blood cells, are in spherical shapes and roll along vascular endothelium before adhering to tissue. Myocytes, muscle cells have long tubular shape, and undergo deformation when an external load is applied on them. Osteocytes, bone cells continuously undergo deformation while the bones are in motion [5] [6]. Hence, understanding the adhesion, deformability and dislodgement of cell is helpful in developing bio devices. To experimentally study the behavior of the cell it is important to perform studies on suitable sample that would mimic cellular behavior. To simulate cell behavior, it is necessary to understand the structure of the cell. Structural components of a cell are membrane, cytoskeleton, nucleus, cell contractility and motor proteins and adhesion complexes.

1.1 Structural components of a cell

1.1.1 Membrane

The membranes cover the cell. They are generally phospholipid bilayer and the associated protein. As the name suggests they are made up of two layers. They have hydrophobic tail inwards (inside cell membrane)

and hydrophilic tail outwards (outside the cell membrane). Furthermore, these lipid bilayer are homogeneous up to molecular levels, and hence continuum theory is valid [7] [8]. Thus, we can assume the elasticity to be uniform.

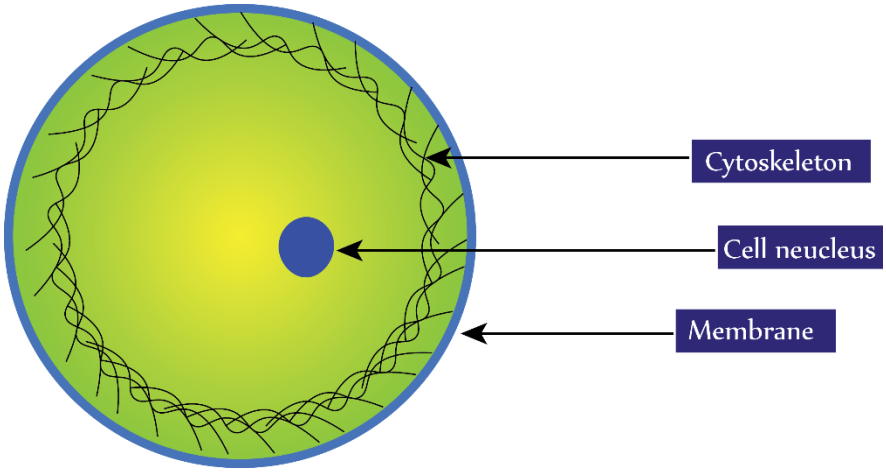

Figure 1.1: Structural component of a cell

1.1.2 Cytoskeleton

These are network of bio polymers that surround the cell as shown in Figure 1.1, and give structural stability to the cell. They are attached to cell and can sustain large strains. The long filament kind of structure helps in withstanding stress.

1.1.3 Cell nucleus

Cell nucleus is present inside cytoskeleton. Depending on the type of the cell, number of nucleus can vary. Red blood cells do not have any nucleus during maturation, whereas skeletal and cardiac muscle cells have more than one nucleus. In eukaryote cell, common cell in human body, one nucleus is present.

1.1.4 Cell contractility and motor proteins

These proteins are filament shaped and help the cell to undergo deformation necessary to reduce tensions in cell. These proteins help cell to maintain cell shape, cell tension and cell migration.

1.1.5 Adhesion complexes

These are basically collection of proteins that form physical linkage between cytoskeleton and extra cellular matrix. They play a significant role in serving tissues from holding together. Also, they help in mechanical coupling of cells and intercellular transport.

Elasticity of the cell has been studied widely among all the mechanical properties of the cell [9]. Cell elasticity is a good indicator of its health. Cell elasticity not only vary when they die, but also, they progressively change as the cell develops disease. Suresh. S [10] studied the elasticity of Red blood cells of human, infected by p.falcipaurm malaria virus. It was found from this study that the shear modulus of RBC progressively increases with disease. There exists three intermediate stages before the p.falcipaurm malaria virus completely sets in. The shear modulus of healthy RBC is 10μN/m. while the same of RBC exposed to p.falcipaurm malaria virus, stage 1, stage 2 and stage 3 infected RBC are 12μN/m, 20μN/m, 40μN/m and 60μN/m, respectively. It can be concluded from this study that healthy RBC is 6 times more elastic than the one infected by p.falcipaurm malaria virus. The shear modulus of cancerous cell varies as well. Following table sheds light on comprehensive data of ratio of shear modulus of healthy and cancerous cells.

Table 1.1: Ratio of shear modulus of healthy cell to cancerous cell obtained from AFM *[11]*

Cell tissue type	Shear modulus ratio of normal cell to cancerous cell
Bladder	
HCV29/Hu456	12
HCV29/T24	32
HCV29/HTB9	5
SV-HUC-1/MGH-U1	12
Prostate	
BPH/LNCaP	9
BPH/PC-3	2
PZHPV-7/LNCaP	6.8
PZHPV-7/Du145	2.3
PZHPV-7/PC-3	1.6
Vero/Du145	2.2

Breast	
MCF-10A/MCF-7	1.4
184A/T47D	1.9
184A/MCF7	1.8
HBL-100/MDA-MB-231	1.7
HBL-100/MCF-7	1.1
MCF-10A/MDA-MB-23	2.2
Cervix	
Normal/cancer primary cell	0.7
CRL2614/CaSki	3.8
HeLa/End1(E6E7)	0.5
Thyroid	
Primary thyroid cells S748/carcinoma cell S277	5
Ovary	
IOSE/HEY	2.8
IOSE/HEYA8	5
IOSE/OVCAR-3	4.3
IOSE/OVCAR-4	2.2
Chondrocytes	
Chondrosarcoma cells FS090 (grade II)/ JJ102 (myxoid chondrosarcoma)	3.6
FS090 (grade II)/JJ102 (myxoid chondrosarcoma)	1.6
FS090 (grade II)/	

It can be observed form Table 1.1 that cell elasticity increases or decreases based on type of cancer. Elastic nature of the cell is due to membrane and cytoplasm. The change in cell elasticity is due to change in structure and component of cytoskeleton [10]. Most of the cellular components are proteins. When a cell is attacked by disease virus a bio-chemical reaction is initiated in the cell. As the reaction progresses the structure and component of the cell changes. Elasticity of the cell indicates this change. Although cell structures are complex, for simulation purposes the structural components of the cell are simplified as membrane, cytoplasm and cell nucleus as shown in Figure 1.2, where cytoplasm is material present inside the membrane excluding cell nucleus. Several numerical studies have been carried on cell elasticity.

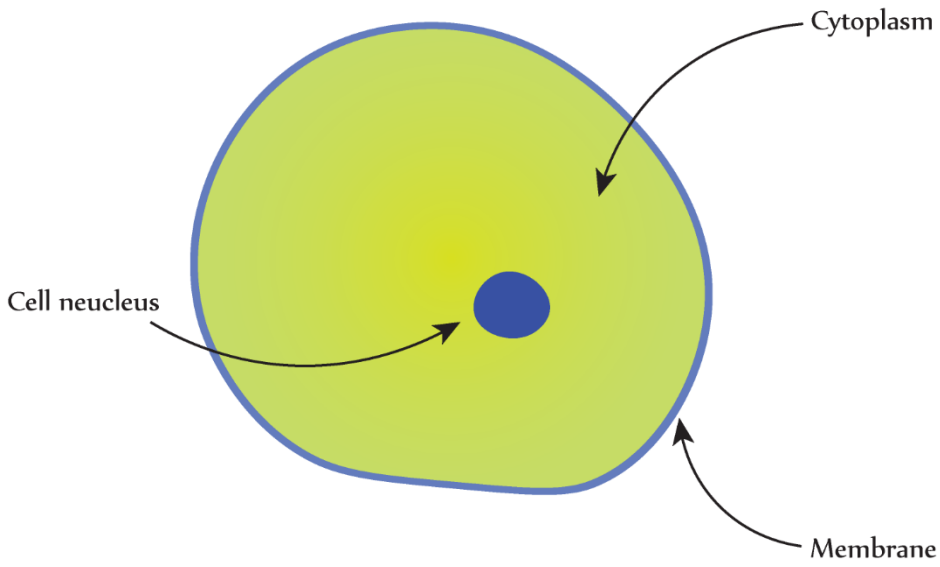

Figure 1.2*:* Simple structure of a cell

Tarrtibi et al [12] formulated a continuum-based cell model, for analyzing elastic behavior of the membrane and cytoskeleton of live cell. Continuum mechanics model correlates force applied to the cell by the glass sphere (analogous to AFM probe) and consequent deformation in the cell geometry and material parameters of membrane and cytoskeleton. Material stiffness depends on mechanical property as well as the geometry of cell. Additionally, cells do not possess one particular shape. Thus, choosing a right geometry was necessary. A 3D shape of axisymmetric semi ellipsoid was considered as the shape of actual cell on a patterned dish resembling this shape. This 3D cell shape is further approximated as 2D axisymmetric semi-ellipse. This approximation was based on the understanding that the cell nucleus floats away from the region of compression form glass sphere and nucleus contribution to load sharing was inferior. This suggests that the cell nucleus absorbs least force applied from glass sphere. Hence cross section of semi ellipsoid without nucleus was considered. The 2D axisymmetric semi-ellipse was described by five geometric parameters. Namely, Sphere radius (R), undeformed cell height (h), cytoskeleton base radius (b), cytoskeleton dome thickness (th), cytoskeleton base thickness (th_b). A 2D axisymmetric model of the cell is shown in Figure 1.3.

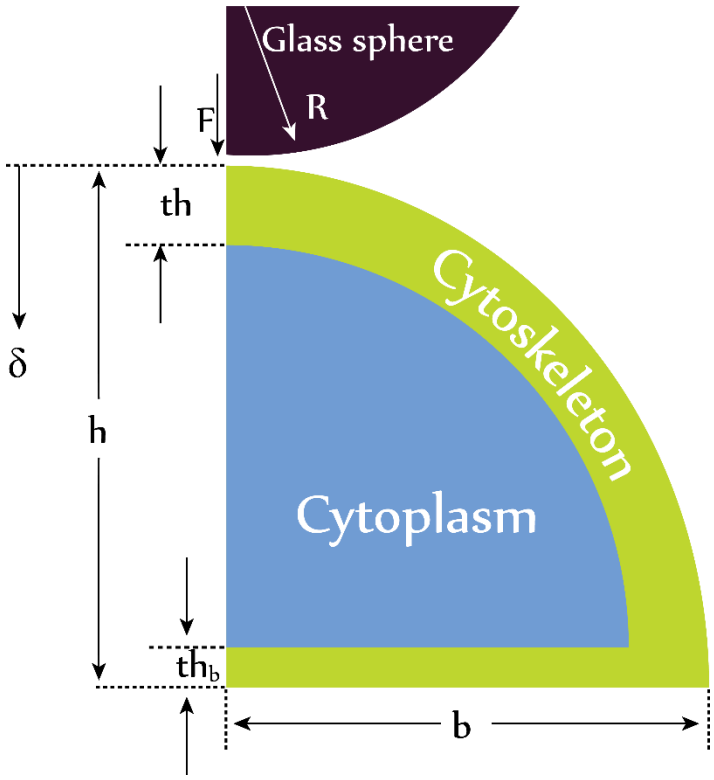

Figure 1.3: 2 D axisymmetric model of a semi-elliptical cell *[12]*.

In this study the cytoskeleton was considered as elastic material while the sub cellular components (cytoplasm) was considered as an incompressible fluid.

T.J Vaughan et al [6] studied fluid structure interaction (FSI) of bone cell to characterize its simulation in parallel plate chamber systems. Ellipsoid profile was considered for the study. Elastic solid was subjected to hydrodynamic load. The properties of chosen incompressible Newtonian fluid providing hydrodynamic load were dynamic viscosity (μ) 0.899mN/s, density = 997kgm^{-3}. Material properties of the structure, elastic modulus (E) and Poisson's ratio (ν), were found by using standard isotropic linear elastic relation $\mu_0 = E/2(1+\nu)$ and $k_0 = E/2(1-2\nu)$. For cytoplasm an elastic modulus of 4.47kPa and Poisson's ratio of 0.4 were chosen. Effect of fluid flow, wall shear stress and pressure over elastic strain of the bone cell were examined. It was found that the elastic strain of cell increases with increase in the volumetric flow. While increasing pressure at the outlet of the chamber increases cell elastic strain, wall shear stress proved to be not effective in causing strain to bone cell.

In other cell adhesion related numerical simulation studies [13] [14] [15] semi spherical or semi ellipsoid cell profile was considered for the study, similar to water drop resting on a horizontal partial wetting surface. Shape of water droplet placed on horizontal surface depends upon several factors.

1.2 Water droplets

Water droplets are fascinating micro structures. Because, in general, shape assumed by liquid depends on its container. When small volume of water dropped in the air, without any container like rain drops, they possess perfect spherical shape. Furthermore, when water is dropped on flat horizontal solid surface they assume wide range of shapes as shown in Figure 1.5. In the absence of container surface tension determines the shape of water droplet [16].

1.2.1 Surface Tension

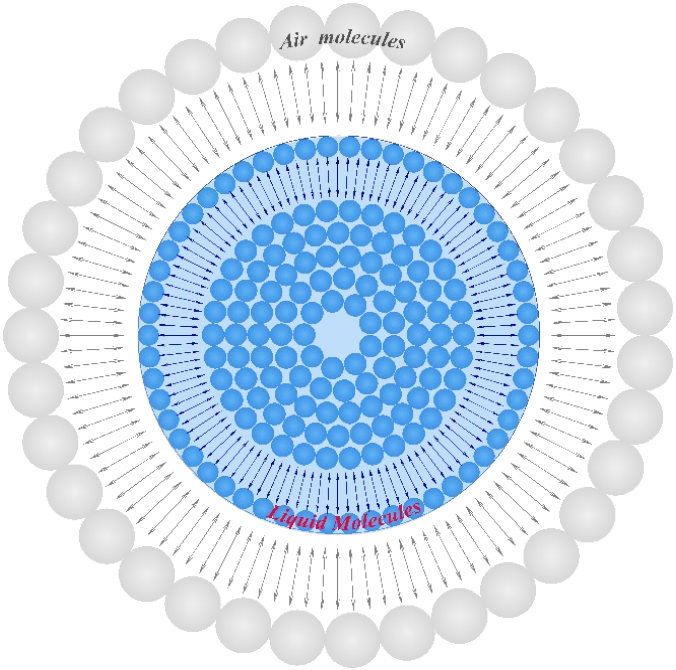

Figure 1.4: Spherical rain drops

Every molecule in a material will experience cohesive force from the neighboring molecules. This cohesive force is the most in solids and the least in gases. Hence solids have its own shape and volume for a given temperature and pressure while, gas neither has its own volume nor its own shape. When water is dropped

in the air, at the liquid-air boundary, water molecules will experience two kinds of forces, namely, adhesive force and cohesive force in addition to gravitational force as shown in Figure 1.4. Adhesive force is from the air molecule surrounding the liquid volume while cohesive force is from neighboring water molecules. Water molecules in liquid air boundary will be pulled on either side by these two forces which causes tension in the water molecule. The cohesive force is stronger and hence droplets are pulled inside. Thus, the rain drops hold spherical shape.

When water droplet is placed on flat horizontal solid surface similar interaction takes place at air-water and solid- water boundary. Water droplet is sandwiched between air and solid surface. Shape of one side of droplet, which is exposed to air, is spherical while the same on the other side depends on surface energy of solid. Surface energy of solid is analogous to surface tension of liquid. At the junction of the three phases, air-water-solid, the shape is decided by the dominant force. Angle made by water droplet with solid surface reveals the dominant force between surface tension and surface energy. This angle is called contact angle.

Young's law given in Equation (1.1) explains the relation between contact angle, surface tension and surface energy [17].

$$\gamma_{SV} - \gamma_{SL} - \gamma_{LV} \cos\theta_s = 0 \tag{1.1}$$

where,

θ_s – Static contact angle

γ_{SG} - Interfacial tension between solid and gas known as solid surface energy

γ_{LG} - Interfacial tension between water and gas known as surface tension

γ_{SL} - Interfacial tension between solid and water

1.3 Surface wettability

Surface wettability is a term coined to explain the nature of solid surface. Surface wettability is established by the contact angle. If the contact angle is less than 90˚ it is called wetting surface and such surfaces are called hydrophilic which means water loving. On the other hand, if the contact angle is above 90˚ it is non-

wetting surface called hydrophobic which means water fearing. Surfaces where static contact angle is above 150° are called super hydrophobic surfaces. Different wetting regimes are shown in Figure 1.5

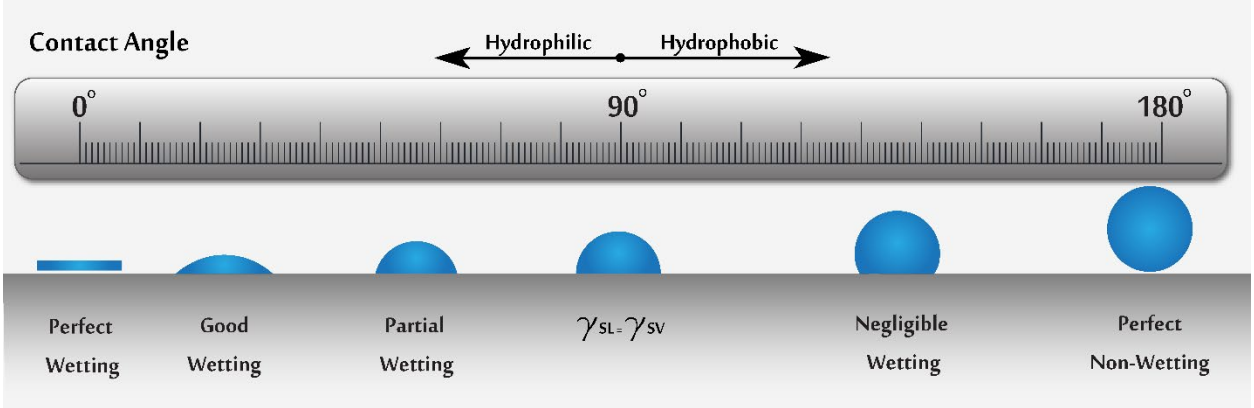

Figure 1.5: Wetting regimes

Water droplets make different contact angles on different solid surfaces because the surface energy of the solids are not the same. Similarly, droplets of different liquids will have different contact angles on the same solid surface because the surface tension of the liquids are not the same. Surface tension is intrinsic property of the liquid. Its value depends on type of intermolecular bonding. Cohesive force between molecules is due to intermolecular bonding. Water has hydrogen bonding while oil such as silicone oil has Van der Waals bonding. Van der Waal bonding are weaker than hydrogen bonding. Thus, any liquid which has Van der Waals intermolecular bonding will have surface tension less than that of water**.**

1.4 Silicone oil

Silicone oil is one of the commonly used lubricants [18] and is a general term used to describe a group of compounds constituting silicon-oxygen bonds and named organ siloxane. Ability of this silicone polymer to repel water, gives the term ‘oil’. Silicone oils are a linear chain polymer of siloxane repeating units (–Si–O). Some type of silicone oil has functional groups (e.g., methyl, phenyl, vinyl, and trifluoropropyl groups) as side chain. The major differences among silicone oils are due to the molecular weight (MW), the length of the linear chain, and the chemical structure of radical side groups, radical end termination of the polymer chains, and the size distribution of the chain. Therefore, each type of silicone oil has specific

chemical and physical characteristics. The viscosity of diverse types of silicone oils, which is expressed in centistokes, is from the molecular weight and from the length of the polymers. Increasing a silicone oil's molecular weight results in an increased polymer chain length and consequently an increase in its viscosity.

1.5 Water droplet as micro structure

Water droplets placed on flat horizontal surfaces will be immobile. Because, water molecules are attracted by surface molecules, which act as fixed constraints, the droplet is held stationary. Such droplets are called sessile droplets. When sessile droplet is under steady fluid flow, tangential component of surface force, called adhesive force (F_{Ad}), acts in the direction opposite to drag force (F_D) due to fluid flow. Droplet will stay pinned to the solid surface until drag force is larger than adhesive force. However, sessile droplet will deform in the direction of fluid flow until $F_D \leq F_{Ad}$. Droplet will assume its initial shape once the fluid flow ceases. This elastic nature is due to surface tension. Hence, water droplet can be considered as flexible deformable microstructure on a surface that offers partial wetting to negligible wetting. Study of interaction of water droplet under fluid flow can be used in the removal of water droplet from Proton Exchange Membrane fuel cell [19] [20] [21] , Oil recovery, Cell adhesion and many more applications.

E.C Kumbur et al [19] studied the factors effecting surface droplet deformation on diffusion media. Experiment was performed to determine the factors by placing droplet on PTFE (Teflon^{TM}) surface. An analytical force balance model was derived to find the droplet instability under shear flow. It was found that channel flow rate, droplet chord length, droplet height, surface properties have influence on droplet deformation. As it can be observed from this study, a static macroscopic force balance in the x direction gives

$$F_p + F_{shear} + F_D = 0 \tag{1.2}$$

where

F_p = pressure force along x direction created by pressure difference due to fluid flow

F_{shear} = shear force exerted by fluid on the top wall due to no slip condition

F_D = total drag force exerted on the droplet along the x direction

The drag force is due to fluid flow and it is function of fluid velocity and pressure gradient. Condition for stability is given by Equation (1.3)

$$|F_{ST_x}| \geq |F_D| \tag{1.3}$$

F_{STx} is lateral component of surface tension force (F_{ST}) also known as adhesive force. To determine surface tension force it is necessary to consider advance and receding contact angle. These are dynamic contact angle**s.**

Contact angle

Contact angle is used to describe the wetting nature of the solid surface. There are several variants of contact angle. Although they are measured in similar manner, each of them carries unique significance.

1. Equilibrium contact angle or Static contact angle (θ_s)
2. Advancing angle (θ_A)
3. Maximum advancing angle (θ_{max})
4. Receding angle (θ_R)
5. Minimum receding angle (θ_{min})

Equilibrium contact angle or Static contact angle (θ)

This is the angle made by the liquid surface, emerging from droplet base, and the solid surface. On a chemically homogenous surface, all the sides emerging around the droplet base would make same angle. This is the angle measured at static condition and hence it is called static contact angle, with the symbol theta (θ_s) As shown in Figure 1.6. The subsequent four angles are measured under dynamic conditions.

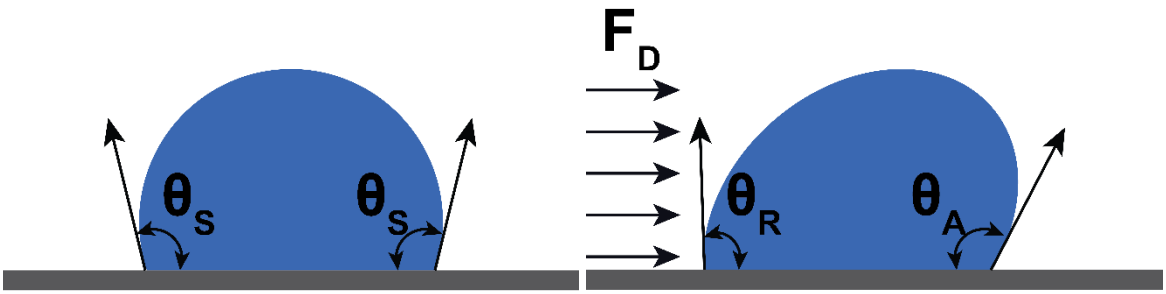

(a) (b)

Figure 1.6 : Droplet under (a) static and (b) dynamic conditions

Advancing angle (θ_A)

Advancing angle is dynamic contact angle measured at the end where the droplet base advances as shown in Figure 1.7. The angle θ_A is always greater than θ. The change in angle from equilibrium condition is because of the external forces that are acting on the drop. Hence a droplet can have different advancing angles based on the magnitude of the force acting. The external forces are gravitational force (F_g) in the case of tilted surface and drag force (F_d) on horizontal surface.

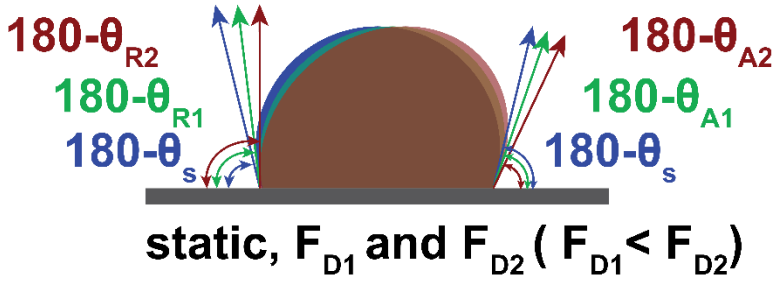

Figure 1.7: Variation of θ_A and θ_R

Maximum advancing angle (θ_{max})

Maximum advancing angle is the maximum possible contact angle of a droplet for a given base area. A droplet of volume 'V_d' makes a contact angle θ. Careful injection of some more liquid to the given droplet would result in an increase in the droplet volume. The droplet side will extend to accommodate additional volume of injected liquid. This results in increase in contact angle. However at $\theta = \theta_{max}$, the droplet cannot stay at equilibrium unless it expands its base. The droplet base advances in order to increase the base area hence this angle is called maximum advancing angle (θ_{max}).

Receding angle (θ_R)

Receding angle is measured at the end where the droplet base recedes. The angle θ_R is always lower than θ. When droplet is under external force one end will advance while the opposite end will recede. Similar to θ_A , a droplet can have different θ_R for the same reason mentioned.

Minimum receding angle (θ_{min})

Suppose volume from the droplet with volume V_d is withdrawn carefully the droplet side will contract around the base. Until $\theta = \theta_{min,}$ Droplet base area will be constant. Further withdrawal of liquid will compel the droplet to reduce its base to find equilibrium. Thus droplet base will contract and the droplet position is receded at either end, and hence this angle is called minimum receding angle (θ_{min}) [22].

$$\theta_{min} \leq \theta \leq \theta_{max} \tag{1.4}$$

Hence Equation (1.4) is called condition for equilibrium. When droplet is under fluid flow contact angle of droplet in the upstream will decrease while in the downstream it will increase. Surface tension force will result in adhesive force which resists the motion of liquid droplet. Surface tension force acts normal to contact area [23]. The lateral component of the surface tension force is considered while estimating the adhesion force. F_{ST} acting on small segment of contact line is given by Equation (1.5) [24]

$$dF_{ST} = \gamma_x d\iota \tag{1.5}$$

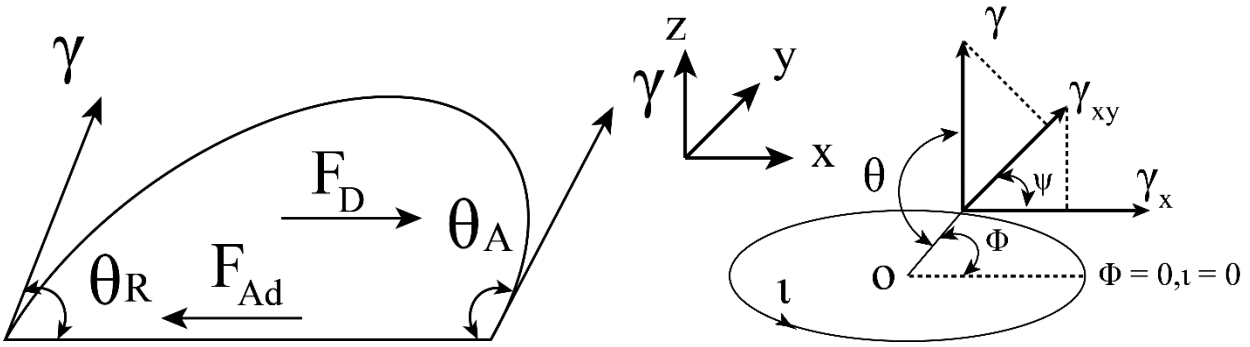

(a) (b)

Figure 1.8: Water droplet under fluid flow *[24]*

For these, γ_x can be found from Figure 1.8 as

$$\gamma_x = \gamma \cos\theta\,(\varphi) \cos\varphi \tag{1.6}$$

For circular contact line $\varphi = \psi$, $d\iota = r\, d\varphi$ (arc length)

Equation (1.6) can be written as

$$dF_{ST} = \gamma \cos\theta\,(\varphi) \cos\varphi\, r d\varphi \tag{1.7}$$

Integrating Equation (1.7) over 2π gives the total resisting force (adhesive force) as

$$F_{ST} = \gamma \int_{0}^{2\pi} r(\varphi) \cos\theta\,(\varphi) \cos\varphi \, d\varphi \tag{1.8}$$

Integrating Equation (1.8) defines a relation between r, φ and θ as

$$F_{ST} = \gamma_{LV} l_c (\cos\theta_R - \cos\theta_A) \tag{1.9}$$

Equation (1.9) is used to find Adhesive force acting on droplet.

Drag force is given by Equation (1.10) as

$$F_D = \frac{1}{2} \rho_a v^2 A_{ps} C_D \tag{1.10}$$

where

ρ_a - Density of air

v - Velocity of air

A_s- Frontal projected area of the droplet to the fluid flow

C_D = Drag coefficient

When the drag force is large enough to violate equilibrium condition droplet will adjust by sliding forward. Hence Equation (1.4) is also condition for dislodgement of water droplet. The phenomena of droplet dislodgement due to fluid flow is called Droplet shedding [25]. The threshold value of drag force before the droplet dislodgment is called point of incipient motion. The velocity of the air at this point is called critical air velocity. Knowing critical air velocity is helpful in droplet dislodgement since it gives idea to match the magnitude of air velocity. The condition for droplet dislodgement is F_D=F_{Ad}, hence to find critical velocity (v_{cr}) one can equate Equations (1.8)- (1.9)

$$v_{cr} = \left(\frac{2\gamma_{LV} l_c (\cos\theta_R - \cos\theta_A)}{\rho_a A_{ps} C_D} \right)^{1/2} \tag{1.11}$$

Deepak et al [26] experimentally found the critical velocity of water drop over different surface wettabilities such as Teflon, Poly(methyl methacrylate) (acrylic glass) and super hydrophobic surface at icing condition (T = -5˚C) and room temperature (T = 24.5˚C). It can be concluded from this study that critical velocity is

a strong function of droplet volume. Even though temperature is function of critical velocity, surface roughness was found to be another significant function of critical velocity. Water droplets on Teflon surface will have critical air velocity of 2-4 m/s. Critical velocity depends on surface roughness. Smoother surface offers less resistance to the droplet sliding and hence critical velocity is lower in smoother surface. Lubrication has been used to reduce friction between mechanical components for many years. Introducing lubricant helps in reducing the critical velocity. Lubricant in general are in solid and liquid states, when the lubricant is provided through liquid medium, such as silicone oil, the droplet shedding problem becomes a multiphase liquid interaction problem. Also, introduction of the oil offers feature such as wetting ridge.

1.6 Oil coated water droplet

Physical properties of the droplet vary when oil is introduced. It is evident that surface tension of the droplet changes since the contact angle for the droplet is different. Studies show that the surface tension of immiscible mixture is not only a function of pure constituent components [27]. However, it is true that when a liquid with high surface tension (water) is mixed with low surface tension liquid (silicone oil) the resulting mixture will have surface tension value in between that of the pure components. Similarly, viscosity of the immiscible mixture cannot be approximated as function of pure components. Surface tension of silicone oil plays vital role in forming shape of water droplets coated with silicone oil. When droplets of liquid with low surface tension are placed on surfaces with relatively higher surface energy, liquid drop will spread on the solid surface as silicone oil on parafilm or Teflon surfaces. When liquid mixture of water and oil is placed on solid ideally oil should spread on the surface while water will form hemispherical shape since water and oil are immiscible liquids. But, this is not completely true. There exists four distinct phases, namely, air, water, silicone oil and solid surface. Surface tension of these individual phases will determine the shape of oil coated water droplets. As explained in the earlier section, in the individual cases of air- water-solid, and air-oil-solid, droplets in each case will have hemispherical and thin layer of oil, due to spreading, respectively. When, these two liquids, water and oil, are brought together the resulting droplet will have a shape shown in Figure 1.9. Water has higher surface tension and hence it will

attract oil molecules which are now held between air and water. Similarly, at multiphase junction oil molecule is pulled from all the sides as shown in Figure 1.9. Hence excess oil will stay at multiphase junction. Since oil droplets on water is held by surface tension of water and air, the thickness of oil layer is uniform. It is possible to have different shapes for water- oil combinations based on surface tension value [28] .

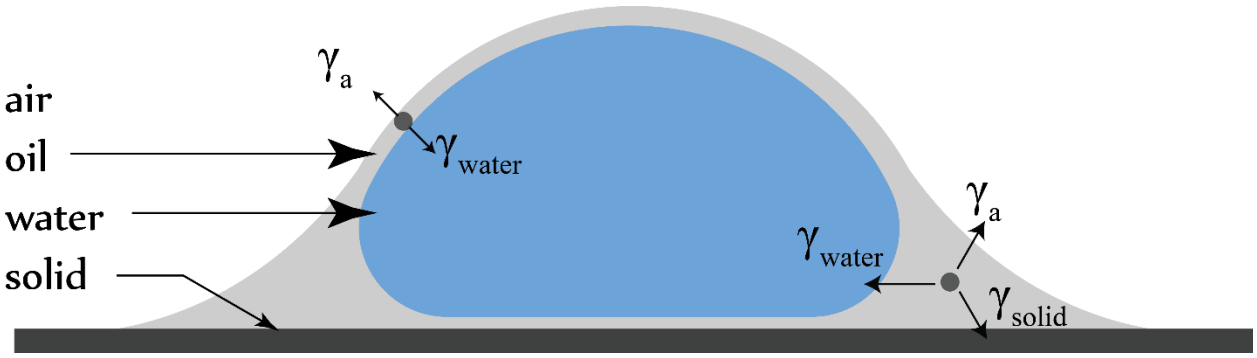

Figure 1.9: Shape of oil coated water droplet

1.7 Fluid structure interaction studies

Fluid structure interaction (FSI) is the mutual behavior between the structure and the surrounding or internal fluid flow when they meet each other. These behaviors include deformation or dislodgement of structure and change in direction of flow or change in intensity of fluid. FSI is very common phenomenon which occurs in nature. Most of the time the fluid flow is wind (air being the fluid) and structures are any natural structures such as hills, mountains, canyons and trees or manmade structures such as buildings, bridges, pavements, wind turbines and airplanes etc., Nevertheless, FSIs are not limited to large structures. For example, several complex structure fluid interactions occur inside human body. Most of the time the fluid is blood and structures are cells, blood vessels etc. Studying FSI of manmade structures in test environment before their actual usage clarifies their resistance to wind load. Similarly, studying fluid interaction with relevant structure enables understanding cellular behavior.

1.8 Wind tunnel

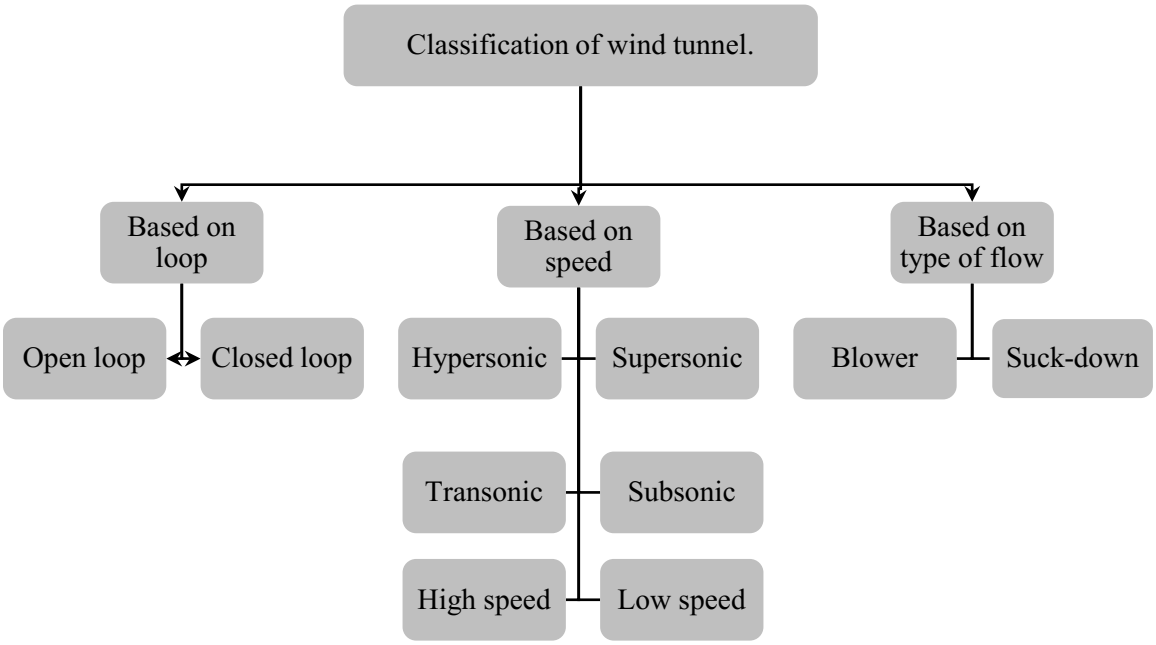

Figure 1.10: Classification of wind tunnel

Wind tunnel is a large tunnel-like structures used to study the effect of aerodynamic force on a test object. Using wind tunnel, one can study the dynamic pressure, static pressure, temperature changes due to air flow and velocity profile of air as it passes a solid object etc. Using wind tunnel, one can mimic the condition of object moving at a speed in stationary air, by blowing air at speed (v_{avg}) past the stationary test object. This would produce the same effect of lift and drag force on a stationary test object, as if it is moving at a speed (v_{avg}) in stationary air. To study the effect of aerodynamic forces on micro objects, a scaled down wind tunnel can be built, to millimeter level, through careful design and fabrication. The scaled down wind tunnel is called mini wind tunnel. One such mini wind tunnel is used in the present study to examine fluid micro structure interaction. A wind tunnel can be classified in a number of ways. Based on speed at which it is operating, it can be divided into low speed, high speed, and subsonic, supersonic, transonic and hypersonic wind tunnel. Based on the type of flow provided by fan it can be categorized as suck down and blower wind tunnel. Based on the type of loop of operation, wind tunnel can be further classified into open loop and closed loop wind tunnel as shown in Figure 1.10. Diverse types of wind tunnel designs are

possible. Design choice of wind tunnel is purely based on the user's requirements. To test microstructures at low speed an open loop wind tunnel is preferred. Open loop wind tunnel is safe from temperature changes in the flow [29] .Since size of the mini wind tunnel is very small compared to size of the room. In addition, an open loop wind tunnel is free from flow disturbance at the inlet, as there is no re-entry of the flow as in the case of closed loop. Figure 1.11 shows the exploded view of a low speed open loop blower wind tunnel. As shown in Figure 1.11 it consists of five basic parts. They are wide angle diffuser, settling chamber, contraction section, test section and exit diffuser. In addition to these five basic parts the settling chamber consists of a flow straightener.

1.8.1 Wide angle diffuser

The wide-angle diffuser is placed at the inlet of mini wind tunnel. It helps in reducing boundary layer thickness [29]. Flow provided from fan takes a longer distance to develop completely on to the tunnel in the absence of the wide-angle diffuser. The rapid increase in flow cross section allows the flow to develop at reasonably shorter distance. It is necessary to have a settling chamber to make the flow steady and streamlined after the rapid expansion in the flow cross section.

1.8.2 Settling chamber

Settling chamber is located at the exit of wide angle diffuser. As it can be observed from Figure 1.11 the settling chamber consists of flow straightener which helps to provide a streamlined flow. Flow straighteners are typically a mesh, covering entire flow cross section. Shape of perforations in the mesh are typically circular. However, square or other shaped perforations are not uncommon. Flow is at its lowest velocity and pressure in this section due to flow straightener and large cross section of settling chamber [29].

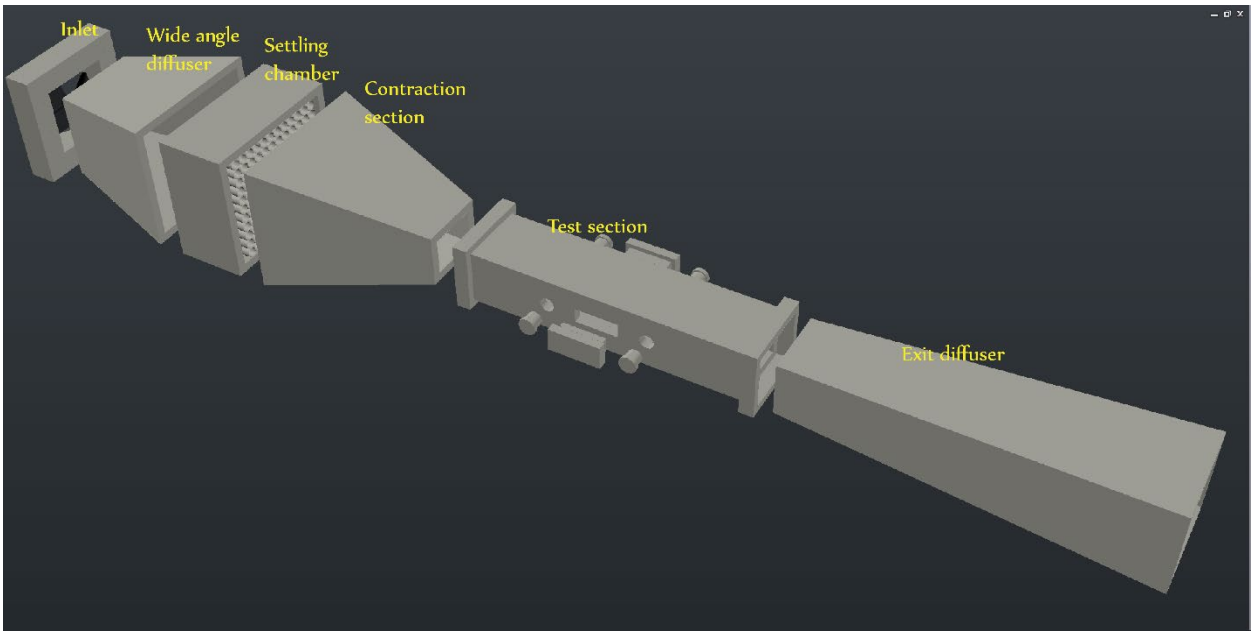

Figure 1.11: Open loop mini wind tunnel

1.8.3 Contraction section

Contraction section follows the settling chamber. Since the flow velocity is reduced in the settling chamber it is necessary to steadily increase the flow intensity. Contraction section helps to increase the flow velocity as the flow cross section decreases gradually [29].

1.8.4 Test section

In this section the FSI is studied. Therefore, test objects are kept in test section. It is a long rectangular flow channel where flow, and pressure are uniform. Test section has the least cross section. As a result, flow velocity is the highest inside the test section. Average flow velocity, ratio of flowrate to area of cross section, of fluid inside test section, v_{avg} is used for calculation such as drag force, since, fluid interacts with test object at this velocity.

1.8.5 Exit diffuser

Exit diffuser is present after test section. It is important to dispose flow to atmosphere at atmospheric pressure to prevent any back mixing. Exit diffuser is longer than test section. Its flow cross section gradually increases. The angle of expansion is typically 4-5˚ [29].

1.9 FSI studies using mini wind tunnel

The small size and mobility of the mini wind tunnel facilitates testing fluid interaction of micro structures such as micro- cantilever beam and water droplets. The test object is kept inside the test section. Fluid is blown past test objects. Response of test object to the fluid flow is recorded using a camera. A microscope attached with camera gives greater resolution.

1.10 Micro-cantilever beam

Micro- cantilevers are tiny dive boards where at least one side, typically thickness, is in the order of micrometers. Their small size makes them easy to mass produce using micromachining process. Micro-cantilever-based sensors have been widely studied due to the several advantages they possess.

a. Low response time
b. High natural frequency
c. High sensitivity

Natural frequency of cantilever beam is given in Equation (1.12) as

$$\omega_n = \frac{1}{2\pi}\sqrt{\frac{\mathrm{k}}{m_b}} \tag{1.12}$$

where

ω_n - Natural frequency of the beam (Hz)

k - Spring constant of the beam

m_b - mass of the beam

Since micro-cantilever beams have relatively low mass the natural frequency is higher and response time is low [30].

Micro-cantilever based sensors can be categorized into three types depending on the sample tested. Namely bio sensors which detect biological samples, chemical sensors which detect chemical components, and physical sensors, which detect physical properties. Working principle for each type of sensor is different. Temperature sensor exploits the thermal expansion of a metal. In this case, Micro-cantilever beam

made up of bimetallic strips is used. Two metals of different coefficients of thermal expansion will expand at different rates causing stress in the beam which in turn causes beam bending [31] [32]. Chao-an et al [31] fabricated bimetallic cantilever by depositing thin layer of TaO_xN_y over silicon and silicon oxide substrate. Strain caused by thermal mismatch between two layers were found.

A successful temperature sensor leads to a new way to develop a bio senor. Biological samples such as fat, protein etc undergo biochemical reactions. These reactions will release heat (exothermic reaction) or absorb heat (endothermic reaction). When such reaction occurs on bimetallic cantilever beam it results in thermal mismatch. Hence a bio chemical reaction can be converted into mechanical motion in the form of bending or change in frequency yielding a way to develop bio sensors. Chemical sensors have been developed for detection of leakage of chemicals. An example is a Humidity sensor. Chemical sensors will be using the selective absorption of chemical compound over the micro- cantilever beam. As a result of absorption, the micro-cantilever beam gets 'loaded' and it causes bending. By the degree of bending one can do quantitative estimation of the sample of interest. In addition, there are numerous micro-cantilever based sensors, which use properties such as capacitance, piezo resistivity etc. Yu-Hsiang Wang et al [30] developed a flow sensor that works on the principle of piezo resistivity. It has a free-standing cantilever beam made up of silicon nitride where platinum-gold acts as piezo resistivity. Wind load applied on the beam will induce stress in beam which results in resistivity in platinum-gold piezo resister. Measuring the resistivity of the layer wind velocity can be found**.** Micro-cantilever is under two kinds of load. One from fluid, and the second from the free-standing structure.

Another important advantage of the micro-cantilever technique is that four response parameters (resonance frequency, phase, amplitude-factor, and deflection) can be simultaneously measured [33]. Micro-cantilever sensors offer enhanced dynamic response, greatly reduced size, high precision, and increased reliability compared to conventional sensors.

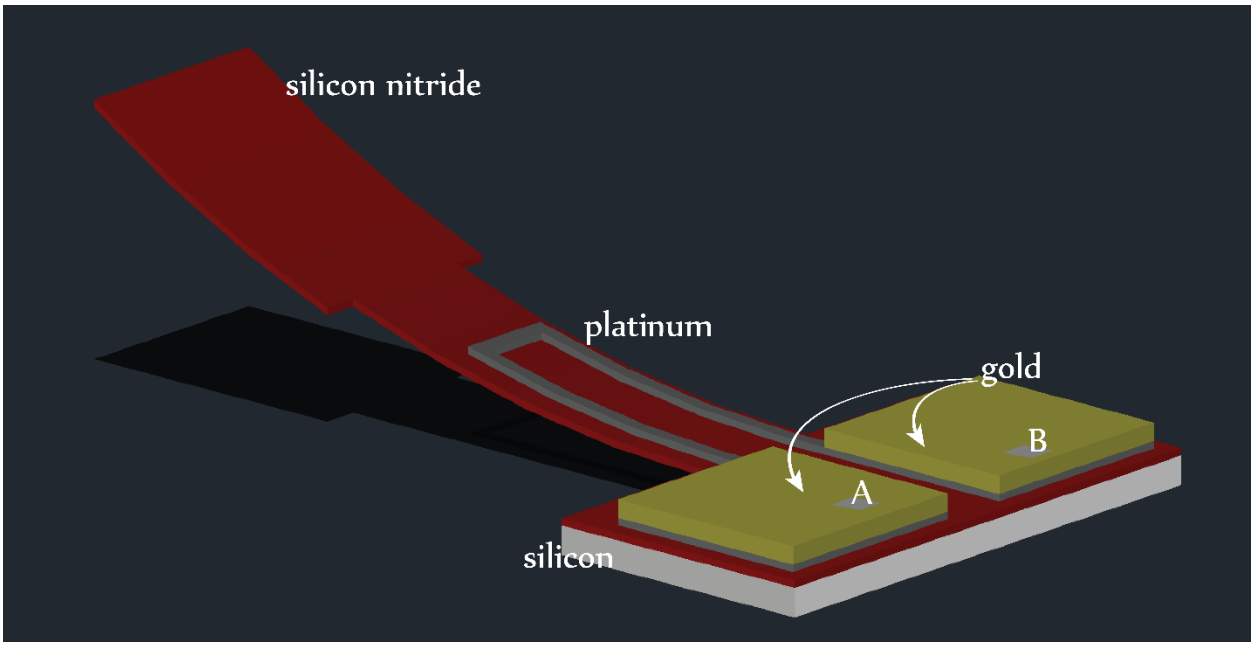

Figure 1.12: Piezo resistive airflow sensor [16]

1.11 Thesis objective, contribution and layout

1.11.1 Thesis objective

The main objective of the thesis is to assimilate cellular behavior by studying the fluid interaction of oil coated water droplets using a simple mini wind tunnel .The sub objectives can be listed as following.

- To validate the design of mini wind tunnel by performing micro- cantilever deflection experiments.
- To study static fluid structure interaction of oil coated water droplet by examining deformation of droplets.
- To study dynamic fluid structure interaction of oil coated water droplet by testing average shedding velocity.
- To study the deflection of the cantilever under fluid flow and droplet loading.

1.11.2 Thesis contributions

Fluid micro structure interaction studies are useful in many ways, be it understanding cell adhesion or developing biosensors. Thus, oil coated water droplets, which shows cellular behavior of wetting, are chosen as micro structures to study their fluid interactions. Mini wind tunnel facilitates testing of deformation and dislodgement of oil coated droplets at low fluid flow. Various factors that influence droplet

deformation and dislodgement are studied and presented here. Furthermore, understanding dynamic response of cantilever under fluid flow and droplet loading in detail is helpful in developing bio sensors.

1.11.3 Thesis layout

The present thesis is structured in manuscript form to study the fluid interaction with microstructures such as cantilever and water droplet inside a mini wind tunnel and application of these studies in bio sensing and sorting area. The thesis comprises of the following six chapters.

Chapter 1: This chapter includes general introduction for the topics discussed in the thesis and literature survey. This chapter also discusses the general physics involved in the study.

Chapter 2: This chapter includes validation of the design of Mini wind tunnel, which is used for testing fluid interaction with microstructures in subsequent chapters, through experimentation. Measurements of tip deflection of Polydimethylsiloxane (PDMS) micro- cantilevers of different aspect ratios under fluid flow inside a mini wind tunnel will be taken. Effect of length, width and thickness over deflection will be studied and design of the mini wind tunnel will be verified. Manuscript submitted to *Experimental mechanics (Springer)*

Chapter 3: This chapter includes the study about water droplet deformation, which acts as test object, on a solid surface using a mini wind tunnel. Silicone oil will be introduced to mimic liquid-liquid bell profile. Effect of Oil concentration, Fluid velocity and Droplet size over deformation will be investigated through experiments. Manuscript submitted to *Colloids and Surfaces A: Physicochemical and Engineering Aspects (Elsevier)*

Chapter 4: This chapter includes experimental determination of average velocity of water droplet shedding over a solid surface due to fluid flow. This chapter discusses the effect of Surface roughness, Oil concentration and Droplet size over the average velocity of droplet shedding. Manuscript submitted to *International Journal of Multiphase Flow (Elsevier)*

Chapter 5: This chapter includes the study of deflection of micro-cantilever with droplet, acting as point load, at various locations along the length of the beam, under fluid flow. Effect of droplet position and fluid flow velocity over deflection is studied. Manuscript submitted to *Microsystems technologies (Springer)*

Chapter 6: This chapter presents the conclusions and possible scope for the future work that can be carried by using current study.

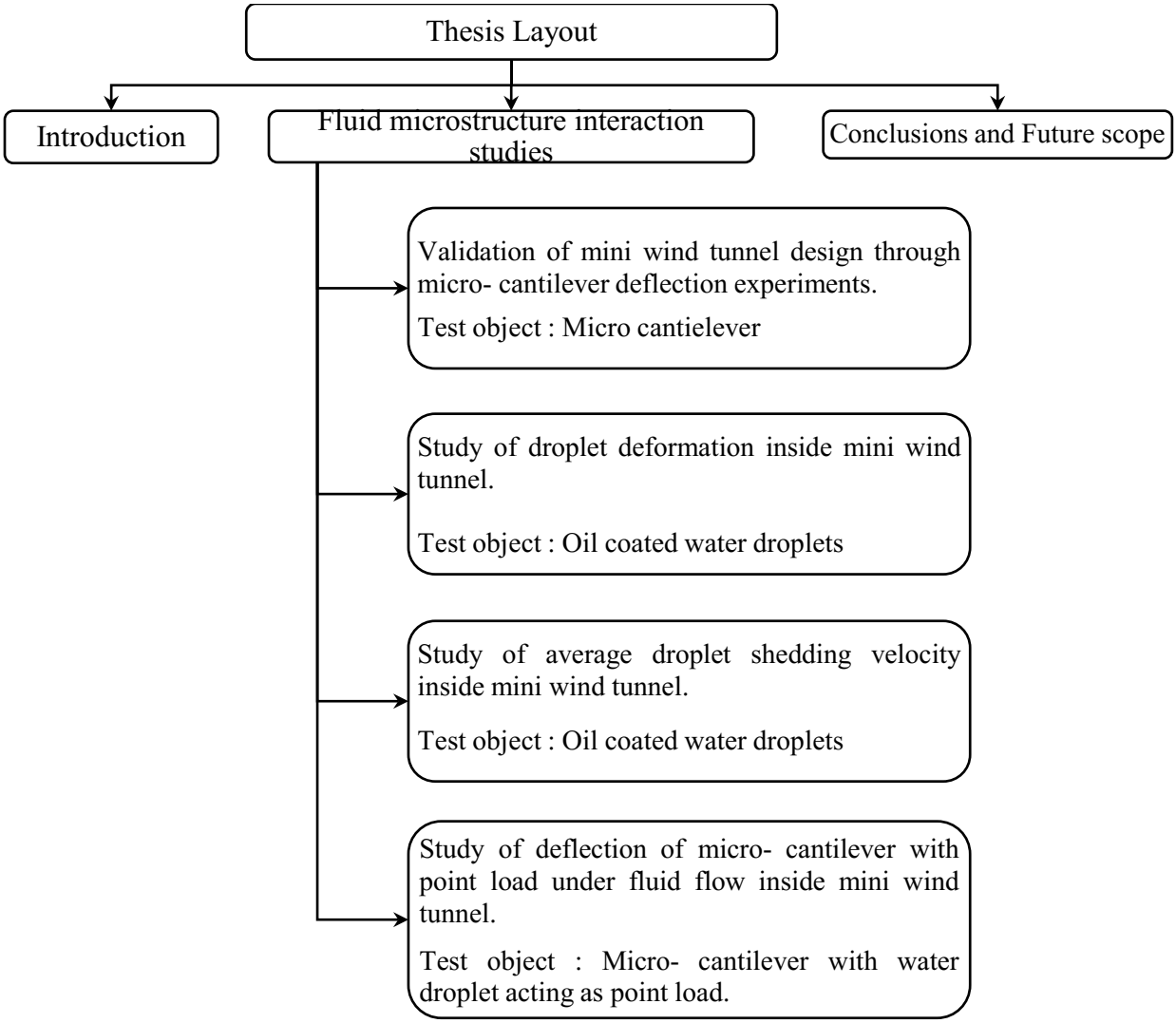

Figure 1.13: Thesis Layout

Chapter 2|Design and study of mini wind tunnel for microsystems fluid interaction under low Reynolds number flows

Abstract

Devices to study fluid interaction of microstructures are rare. In this chapter, details of design and fabrication of a simple open loop modular mini wind tunnel for studying fluid microstructure interaction is discussed. Proposed mini wind tunnel design is finalized after examining various design possibilities. Current design involves five basic sections namely, wide-angle diffuser, settling chamber, contraction section, test section and exit diffuser. The settling chamber consists of flow straightner made from array of drinking straws. Mini wind tunnel is powered by incorporating a fan which provides air flow with Re<1500. Pressure loss across the mini wind tunnel was calculated by finding pressure loss coefficient in each section. Flow behavior inside the mini wind tunnel, particularly test section, was investigated by performing flow simulation using COMSOL finite element modeling. Additionally, smoke experiments confirm streamline flow inside the test section. Fluid interaction of micro-cantilevers was studied using the designed mini wind tunnel. PDMS micro-cantilever beam of different aspect ratios were fabricated and tested for airflow sensing applications. Micro-cantilevers are placed normal to fluid flow and steady tip deflection of the beam was tested. Influence of all three dimensions, length, width and thickness were checked by examining the tip deflection of various micro-cantilever beams. Obtained results suggest that length of the beam is significant contributor to beam stiffness. Furthermore, simulation results are well within agreement with experimental results enabling the mini wind tunnel to be used for any new microstructures.

2.1 Introduction

A small-scale wind tunnel is in the millimeter range to determine fundamental characteristic such as force and drag on a design of choice. However, the forces at the sub Newton level cannot be measured in large wind tunnels. Therefore mini wind tunnel is needed to test devices such as Microcantilevers as shown in Figure 2.1 micro-sensors, micro-electromechanical system etc. to determine the characteristics of the

microstructure. The design of miniature wind tunnel is not readily available, and hence the importance of designing, fabricating and testing andbuilding successful micro-systems. Over the years, wind tunnel has been widely used to study the structure interaction with air. Many interesting studies were performed using wind tunnel. Chien et al [34] studied the effect of high rise buildings to wind direction and velocity.

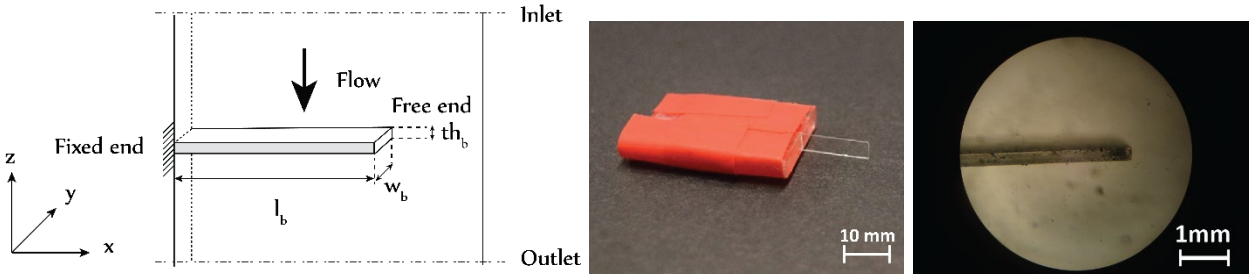

(a) (b) (c)

Figure 2.1. (a) Schematic of microcantilever subjected to flow (b) A micro cantilever beam (4x12x0.24mm) attached to PDMS base and (c) Micro-cantilever tip under microscope.

Due to high rate of urbanization, demand for residence in prime locations of city is high and hence high-rise buildings are common in cities. Series of high rise buildings make a virtual street canyon. Such street canyons push shorter buildings and the pedestrians in the street to a position of vulnerability when there is a strong wind. These artificial channeling will increase the velocity and change the natural direction of the flow. This group studied the effect of street width, podium height and wind direction using a closed loop blower wind tunnel. This wind tunnel consists of two test section separated by a rectangular flow channel. The maximum wind speed of 30 m/s was used for the study. Y. Watanabe et al [35] studied paper fluttering in wind tunnel. Paper fluttering is common phenomenon in printing presses while folding the papers using rollers. A blower type of wind tunnel is used in this study with test cross section area of 1 square meter. The wind velocity used for the study is 25 m/s. Yu Li et al [36] used wind tunnel to study the phenomena of parachute inflation. A steady velocity of 18m/s was used to inflate the parachute. This study was primarily done to design parachute that takes less time to inflate and gives great control for the rider. M. Bastankhah et al [37] performed wind tunnel experiment to finalize the turbine design. Turbulent flow was

used for the study. Closed loop wind tunnel was used with test section dimension of 28 m long 2.5 m wide and a height of 2.25 m. A steady constant velocity of 4.88 m/s was used for the study with Reynolds number in the range of 8000 to 37000. Robert Howell et al [38] used an open loop wind tunnel with test section dimensions of 3 m x1.2 m 1.2 m to study vertical line wind turbine.

2.2 Design considerations

Wind tunnel is a tunnel like structure that allows testing models before making their prototypes Wind tunnel has evolved over decades however, its primitive structure follows the same design rules. There are numerous configurations of wind tunnel based on size, flow velocity flow type and flow cycle. The primary design choice is based on the test object. Other important design considerations are test section, Reynolds number, flow type and flow cycle [39]. The present mini-windtunnel is designed for studying fluid interaction of structure with maximum size of 15 mm^2 under laminar flow.

Reynolds number is defined as the ratio between inertial force and viscous force [40]:

$$\mathrm{Re}=\frac{\mathrm{D_h}*\mathrm{v}}{\nu} \tag{2.1}$$

where:

Re - Reynolds Number

D_h - Hydraulic Diameter (m)

ν - Kinematic Viscosity of Air (m^2/sec)

v - Velocity of the fluid (m/s)

The hydraulic diameter is given by Equation 2.2 [40]:

$$D_h = \frac{4A_{cs}}{P_{wt}} \tag{2.3}$$

where, A_{cs} is the cross-sectional area of the test section and P_{wt} is the wetted perimeter.

In general, Reynolds number is less than 2300 in laminar flow, and hence the Reynolds number inside test section is chosen to be 1500, which is well within laminar flow range.

An open loop cycle was chosen because open loop wind tunnel is safe from temperature changes in the flow [29], since size of the mini wind tunnel is very small as compared to size of the room. This facilitates continuous supply of air at room temperature, which is not possible in closed loop. In addition, an open loop wind tunnel is free from flow disturbance at the inlet, as there is no re-entry of the flow as in the case of closed loop. Two type of flow is possible inside the wind tunnel. One is the suck-down and the other is blow-down wind tunnel as shown in Figure 2.2. The suck-down wind tunnel sucks the air inside the wind tunnel rather than blowing the air. This configuration is rarely used since the entry has to re-ingest the exit flow after it returns through outside as shown in Figure 2.2 (a). Flow straighteners are necessary in this configuration since the flow returning is not consistent. The other configuration is the blow-down wind tunnel as shown in Figure 2.2 (b). The blow-down wind tunnel is the most widely used wind tunnel for its simplicity and cost benefits. The inlet of the wind tunnel contains a wide-angle diffuser [29] . Usual diffusers in wind tunnels have only one diffuser at the exit where the flow leaves at an angle less than 5 degrees, but the blow-down wind tunnel is an exception. The blow-down wind tunnel has inlet diffuser angles exceeding 20 degrees. Wide angle diffuser enables the flow to develop at a shorter distance.

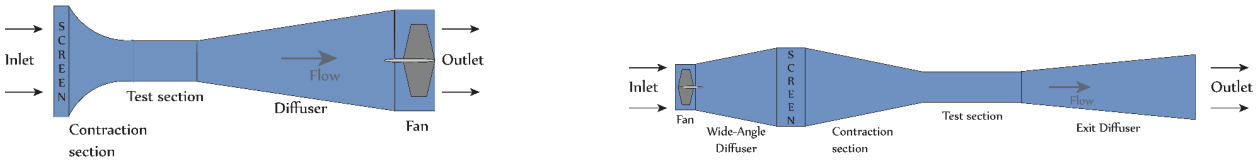

(a) (b)

Figure 2.2: Two potential setups for open loop wind tunnel. (a) Suck-down wind tunnel, (b) Blow-down wind tunnel.

Based on all the design consideration a final decision of open loop laminar flow mini-windtunnel was made. The open loop laminar flow mini-windtunnel is an assembly of five main sections, all of which all have an integral role in the flow. The main parts are the wide-angle diffuser, settling chamber, contraction section, test section, and exit diffuser. The wide-angle diffuser connected to the fan, allows the flow to

expand and decrease in velocity into the settling chamber. The settling chamber allows the fluid to straighten and is the region of the lowest velocity. The contraction section increases the velocity of the flow to get a uniform flow in the test section. The test section is the heart of the wind tunnel with the highest velocity, where the model is tested. Lastly the diffuser slows down the fluid allowing it to exit the wind tunnel slowly to the outside atmosphere without disturbing the flow inside [29].

2.3 Theoretical modelling of wind tunnel design

The mini wind tunnel is an assembly of five main sections which have an important role for the flow of the wind tunnel. The five parts are the wide-angle diffuser, settling chamber, contraction section, test section, and exit diffuser, all in order from inlet to outlet, left to right as shown in Figure 2.2. The design of each part depends on each other through various design parameters that are outlined in this section. A micro-fan was used to power the mini wind tunnel. Modularity of the wind tunnel is achieved by replacing the micro-fan at the inlet. Similarly the test section is replaceable in a modular fashion by loosening and tightening the correct cross section needed for a desired Reynolds number.

2.3.1 Test Section

The test section is the most important part of the wind tunnel since it is where the test model is placed. The flow around the test model must not separate and continue without mixing. For the flow to be laminar and smooth, Reynolds number should be less than 2100 [41]. In this design, a Reynolds number of 1500, which is well below this region, is examined. Test section has rectangular cross section and a common rule is that the width to height ratio of the cross section of the test chamber for small low speed wind tunnels should be approximately$\sqrt{2}$ [29]. Lastly the area of the fan should be 2-3 times larger than the test section [42].

The dimension of the test section depends on the maximum size of the model that needs to be tested. For this design, the maximum size of an object is 15 mm^2. Also the length of the test section depends on the Reynolds Number, and hence for analysis purpose Reynolds number of 1500 is chosen. Based on these

design parameters, the test section has a cross section of 18mm by 12.5mm (ratio of 1.44) and the length is approximately 100mm.

2.3.2 Contraction Section

For wind tunnels that deal with turbulent flow it is important to design the contraction following a 5th degree polynomial for the flow not to separate [43]. However, for low speed wind tunnels with laminar flow, constructing a 5th degree polynomial cross section is not essential, and a circular or rectangular cross section will suffice. The two main constraints placed on the contraction are the area ratio and the length. The area ratio between the inlet and outlet for the contraction is a value between 6 and 9 [29] [44]. The length of the contraction is approximately same as the inlet height of the contraction section [45]. A 45-degree corner fillet to reduce the separation of the fluid [45] is provided. The main purpose of the contraction is to increase the velocity of the fluid and to reduce the velocity fluctuation.

The area ratio chosen for the contraction section is 8.53 (matching the cross sectional area of settling chamber and test-section), as shown in Figure 2.3, which is within the design rule of 6-9. The dimension at the inlet of the contraction is 40x48mm and outlet leads to the test section 18x12.5mm. The length of the contraction is same as the inlet height of the contraction; hence the length of the contraction is 60mm.

2.3.3 Settling Chamber

The settling chamber is a straight short portion of the wind tunnel where the cross section is the largest and is constant. The settling chamber contains screens and honeycomb structure to straighten the flow. The length of the settling chamber is 0.5 times the inlet diameter of the contraction section [42]. The settling chamber cross section is the same as that of the inlet of the contraction, 40x48 mm. Since the inlet of the contraction is not circular, the equivalent diameter is found by using the dimension of the cross section [41]:

$$D_{eq} = \frac{1.265 * {w_{SC}}^{0.6} * {h_{SC}}^{0.6}}{(w_{SC} + h_{SC})^{0.2}} \tag{2.4}$$

where, D_{eq} - Equivalent diameter of the contraction section, w_{sc} - width of the settling chamber and h_{sc} - Height of the settling chamber.

2.3.4 Wide-Angle Diffuser

The wide-angle diffuser is the section that is connected to the fan and is dependent on four main parameters: the area ratio, the diffuser angle, number of screens in the diffuser and drop coefficient of the screens [29]. The wide-angle diffuser has greater angle than usual diffusers with its cross sectional area increasing very rapidly. The wide-angle diffuser is inserted at the beginning of the wind tunnel and has area ratio between 1 and 4 with an inlet area larger than that of the test section by a factor of 2 to 3 [42]. Ideally the selection of the fan is axial, and the area ratio must be taken with respect to an inlet circular cross section. A 25 mm diameter axial fan satisfies all the above requirements. The length of the diffuser is roughly the hydraulic diameter of the settling chamber, which is 45mm.

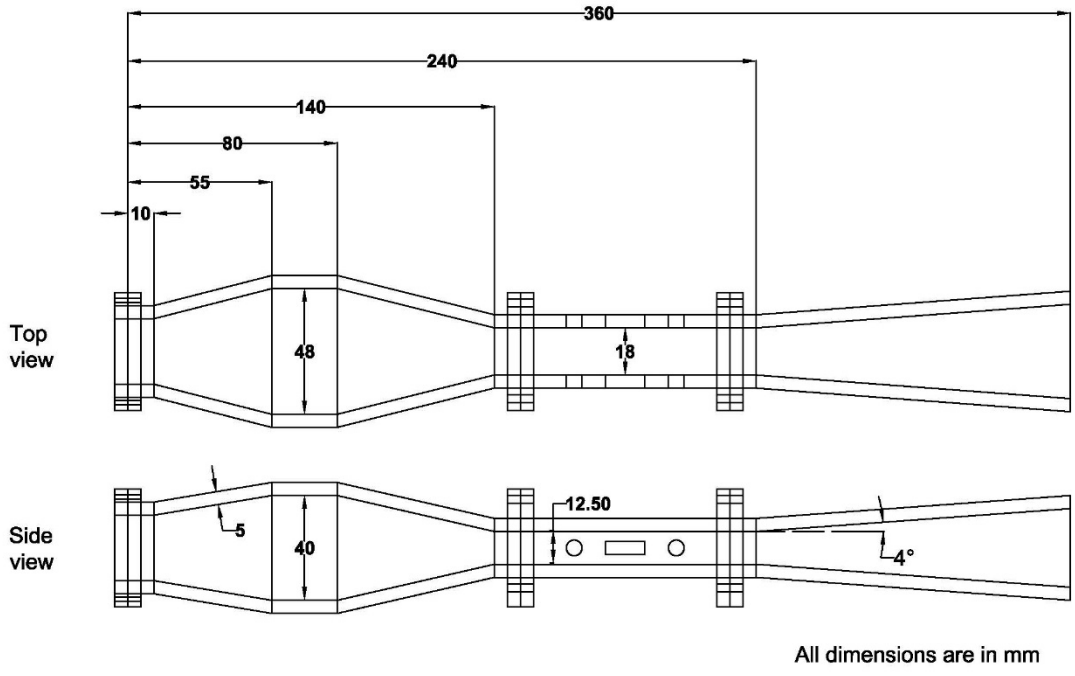

Figure 2.3: Mini wind tunnel dimensions

2.3.5 Exit Diffuser

The exit diffuser is fitted downstream of the test section to allow the flow to leave slowly out. The angle of expansion is between 2-3 degrees, the area ratio is 2-3 times larger than that of the inlet and, the length needs to be between 3-4 times that of the test section. There are designs without exit diffuser, however those models suffer from flow instability in the test section. Exit diffuser is needed to further reduce the fluctuation of the velocity in the test section. The area ratio chosen for the exit diffuser is 1.54 and angle of expansion is 3 degrees. According to these constraints the length is chosen to be 120 mm.

2.3.6 Assembly/Fabrication

The wind tunnel assembly is completed once all the five parts are designed and fabricated. The cross section, angles and lengths are summarized in Figure 2.3 . The test section is of prime importance because here the microstructure of interest will be kept and analyzed. Therefore this section requires additional design features such as openings to place test objects, sensors etc. Hence two 10mm diameter openings are made on the sidewalls for data acquisition and monitoring the test specimens. Similarly, a larger rectangular block is made in between the openings as shown in Figure 2.4, to insert micro structures. The size of the rectangular block is 5 by 15mm, which gives enough room to operate for models in the micro scale. The wind tunnel altogether is 360 mm in length, which is considered a small-scale wind tunnel. The two brackets at the test section allow adjusting different cross sections and provide access to clean inside. The bracket at the inlet of the tunnel is connected to the wide-angle diffuser, which permits interchangeable fans to achieve different Reynolds number.

Wind tunnel fabrication can be done in many different methods. The choice of material is acrylic sheet due to its transparent property and smoothness. The transparency allows flow visualization and the minimum roughness does not hinder the flow path to achieve laminar flow. A laser machine is used to cut 5.6 mm thick acrylic sheet. It is important to choose a thick enough material to have a better handling during assembly. Each section of the wind tunnel is made from four pieces of acrylic sheets that are glued together

using dichloromethane (CH_2Cl_2) to create the specified geometries. The CH_2Cl_2 is an adhesive for plastic material and it bonds within seconds of application of the product.

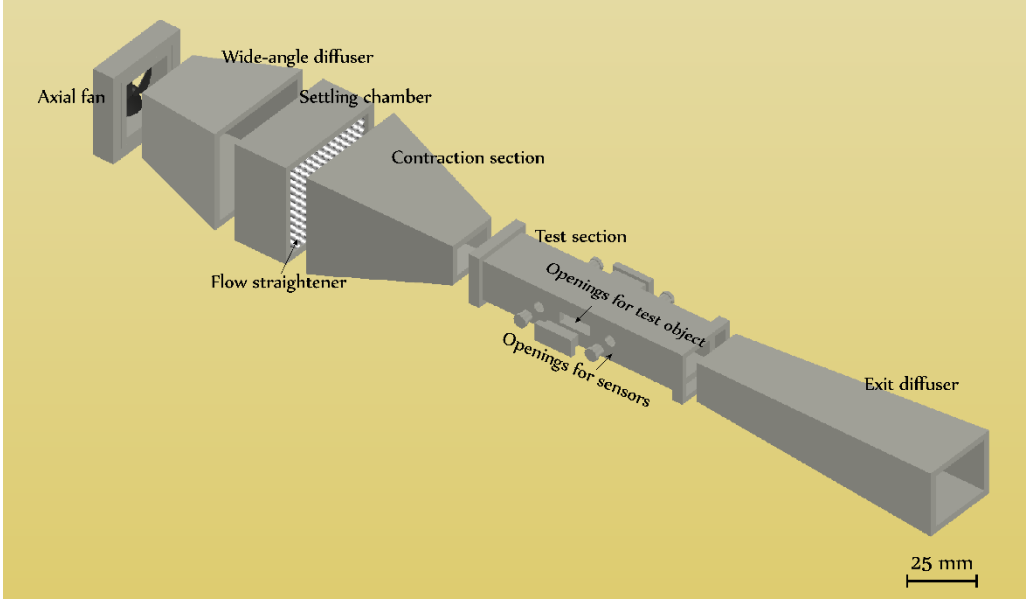

Figure 2.4: CAD 3D model of mini wind tunnel

Once each section is successfully glued together, brackets are glued at both ends of the test sections. The brackets are bonded since modularity is important in the miniature wind tunnel design. The brackets allow removing and implementation of different test sections. A similar bracket is placed at the inlet in order to change fans to get a wide spectrum of airflows. Other connections that are tapered such as the contraction, wide-angle diffuser and exit diffuser are rounded and smoothed in order to assemble properly. Lastly, Figure 2.5 is the built mini-modular wind tunnel

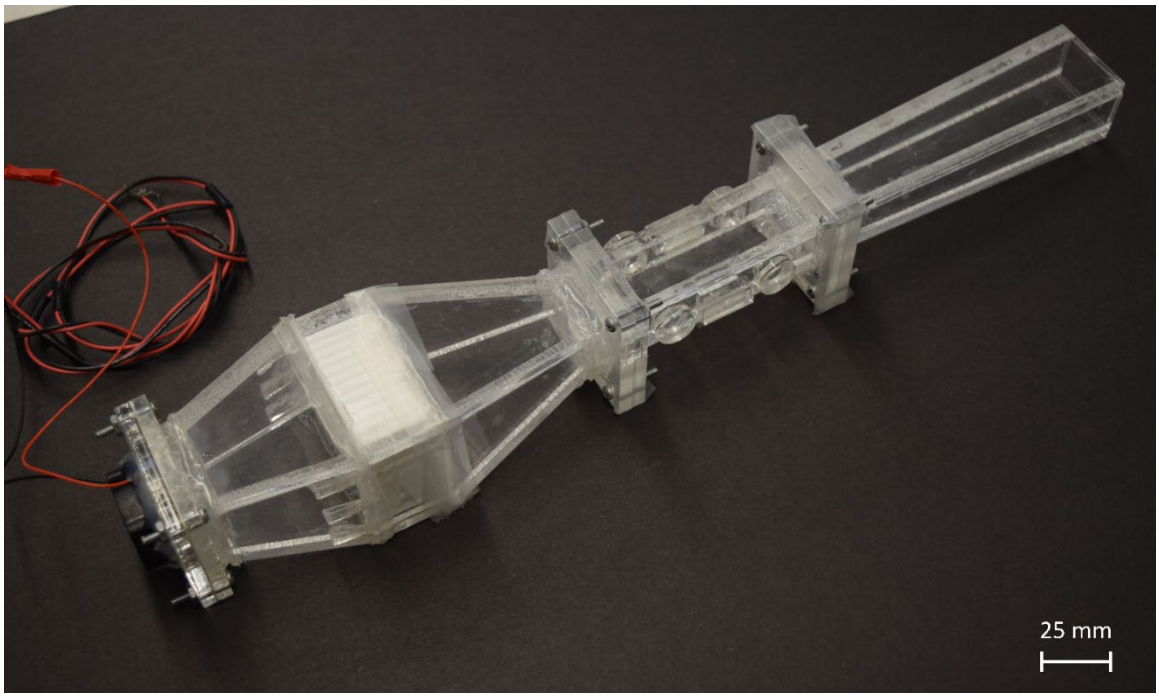

Figure 2.5: Final assembly of mini wind tunnel

2.4 Analysis of losses in wind tunnel

To determine the total pressure loss in the wind tunnel, it is important to understand the losses in each component of the wind tunnel. The loss coefficient K is found using engineering design rules. The equations and graphs that determine the losses of each section originate from large wind tunnel designs, as there are very few artifacts on design rules for mini wind tunnel. Once the K value is determined, the pressure drop from the inlet to outlet is found by using the fundamental fluid dynamic Equation (2.4) [40]:

$$p_i = \frac{K_i * \rho_a * v_{avg,i}^2}{2} \tag{2.5}$$

Friction loss coefficient (f), length of the certain section (l_i) and diameter of the section (D_i) is grouped together as (fl_i/D_i), loss coefficient of section Ki. Subscript 'i' denotes the values of the particular section. p_i is the pressure , $v_{avg,i}$ is average velocity of the air in section named 'i' and ρ_{air} is the density of air at 25˚C.

2.4.1 Test Section Loss Coefficient

The losses in the test sections are along the straight length. The loss coefficient for a long straight section compared to those for the other components of the wind tunnel is given in Equation (2.5) [40]:

$$K_{TS} = \frac{f_{TS} \times L_{TS}}{D_{TS}} \tag{2.6}$$

The parameter *f* is defined as the friction coefficient $f_{TS} = \frac{64}{Re}$ which is only defined for laminar flow, (L_{TS}) the length of the test section is 100 mm and the equivalent hydraulic diameter (D_{TS}) is 14.75 mm. The loss coefficient of the test section is 0.2893. The pressure drop in the test section is estimated as 0.4463 Pa using a velocity of 1.59 m/s for a Reynolds number of 1500.

2.4.2 Contraction Loss Coefficient

To determine the losses in the contraction section the following equation is applied [41]:

$$K_{CS} = \frac{0.32 * f_{avg} * L_{CS}}{D_{ex}} \tag{2.7}$$

The average friction coefficient, f_{avg} is found from the mean of the friction coefficient on both sides of the contraction section.

$$f_{avg} = \left\{(\frac{1}{2})\left(\frac{64}{Re_{inlet}} + \frac{64}{Re_{outlet}}\right)\right\} \tag{2.8}$$

The equivalent exit diameter (D_{ex}) is 14.75 mm which is for the cross section leading into the test chamber of 18x12.5 mm. The loss coefficient for the contraction section is 0.3031 and the corresponding pressure drop across the contraction section is 0.4675 Pa, estimated using Equation (2.4).

2.4.3 Settling Chamber Loss Coefficient

The settling chamber is the shortest straight section of the wind tunnel. For relatively small straight sections, the loss coefficient is [41]:

$$K_{SC} = \frac{0.01 * l_{SC} * (a_{SC} + b_{SC})}{w_{SC} * h_{SC}} \quad (2.9)$$

where, w_{SC} and h_{SC} are width and height of the settling chamber, 48x40 mm, and the length l_{SC} is 25 mm, as shown in Figure 2.3. The loss coefficient according to this equation is 0.01146 and, the pressure drop for the settling chamber is the smallest of all sections due to its small length, which is 2.43x 10^{-4} Pa

The honeycomb structure that is placed to straighten the flow also contributes to the loss in the wind tunnel. The honeycomb structure is composed of 132 straws with 3.5mm diameter. The ratio of free area to the total area of the settling chamber is 0.6610. From these values losses at obstruction to the flow, screen loss coefficient factor, can be found from the Woods handbook [41] as K_{HC}= 0.71. The pressure associated to this loss is 1.52x 10^{-5} Pa.

2.4.4 Diffuser Loss Coefficient

The loss coefficient of a diffuser is dependent upon the cross section of the inlet and the outlet [41] which is represented by an equivalent diameter. The equivalent diameter depends on the shape of the diffuser. There are generally four types of diffusers that determine the equivalent diameter [41].

The wide-angle diffuser chosen for the wind tunnel design has a transition from circular to rectangular cross section. The fan inlet is circular (25 mm diameter) and hence the equivalent diameter is 25mm. There is a gradual expansion loss when the air from the fan enters the wide-angle diffuser. For any given diffuser a standard loss coefficient, K = 1 should be added to the existing loss coefficient which is 0.9450, [41] , thus making the total loss coefficient for the wide-angle diffuser, $K_{WD} = 1.9450$ and the corresponding pressure drop of the wind-angle diffuser was found using Equation 2.4, which is P_{WD} = 0.000477 Pa.

Similarly for the exit diffuser, the equivalent diameter needs to be determined to find the loss coefficient. The exit diffuser located at the end of the wind tunnel has a transition from one rectangular cross section to another. Therefore the equivalent diameter is 14.75 mm. The loss coefficient is determined

as 0.23 [41]. Adding standard loss coefficient the total loss contributed by the exit diffuser is $K_{ED} = 1.23$. The pressure drop, using the velocity as (0.051m/sec) in Equation 2.4, of the diffuser is P_{ED} =1.89 Pa

2.4.5 Total Loss Coefficient in Wind Tunnel

The total loss coefficient of the wind tunnel is determined by summing the coefficient factor K, across the system. The total loss coefficient is:

$$\sum K = K_{TS} + K_{CS} + K_{SC} + K_{WD} + K_{ED} + K_{HC} \quad (2.10)$$

The loss coefficient allows determination of the minimum power to run the wind tunnel. The second most important parameter is the total pressure drop of the wind tunnel. The total pressure drop gives an idea of the losses that are occurring in the wind tunnel and can be further compared with 3D simulation model to indicate the validity of the analytical calculations. The pressure drop in the wind tunnel due to the losses is 2.64 Pa.

$$\Delta P = P_{TS} + P_{CS} + P_{SC} + P_{WD} + P_{ED} + P_{HC} \quad (2.11)$$

2.4.6 Power Supplied to Wind Tunnel

The minimum power needed for the wind tunnel is determined through knowing the losses in the system. One approach is using an equation that estimates the power of the shaft to rotate the fan [42]:

$$H = (\frac{\sum K}{\eta}) * \frac{\rho_a * A_{TS} * v_{TS}^2}{2} \quad (2.12)$$

where:

H- Shaft minimum input power (W)

η- Efficiency of motor

The power needed to run the low speed wind tunnel is about $1.22*10^{-3}$ Watt. The efficiency of the fan motor was approximated as 0.8. The second parameter that is noted for selection of the fan is the airflow. An axial fan is selected with maximum airflow 0.026m^3/min which corresponds to a maximum Reynolds number of 1500.

2.5 Mini wind tunnel simulation set-up

Flow simulation was performed on the wind tunnel to understand the behavior of the flow inside. COMSOL MULTIPHYSICS 4.2 was used to analyze the flow. Fluid was set to be Laminar, incompressible and inviscid inside the wind tunnel. Navier-Stokes and continuity equations were used to analyze the flow parameters, namely, velocity and pressure. Stationary solver was used to solve the equations. Following equations were used by the solver.

In the following, **u** is the velocity field, **F** is the volume force, **p** is the fluid pressure, **μ** is the dynamic viscosity of the fluid, ρ is the density of the fluid and **I** is the identity or unit matrix. The effect of the gravity is neglected as the fluid considered is air.

For laminar flow:

$$\rho_{fluid}(u_{fluid}.\nabla)u_{fluid} = \nabla.\left[-pI + \mu_{fluid}\left(\nabla u_{fluid} + (u_{fluid})^{T}\right)\right] + F \qquad (2.13)$$

$$\rho_{fluid}\nabla.u_{fluid} = 0$$

The selected boundary conditions are

$$No\ slip\ at\ the\ wall, u_{fluid} = u_w = 0 \qquad (2.14)$$

$$At\ the\ inlet, u_{fluid} = -v.n \qquad (2.15)$$

$$At\ the\ Outlet, p = p_o \qquad (2.16)$$

The wind tunnel was sliced along the length to observe the pressure and velocity distribution along the length. The cut section is illustrated by Figure 2.6. The honey-comb structure was also sliced to understand the behavior of velocity inside the honey-comb which is represented in Figure 2.6.

The simulations were carried out for the minimum flow rate of 160 ml/s and the observations were made for the velocity variations. A 2-D representation of velocity and pressure distribution along the length of the Mini wind tunnel is shown in Figure 2.6(a) and (b). The pressure is the highest at the inlet of the wind tunnel, decreasing as the flow passes through honey-comb structure and at the inlet to the test section. A 3-D visualization of transverse velocity distribution is shown in Figure 2.6 (c). The velocity distribution along the transverse direction at the cut-section of the honey-comb structure is shown in Figure 2.6 (d).

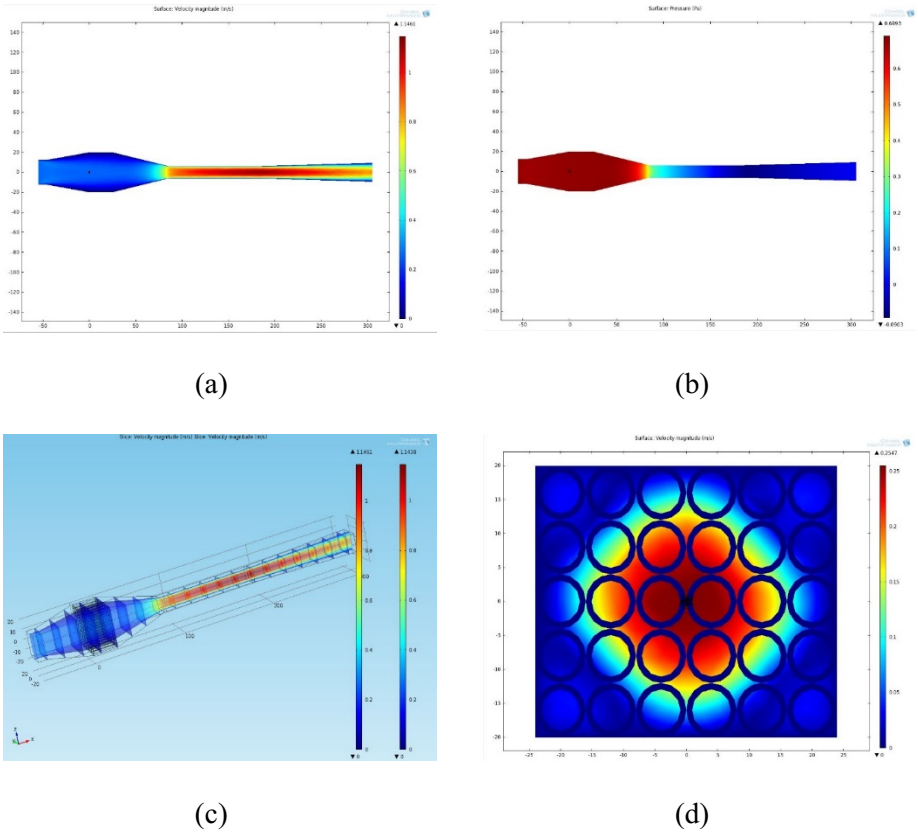

(a) (b)

(c) (d)

Figure 2.6:(a) Velocity, (b) Pressure profile along the wind tunnel for the flowrate 160 ml/s. (c) 3D Representation of velocity profile. (d) Velocity profile through honeycomb structure.

2.6 Experimental Setup

The mini wind tunnel that was designed and built is shown in Figure 2.5. It consists of an axial flow fan at the inlet, with dimension 25x25x10 mm. It gives a maximum air flow of 460 ml/s. The operating range of the fan is about 3-6.8 V. Flow rate given by the fan can be controlled by the input voltage given to the fan. Fan RPM, Reynolds Number (Re) and Flowrate (Q), were measured for different Fan voltage (V_f). Each property has linear relationship with Fan voltage as shown in Figure 2.7 (a), (b) and (c). To confirm that the test section receives a laminar streamlined input, a smoke test was carried out. The smoke test consists of sending dry ice smoke streams into the wind tunnel. The first four images are focusing on the test section, where the flow must have straight streamlines. The smoke streams are straight which characterizes laminar

flow. Figure 2.8(a) corresponds to when airflow in the wind tunnel is absent. Figure 2.8 (b), (c) and (d) show the streamlines for Reynolds numbers of 650, 800 and 1500, respectively.

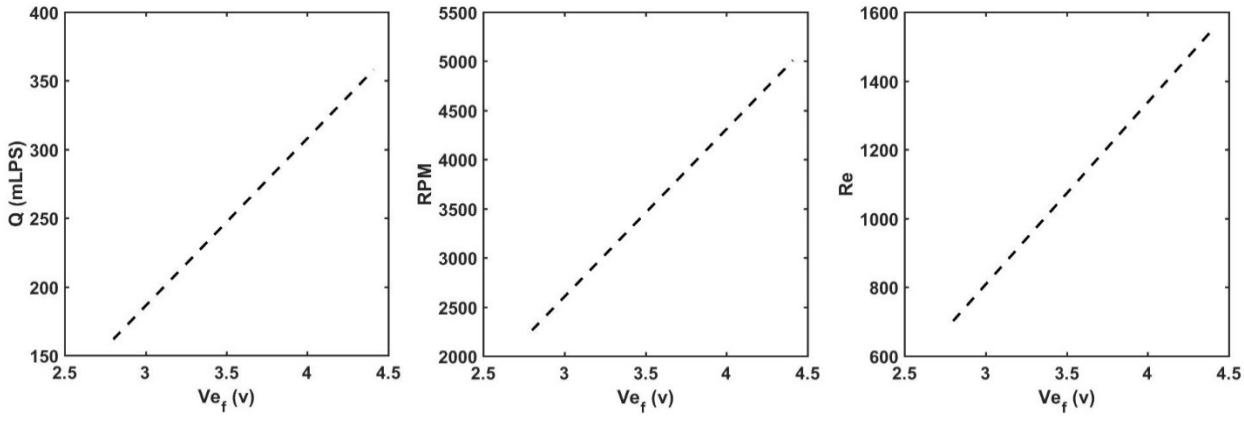

(a) (b) (c)

Figure 2.7: (a) Flowrate (Q), (b) Fan RPM and (c) Reynolds number (Re) as the function of Fan voltage (ve_f)

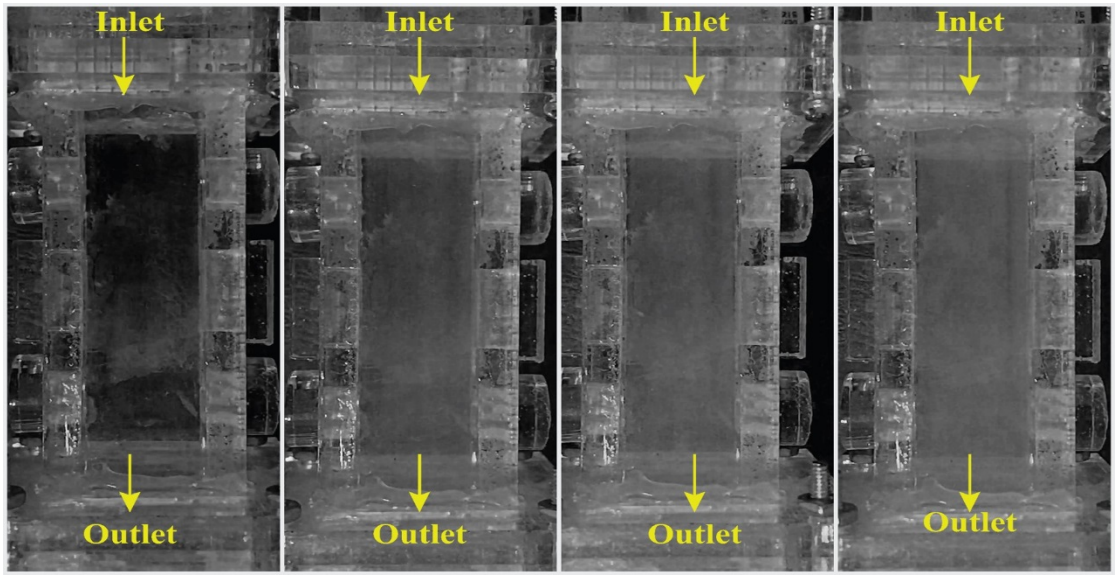

(a) (b) (c) (d)

Figure 2.8: Streamlines in Mini wind tunnel for Reynolds number (a) 0, (b) 650, (c) 800 and (d) 1500.

2.7 Microcantilever study in wind tunnel

2.7.1 Cantilever Simulation Setup

COMSOL 4.2 Multi-physics was used to simulate the test section as the channel and the microcantilever as the solid structure in between, as shown in Figure 2.9. The physical model used was Fluid-Structure-Interaction (FSI) that describes the behavior of the cantilever subjected to fluid flow. The dimension of the test section is given in Figure 2.3. In FSI physical model, an arbitrary Lagrangian-Eulerian (ALE) method was used to capture the deflection of the cantilever. While Lagrangian describes the solid mechanics of the cantilever, Eulerian describes the fluid flow through test section. The cantilever is set to include the inertia term for transient behavior.

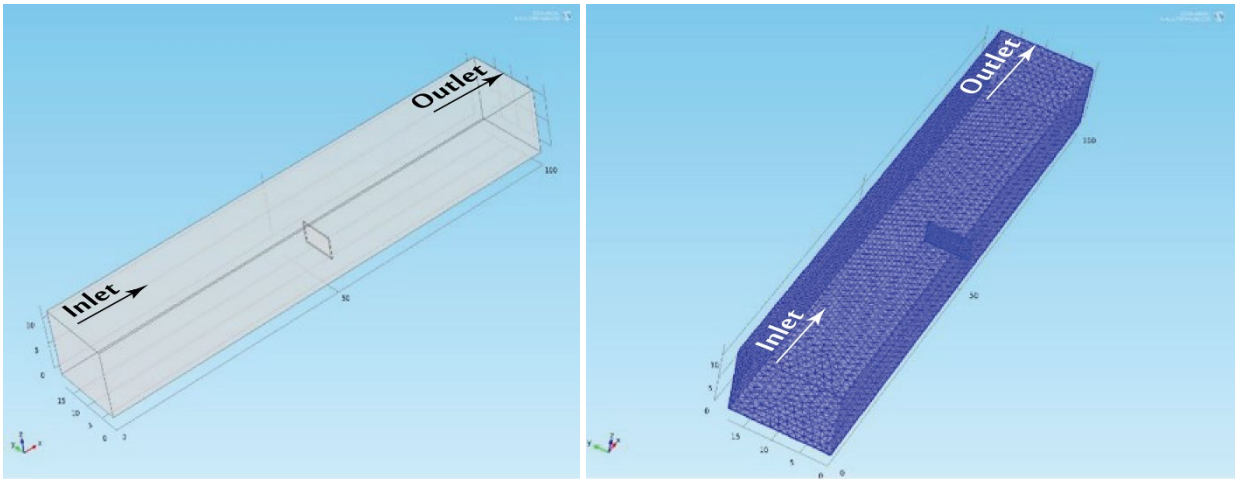

(a) (b)

Figure 2.9: Microcantilever simulation setup (a) Without mesh (b) With mesh.

$$\rho_{fluid}\frac{\partial u_{fluid}}{\partial t} + \rho\left(u_{fluid}\,.\nabla\right)u_{fluid} = \nabla.\left[-pI + \mu_{fluid}\left(\nabla u_{fluid} + \left(\nabla u_{fluid}\right)^{T}\right)\right] + F \tag{2.17}$$

$$\rho_{fluid}\,\nabla.u_{fluid} = 0 \tag{2.18}$$

$$\rho_{fluid}\frac{\partial^2 u_{solid}}{\partial t^2} - \nabla.\sigma = F.u \tag{2.19}$$

Since the pressure losses in the wind tunnel are small compared to the fan pressure, they are not taken into consideration in the simulation. Pressure at the inlet is determined at different flowrates using the Equation (2.19)

$$p_{In} = p_{Ref} * \left(\frac{RPM_{Ref}}{RPM_{In}}\right)^2 \tag{2.20}$$

At the outlet, a laminar flow is set with an exit pressure of zero, and exit length of 0.12 m, which represents the length of the exit diffuser. The boundary condition that is applied to the cantilever is fixed constraint on the side wall of the channel. The Linear Elastic model is chosen to simulate the behavior of the PDMS cantilever with Young's modulus of 802 kPa, Poisson ratio of 0.45 and density of 965 kg/m^3 [46].

2.8 Micro cantilever Experimental Setup

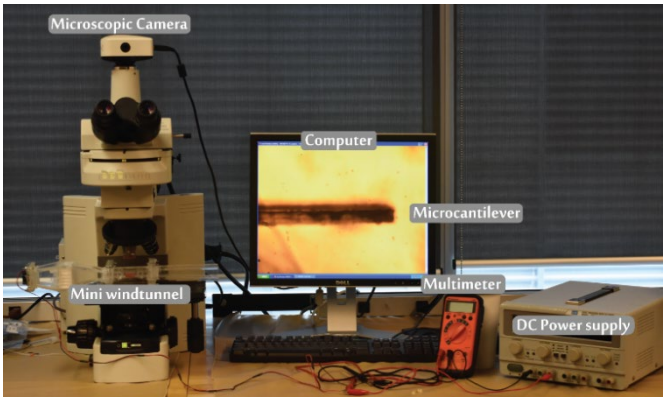

(a)

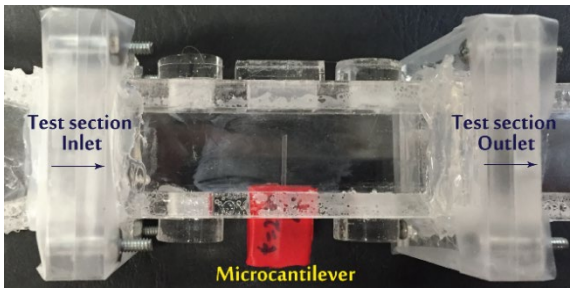

(b)

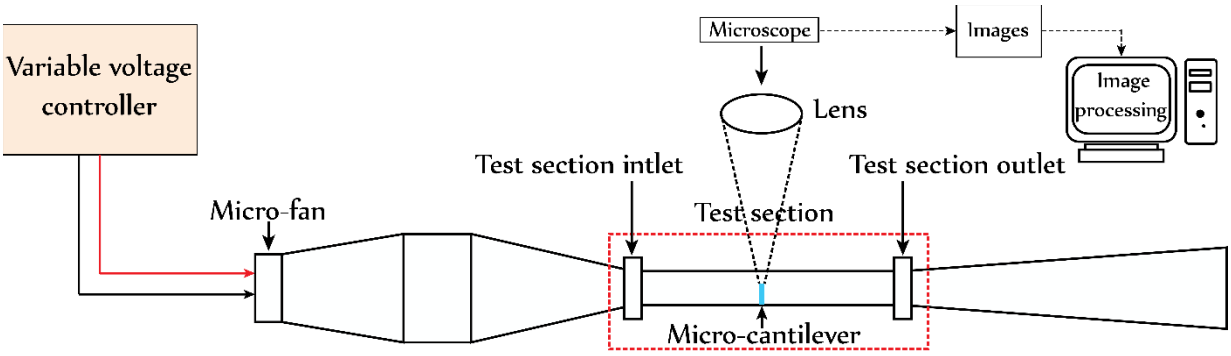

(c)

Figure 2.10: (a) Experimental setup (b) Micro cantilever inside test section, (c) Schematic of the experimental setup

Micro cantilevers were fabricated to perform deflection experiments in the wind tunnel. The micro cantilevers were made of Polydimethylsiloxane (PDMS). Ratio of 10:1 of base to curing agent is used to achieve the desired material property [46]. Once the base was mixed with the curing agent, it was placed in a vacuum seal container to get rid of any bubbles during mixing. Then the mixture was spin coated. The RPM of spin coating machine was tuned to get the layer thickness of 240 µm. After spin coat process, the thin layer is baked for 2 hours at 60-degree Celsius. Once the curing of PDMS was complete it was carefully cut into the micro cantilever beam dimensions. And finally, the cantilever was plasma bonded to its base. The Microcantilevers were inserted inside the wind tunnel to determine the deflection at different air flowrates. The microcantilever was placed at the midway of the test section, from the side wall of the wind tunnel, where it undergoes deflection due to the airflow interaction. The cantilever deflection was recorded using the optical microscope attached with a camera as shown in Figure 2.11(a), Figure 2.11 (b) shows the micro-cantilever beam placed inside the test section. Figure 2.11 (c) shows the schematic of experimental setup. The dimension of the test section is 100 mm in length, 18 mm in width and 12.5 mm in depth. The advantage of having a honeycomb structure in the wind tunnel can be easily investigated when the micro cantilever is studied. The graph below shows the importance of the honeycomb filter in the settling chamber. The honeycomb structure reduces turbulence and helps to steady the flow. Figure 2.11 (d) shows that there

is a variation in the flow in the wind tunnel before installing honeycomb screen, whereas in Figure 2.11 (e), the flow is steady with the honeycomb in place. Thus presence of honeycomb screen is really important.

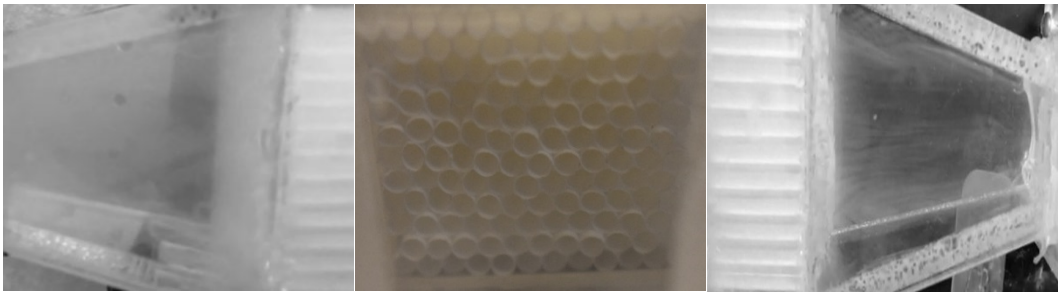

(a) (b) (c)

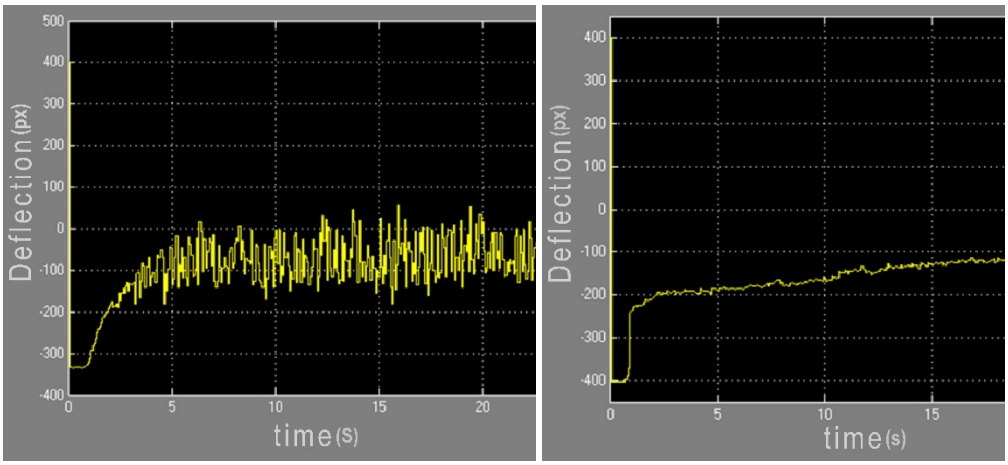

(d) (e)

Figure 2.11: (a) Wide angle diffuser section (b) Honeycomb arrangement (flow straightener),(c) Contraction section (d) Tip deflection without honeycomb structure , (e) Tip deflection with honeycomb structure.

2.9 Testing of Air flow

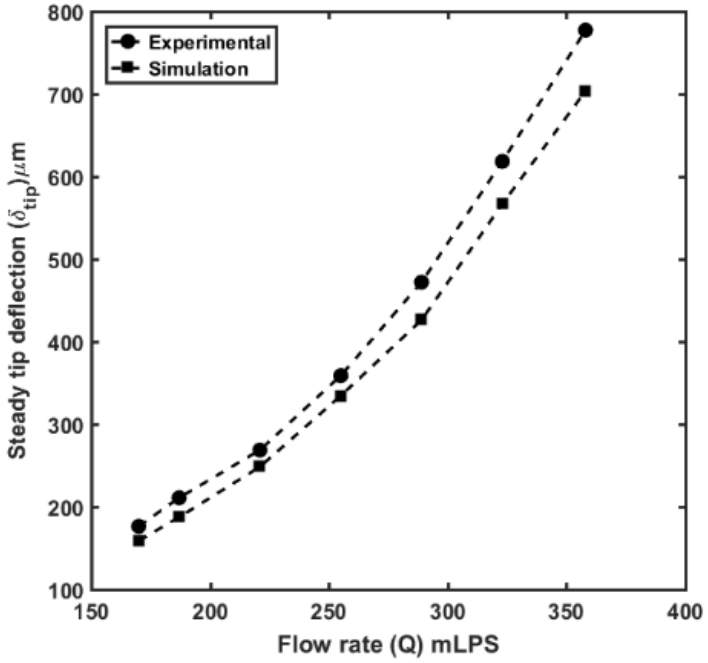

Figure 2.12: Comparison of experimental and simulation results for (a) C1

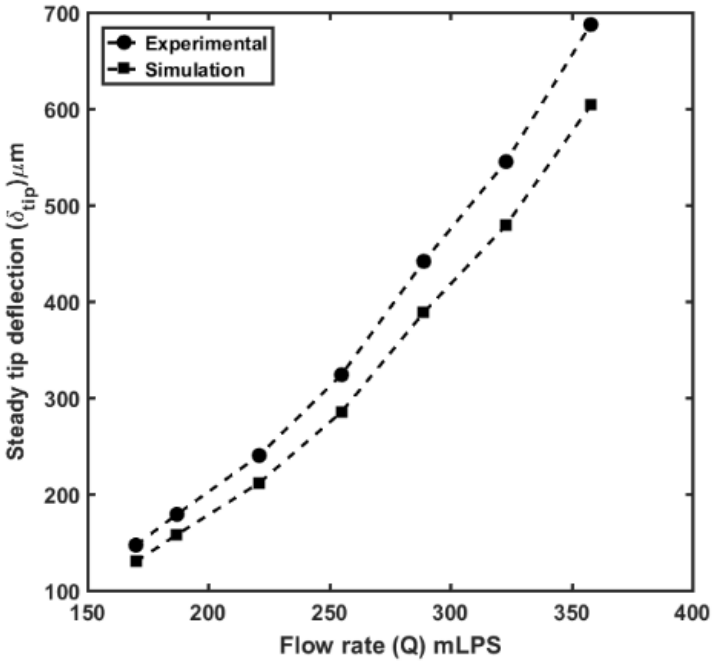

Figure 2.13: Comparison of experimental and simulation results for C4

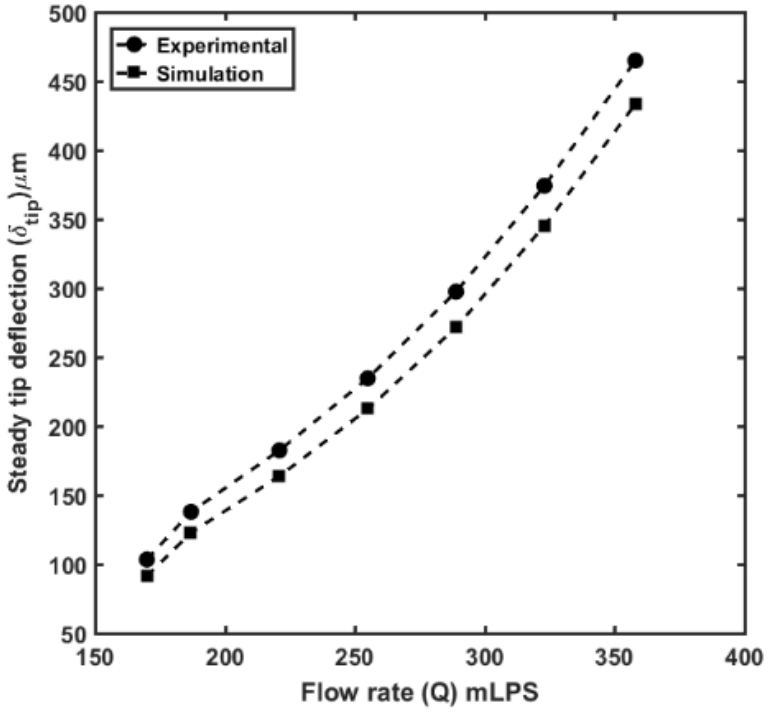

Figure 2.14: Comparison of experimental and simulation results for C7

Experimental measurement of deflection of the cantilever (3x8x0.240 mm) shows good agreement with the simulated values over the entire range of flow rate in Figure 2.12.This experiment was extended to study the air flow sensing using different micro cantilevers. For this study ten cantilevers were used to measure the deflection. The deflection of the microcantilever were tested for flowrates in the range of 160 to 360 ml/s. The dimensions of cantilevers used are listed in Table 1.The difference between experimental and simulated deflections for different cantilevers were about 10% and show that the simulation model can be used for further investigation to see the cantilever deflection. All the cantilevers were tested, using the COMSOL simulation to validate the experimental results. Figure 2.13 and Figure 2.14 show the experimental and simulation values of tip deflection micro cantilevers of dimensions 4x08x0.24mm and 5x08x0.24mm, respectively

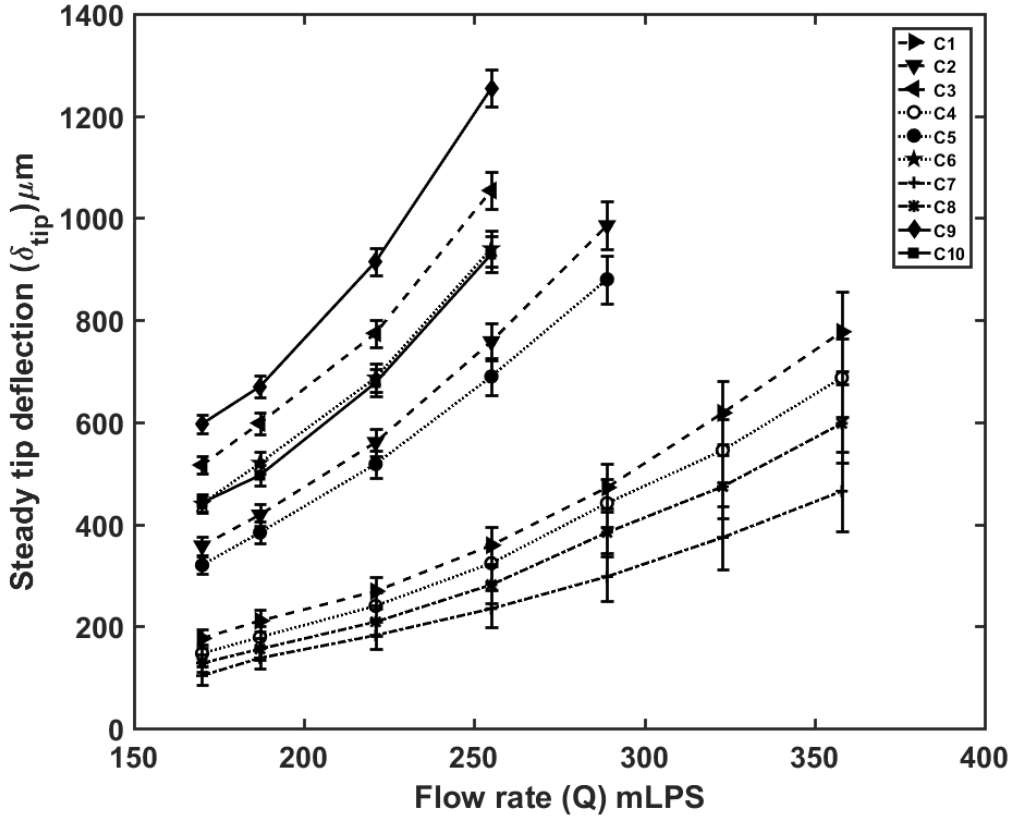

Figure 2.15: Tip deflection as the function of flowrate

From these experiments, we obtain the variation of tip deflection against flow rate Figure 2.15, show that the tip deflection increases with the length of the cantilever. The error bar is in the Figure 2.15, shows the range of values obtained over three trials. The influence of the length of the microcantilever over the tip deflection is more as compared to that of width. The microcantilever is under uniformly distributed fluid loading and maximum deflection is observed at the free end (tip). The stiffness of the microcantilever beam at the free end is given by the Equation 2.20. [47]

$$k_{sp} = \frac{8EIxx}{{l_b}^3} \tag{2.21}$$

where $\mathbf{k_{sp}}$ is the force per unit deflection at the tip of the cantilever beam, **E** is the modulus of elasticity of the beam material, **Ixx** is the area moment of inertia about the neutral axis of the beam cross section, and $\mathbf{l_b}$ is the length of the beam. Therefore, as the length of the cantilever increases, stiffness decreases which

causes more deflection in the microcantilever beam when subjected to air flow. To study the effect of length, width and thickness of the cantilever over deflection, study was grouped as following:

a) Variation of length with constant width and thickness
b) Variation of width with constant length and thickness
c) Variation of thickness with constant length and width

Table 2.1: Cantilever name and dimensions

Name	Beam dimensions (Width x Length x Thickness) (mm)
C1	3x08x0.24
C2	3x10x0.24
C3	3x12x0.24
C4	4x08x0.24
C5	4x10x0.24
C6	4x12x0.24
C7	5x08x0.24
C8	5x10x0.24
C9	4x10x0.16
C10	5x10x0.16

2.9.1 Effect of length on deflection

Equation (2.20) suggest that the beam length L_b has strong influence on beam tip deflection as, $k_{sp} \propto {l_b}^{-3}$. Hence the effect of beam length over tip deflection was studied using micro- cantilever beam with length 8 mm, 10 mm and 12 mm. The study of deflection of cantilevers based on variable length yielded the results that, as the length of the cantilever increases, the deflection increases. It is true for the entire

range of flow. At higher flowrate the deflection is huge, and the experiment is limited to maximum deflection of 1200 μm and the corresponding flowrate is 250 ml/s. as shown in Figure 2.16.

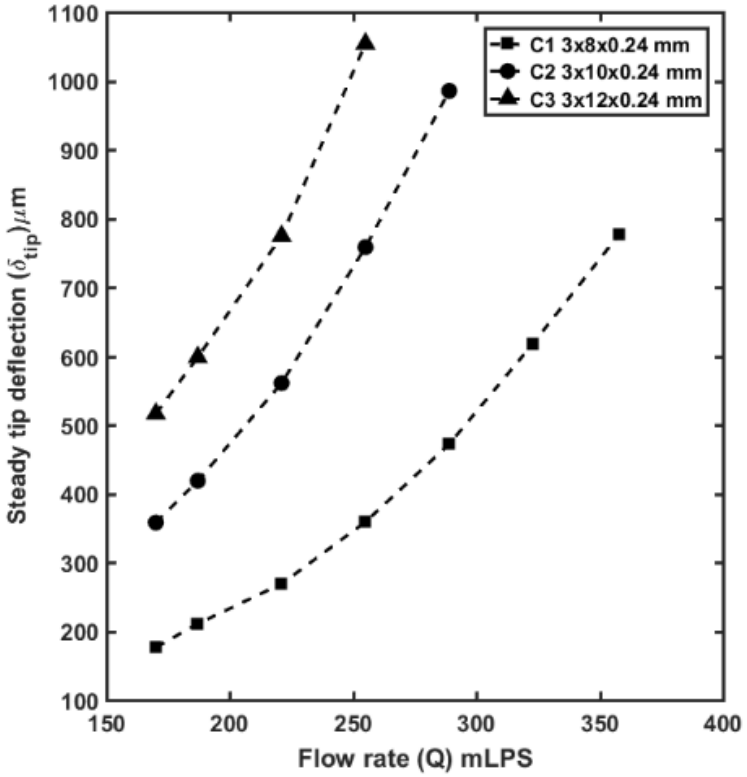

Figure 2.16: Effect of length of the microcantilever over tip deflection

2.9.2 Effect of width on deflection

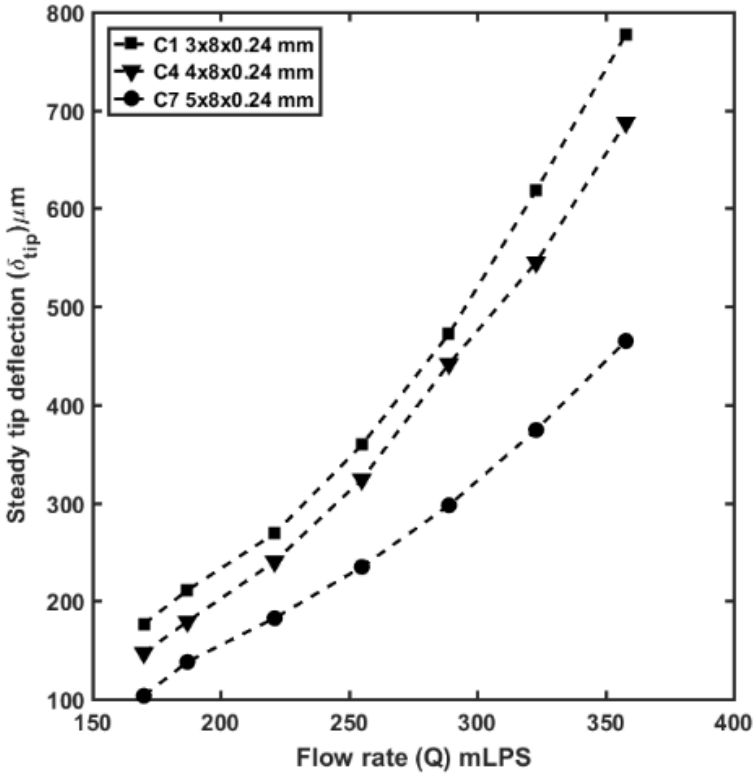

Figure 2.17: Effect width of the microcantilever over tip deflection

Effect of beam width on steady tip deflection was studied by examining the deflection of micro-cantilever beam with of 3 mm, 4 mm and 5 mm. Constant length and thickness of 8 mm and 0.24 mm, respectively, were chosen to study the effect of width because it is possible to examine the deflection of these cantilevers over the entire range of the flowrates. The maximum deflection can be observed for cantilever C1, which is the narrowest beam, 800 μm for the maximum flowrate of 360 ml/s. This observation is consistent for entire flow range. From the Figure 2.17 it can be observed that as the width of the cantilevers increase, the deflection decreases. Because the moment of inertia in Equation (2.20) calculated as, $Ixx=\left(\frac{w_b th_b^3}{12}\right)$, w_b and th_b are beam width and thickness, respectively. Hence stiffness of the cantilever is directly proportional to its width. Thus, wider cantilever offers relatively more resistance to the deflection.

2.9.3 Effect of thickness on deflection

As the thickness of the cantilever is reduced, it is observed that the thinner cantilever deflects more. However, because the deflection remains in the range of 400 μm to 1200 μm, thinner cantilevers provide better visualization of flow rates between 160 ml/s to 250 ml/s (lower flowrates). It can be understood from Figure 2.18 that cantilever C9 is highly sensitive to deflection in this flow range which makes it easier to visualize under the microscope.

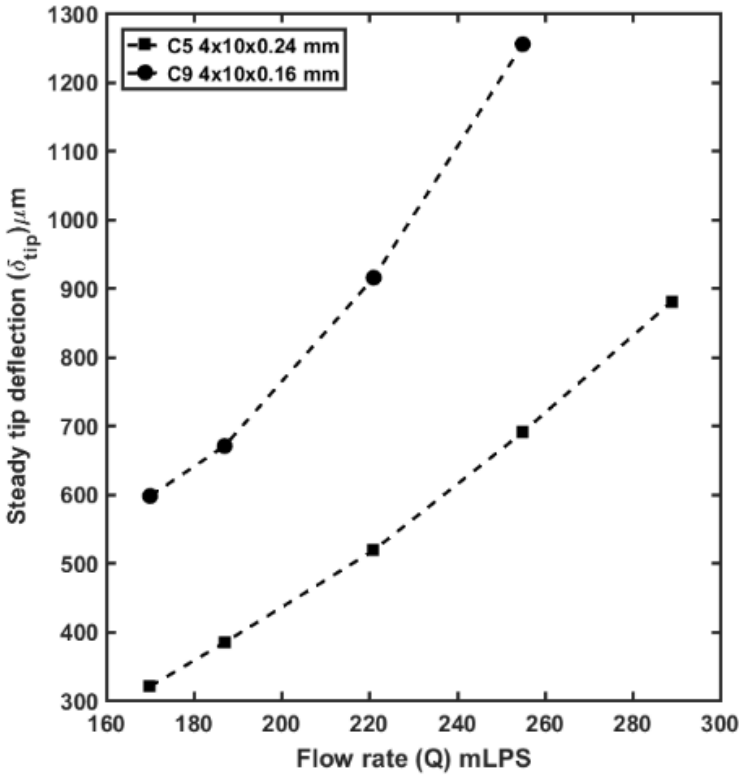

Figure 2.18: Effect of thickness of the microcantilever over tip deflection

2.10 Conclusions

An open loop low speed mini wind tunnel is designed and built to study the fluid interaction of micro structure after examining various potential designs. The proposed mini wind tunnel has total size of 360x48x40 mm with laminar flow inside the test section (Re < 1500). Laminar flow simulation was

conducted for the whole wind tunnel to understand the behavior of the flow inside the wind tunnel. Flow behavior is found to be satisfactory for testing microstructures. Additionally, total pressure loss along the mini wind tunnel was found by calculating pressure loss coefficient for individual sections.

Fluid microstructure interaction study was conducted using Micro-cantilever beam and mini windtunnel. PDMS micro cantilevers, of various aspect ratios, were fabricated using spin coating technique. Steady tip deflection of microcantilever were studied for flow rates up to 430 mL/s. The influence of beam length, width and thickness over tip deflection were experimentally studied by varying length between 8mm to 12 mm, width between 3mm to 5mm and thickness between 0.24 and 0.16mm.Obtained result suggest beam length is strong function of tip deflection which agree with theory. Furthermore, simulation study of fluid-microstructure interaction inside the test section of the mini wind tunnel was carried using COMSOL MULTIPHYSICS 4.2. The simulated results were compared with experimentally obtained values. The experimental results are in good agreement with results obtained using simulation. Thus the presented mini wind tunnel model can be used to perform further studies in fluid micro structure interaction.

Chapter 3| Experimental studies on deformation of oil coated droplets under fluid loading in mini wind tunnel

Abstract

Dynamic behavior of liquid drops under fluid flow explains many phenomena including cell adhesion. To mimic the lipid bilayer-cell nucleus, liquid-liquid bell profile droplets from oil-water mixture were considered. Experiments are carried out to measure the deformation of liquid drops under laminar fluid flow. A low speed mini wind tunnel is used for the study. It was found that liquid droplet deforms with its contact line fixed up to critical velocity. Beyond critical velocity, droplet starts shedding. Factors influencing the deformation of liquid droplet such as fluid velocity, droplet volume, interfacial tension, viscosity of the liquid were studied and presented here.

3.1 Introduction

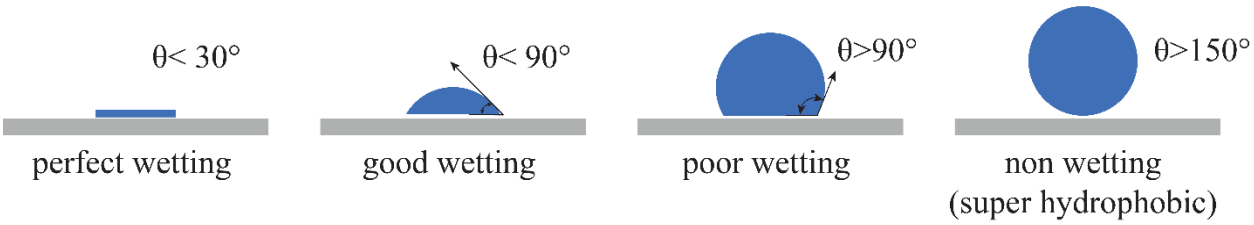

Figure 3.1: Droplet wetting regime on solid surface

A droplet resting on horizontal surface is called sessile drop. Droplet attachment to solid surface is due to the adhesive nature exhibited by the solid surface. Based on water repellency, the surface can be divided into two, namely, hydrophilic and hydrophobic. Hydrophilic is the type of solid surface where, the liquid spreads over the solid surface and this phenomenon is called *wetting*. Hydrophobic surfaces are, in general, any water repellent surfaces. However, surfaces that are extremely water repellent are called super hydrophobic surfaces. Water repellency of the surface is exhibited by the contact angle that is formed with the sessile drop. Figure 3.1 shows that water droplets are in perfect spherical shape on a super hydrophobic surface. As the water repellency of the surface decreases shape of sessile drop changes from perfect spherical to hemisphere, half ellipsoid and eventually a thin line.

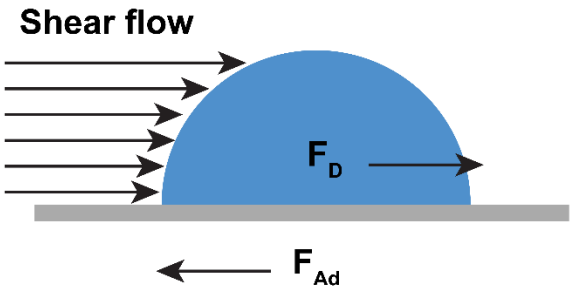

Figure 3.2: Sessile drop under shear flow

Dislodgment of droplet resting on super hydrophobic surface is easy. Even a slight tilt in surface will disturb the equilibrium and droplet will roll along the surface [48] [49]. On the other hand, dislodgement of droplet from hydrophilic surface is difficult because the droplet is held by strong surface forces exhibited by solid surface [50]. There are several means by which a drop can be dislodged from the solid surface. One such method is applying a shear flow [51]. When shear flow is applied, equilibrium contact angle will change and advancing angle and receding angle will differ. Now the droplet is under the influence of two kinds of forces. Adhesive force (F_{Ad}) between solid surface and droplet and drag force (F_D) due to fluid flow as shown in Figure 3.2. For a drag force below adhesive force, droplet will deform with its contact line fixed and hold an equilibrium shape for a given steady flow [52]. The adhesive force and maximum deformation before dislodgement is different for droplets of different sizes and liquids. It is true that for any value of $F_D > F_{Ad,}$ droplet will dislodge. However, if the shear flow is unsteady droplet may break into several tiny droplets. Hence it is important to know fluid velocity where $F_D = F_{Ad}$ also known as *point of incipient motion*. Thus, study of deformation of water droplet under shear flow is useful in understanding processes such as cell adhesion [14], droplet dislodgment in oil industry [52] and droplet formation in Proton exchange membrane fuel cell [21] [20] [53]etc.

Droplet deformation and dislodging have been studied for processes that involve water droplet accumulation. However, there has been no known experimental work done in an effort to understand the extent of deformation of oil coated water droplets before dislodgement. The closest study to this problem was carried out by Antony et al in 1999 [54]. In a numerical study, a pressure driven shear flow was

considered and magnitude of deformation above which no equilibrium shape exists, was studied. This study included the maximum deformation for stationary as well as moving droplets. The deformation was expressed in terms of ratio of initial arc length to final arc length of the droplet. E.C Kumbur et al [19] studied the droplet accumulation and dislodgment using air flow. Their study involved removal of water droplets attached to fuel cell diffusion media. An external air flow was used to remove water droplet attached to microchannel. It was found experimentally that droplet of higher aspect ratio can be removed with less difficulty. In a numerical study carried by Dimitrakopoulos [55], the magnitude of deformation of droplet attached to solid surface was tested. Prime objective of this study was to understand the location in contact line where violation of equilibrium condition ($\theta_R \leq \theta \leq \theta_A$) is first observed. It was found that droplet size plays key role in droplet deformation. For a smaller droplet, the violation of equilibrium condition occurs equally near the advancing as well as receding ends while for larger drops the violation first occurs near leading end. This is due to the additional gravitational force acting on drop due to its size. It can be noted from this study that, a droplet with low or high contact angle, will spread or roll, respectively, upon the application of external fluid flow, whereas droplets with intermediate contact angle, $80^\circ \leq \theta \geq 120^\circ$ show significant stability even in the presence of a steady fluid flow. In another numerical study carried by same author in 2007 [56], effect of gravitational force on three-dimensional droplet deformation was studied. In this study, factors influencing droplet deformation such as initial contact angle, viscosity ratio and initial shape were considered individually. In a cell detachment model studied by Swapnil et al, [13] hydrodynamic force required to dislodge a rigid cell, normal cell and cancer cell was tested. This work involved CFD modeling along with experimental validation.

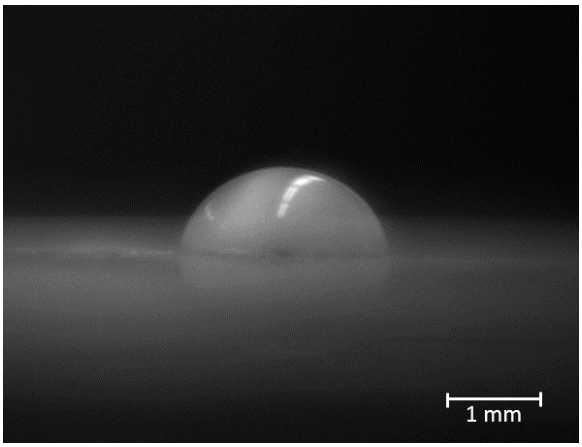

Figure 3.3: 10 µl water droplet on parafilm surface

Present study is done to understand the force exerted and thereby deformation of the water droplet under fluid flow. Hence a parafilm surface, where the contact angle of water droplet is approximately 115˚, was chosen as test surface. Figure 3.3 shows a 10 µL sessile droplet over parafilm surface. To imitate the lipid bilayer and cell nucleus system, droplets made from mixture of silicone oil and water, an immiscible solution, were considered. The resulting droplet holds a liquid-liquid bell shape, like cells, upon placing on the solid surface. Young's modulus of a healthy cell is around 3000 N/m^2 whereas that of unhealthy cell is about 10000 N/m^2 [13]. Hence the extent of deformation can be used to distinguish between healthy and cancerous cell since the latter being rigid, would deform less under fluid flow. In most of the droplet deformation studies, it was found that factors such as volume, interfacial tension, and viscosity ratio have effect on droplet deformation. Silicone oil-water combination provides easy way to study the effect of such properties over deformation, simply by varying relative concentration of silicone oil and water in a droplet.

3.2 Theory

The shape assumed by sessile drop depends on factors such as, surface energy, surface tension of the liquid, ambient temperature and surface roughness [26] [57]. Shape of the sessile droplet is determined by properties, called wetting characteristics. They are contact angle (θ), wetting length (lw), drop diameter (d_d), contact line length (lc) as shown in Figure 3.4 (a).

Contact angle (θ): Angle between the horizontal surface and side emerging from the surface at either side of the drop. Wetting length (l_w) is the length over which the drop is making contact with horizontal surface.

Drop radius (r_d) is the radius of the drop measured along the direction normal to horizontal surface. Contact line length (l_c) is the perimeter of the contact disk formed by the droplet and surface.

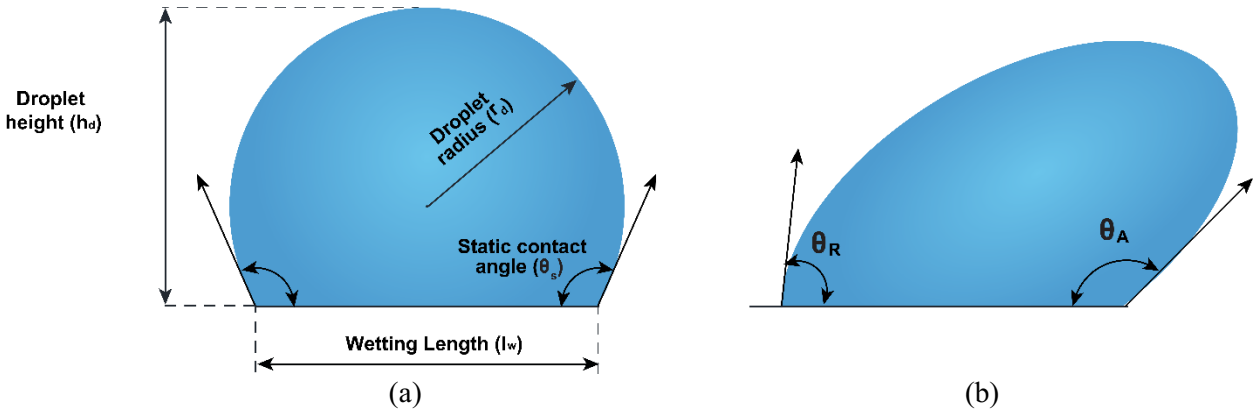

Figure 3.4: Sessile drop on horizontal Surface (a) Static (b) under fluid flow

Young's Equation is used to determine the contact angle (θ), given by the Equation (3.1)

$$\gamma_{SL} + \gamma \cos\theta_Y = \gamma_{SV} \tag{3.1}$$

where,

γ_{SL}-Interfacial tension between solid and liquid

γ-Interfacial tension between liquid and vapor

γ_{SV} -Interfacial tension between solid and vapor

θ_Y – Equilibrium contact angle

Adhesion force

$$F_{AD} = l_c \gamma_{LV} (\cos\theta_R - \cos\theta_A) \tag{3.2}$$

where,

lc - Length of the contact line

γ - Surface tension

θ - Contact angle

Drag force

$$F_D = \frac{1}{2} \times \rho \times v_{avg}^2 \times A_{ps} \times C_d \quad (3.3)$$

ρ_a - Density of the air

v_{avg} –Velocity of air

Aps – Projected area of the droplet facing the fluid flow

C_D - Drag Coefficient

Equations (3.2)and (3.3) can be rearranged to get C_D as

$$C_d = \frac{2\gamma_{LV} l_C (\cos\theta_R - \cos\theta_A)}{\rho A_{ps} v_{avg}^2} \quad (3.4)$$

3.3 Experimental Setup

Droplet deformation experiments were performed using a mini wind tunnel as shown in Figure 3.5 Liquid solution of different silicone oil-water concentrations (0, 10, 20, 40% v-v) were prepared. For example, 5ml 10% oil - water solution was prepared by mixing 0.5ml silicone oil in 4.5 ml water. Liquid drop was placed on test surface using a micro pipette. Test surface was prepared by attaching thin film of parafilm on to 15x 18x 1 mm microscopic glass. Droplet sizes of 5 µl, 10 µl, 15 µl, 20 µl were considered for the study. Droplet deformation was tested between the flow velocities of 0.75m/s – 1.5m/s inside the test section. Flow velocity was controlled by regulating fan voltage of the mini wind tunnel. Droplet

deformation was recorded using a high-speed camera. Duration for each experiment was about 110 s since fan transient time is 100s. Also, this time serves as equilibrium time for oil-water droplet.

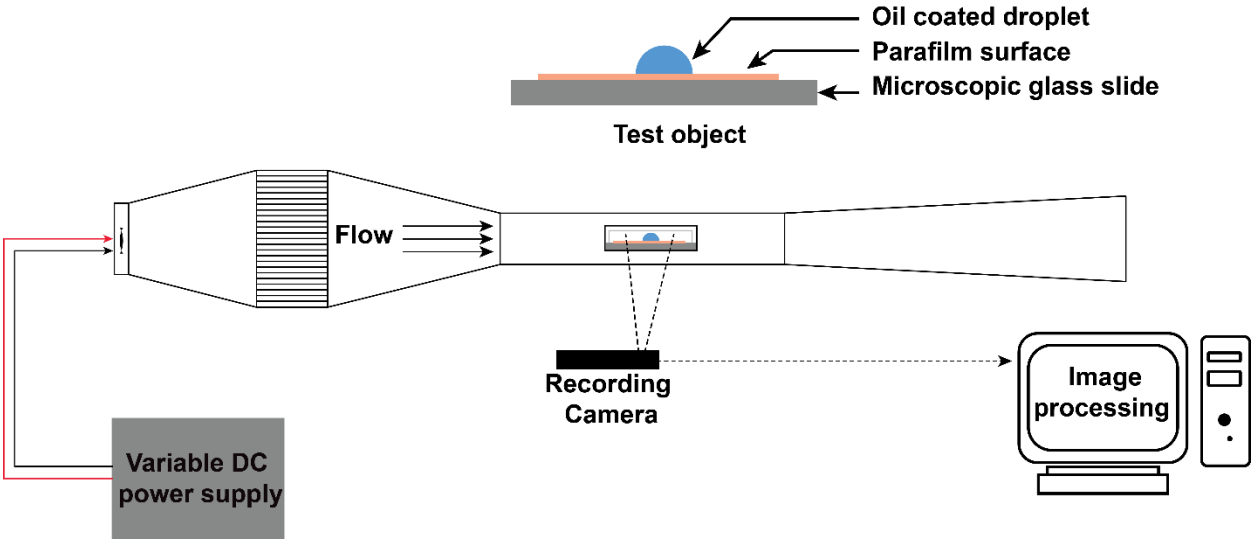

Figure 3.5: Schematic of experimental set up

A simple image processing technique was used to find droplet deformation. Two images from the recordings were captured, one before the air flow and another one after the transient time. Deformation of droplet, which is the change in the shape of droplet in side view along x direction was found by comparing those two images see Figure 3.6.

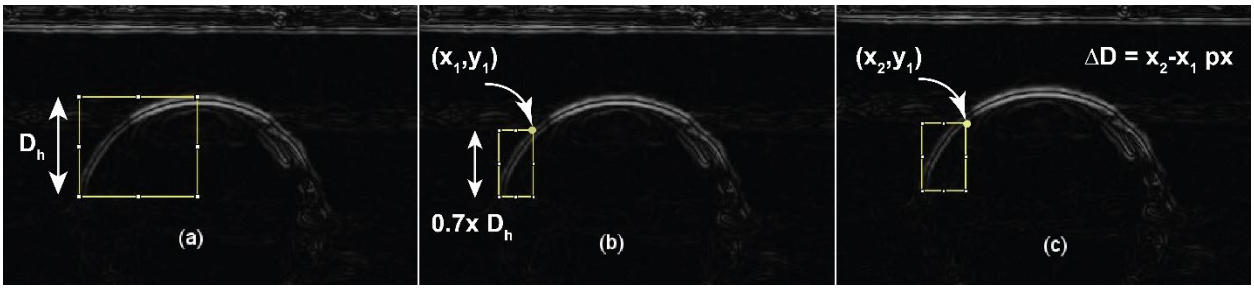

Figure 3.6: Experimental determination of droplet deformation

3.4 Results and Discussion

Factors affecting droplet deformation such as fluid flow rate, droplet volume, and oil concentration were studied.

3.4.1 Effect of fluid flow on droplet deformation

Deformation of droplets was tested for the fluid velocity between 0.75 m/s to 1.5 m/s. Fluid velocity inside the test section was increased from 0.75 m/s to 1.5 m/s by changing fan input voltage. Higher fluid flow induces higher drag force on droplets. Hence deformation increases in liquid droplets as the fluid flow increases. Figure 3.7 shows the effect of fluid flow over droplet deformation. Initially, deflection of 5µL water droplet (X_{oil} = 0%) was tested. Droplet deflection at receding end (δ_R) of 200 µm was observed for v_{avg} : 0.75m/s

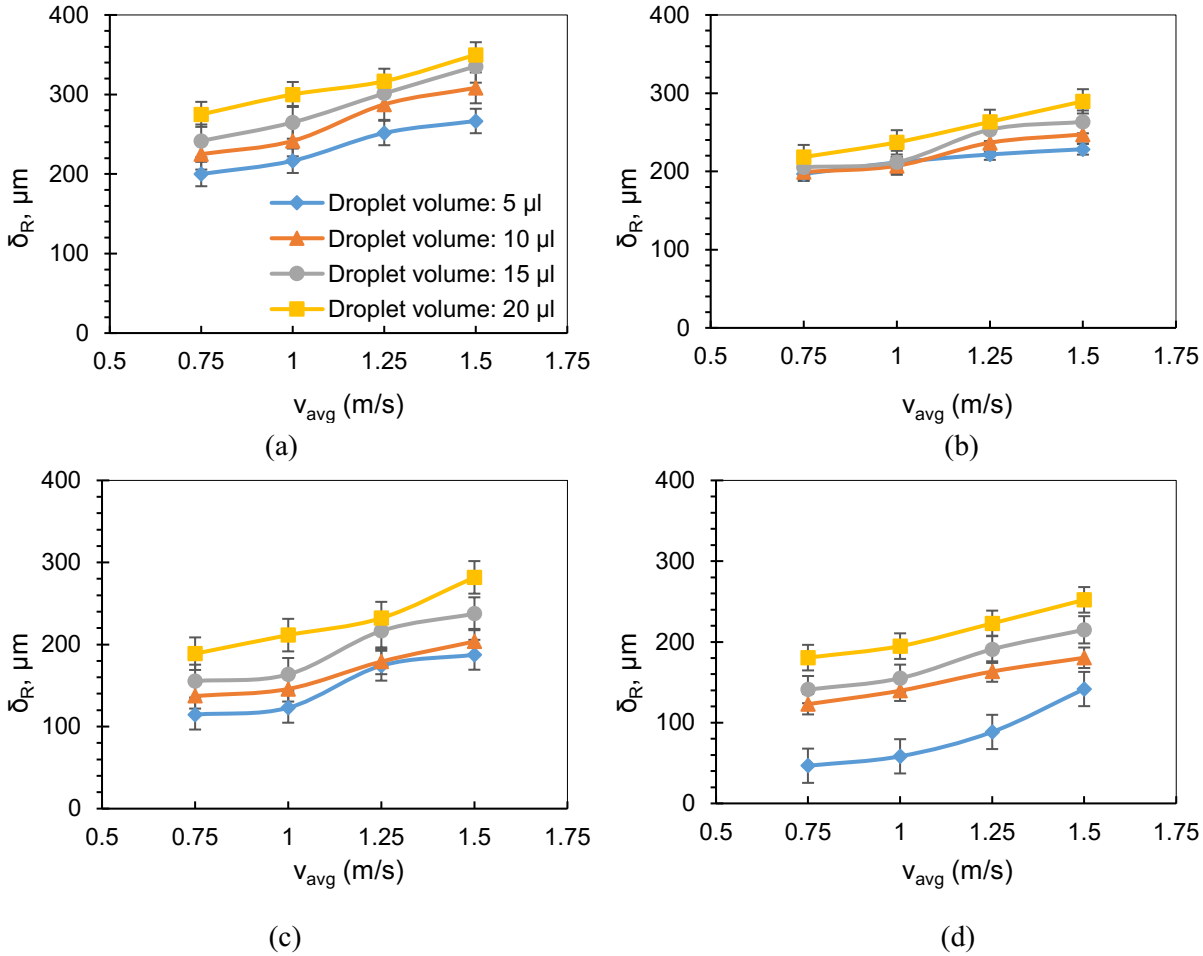

Figure 3.7: Deformation of water droplet as function of fluid velocity (a) X_{oil} = 0%, (b) X_{oil} = 10%, (c) X_{oil} = 20% and (d) X_{oil} = 40%

A new liquid droplet was placed inside the test section to test deflection of 5µL at higher flow velocity 1.00 m/s. As a result of higher fluid flow, droplet deflection increased to 216 µm. Experiment was repeated to

test deflection of 5µL droplet at higher flow velocities. Each test was carried out with a new droplet. Tests for each droplet volume, each flow velocity and each oil concentration were repeated three times and arithmetic average of the results from three trials plotted with fluid velocity as function of droplet deflection. The error bars in the Figures show the range of values obtained over three trials.

3.4.2 Effect of droplet volume on droplet deformation

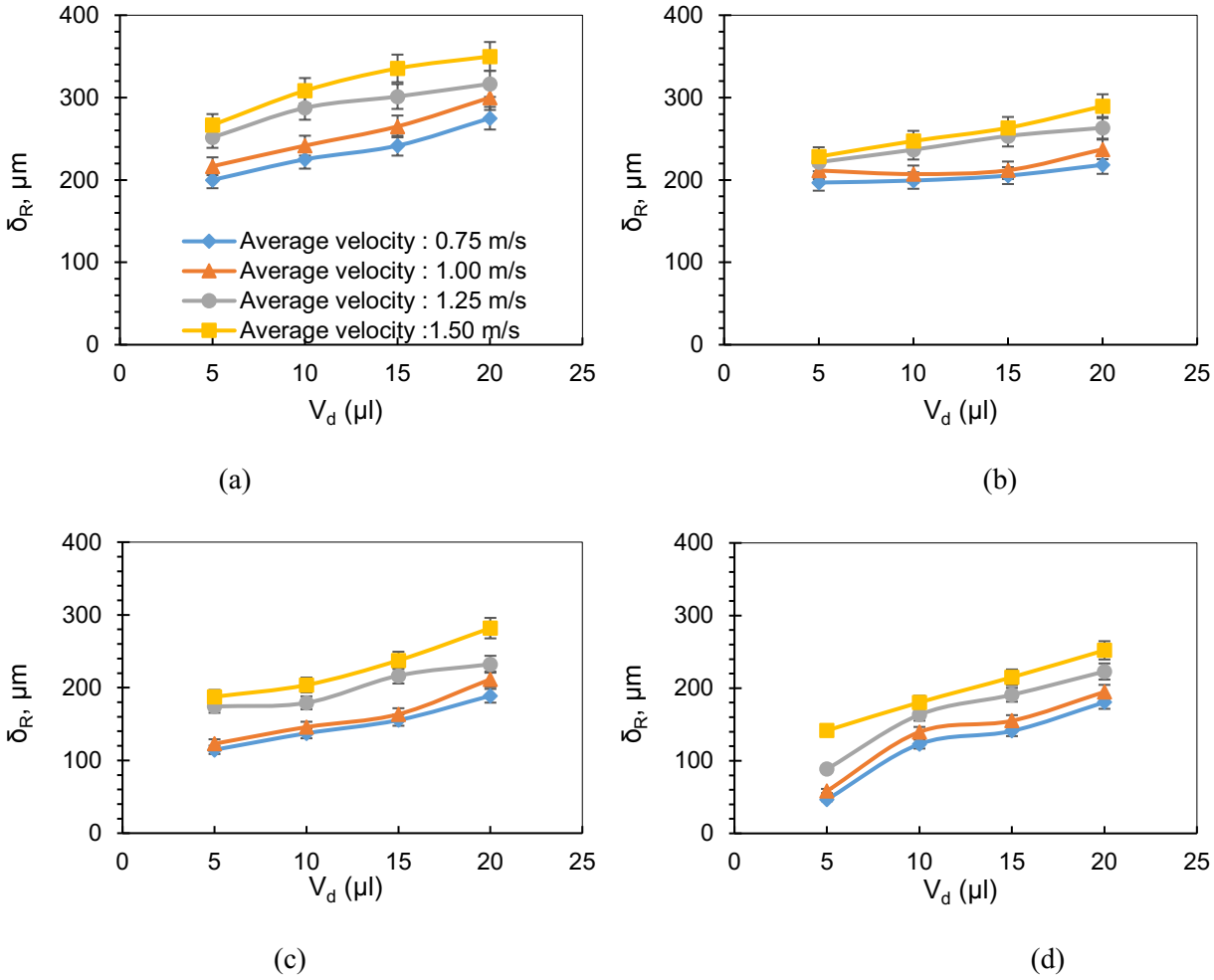

Figure 3.8: Deformation of water droplet as function of droplet volume (a) X_{oil} = 0%, (b) X_{oil} = 10%, (c) X_{oil} = 20% and (d) X_{oil} = 40%

Droplet volume influence on droplet deformation was studied by examining deformation of water droplets of sizes 5,10,15,20 µL. Smaller droplets deform less as compared to larger droplets see Figure 3.8. Deformation of 5µl droplet, with X_{oil} = 0% is 200µm for v_{avg}: 0.75 m/s, as compared to the same of 20µl is

275µm.See Figure 3.8(a). Smaller droplets are under the influence of surface forces. Droplets with larger volume offers higher projected surface area facing the fluid flow. Experiencing higher drag force, larger droplets undergo higher deformation. This observation was consistent across all the oil concentrations. See Figure 3.8 (b) (c) (d).

3.4.3 Effect of oil concentration

Introduction of oil brings two features. Firstly, the oil layer acts as a protective cover. However, increasing oil concentration will not increase the thickness of the cover. Instead excess oil will form a wetting ridge, by spreading around the droplet base, see Figure 3.9. Due to this wetting ridge the contact angle of the droplet further decreases and the ability of the droplet to deform decreases. Influence of surface forces reduce as the oil concentration increases. The moment oil coating is introduced, deformation of droplet decreases significantly. The steep decrease in deformation values, between oil concentration (X_{oil}) =0% to X_{oil} = 10%, for the droplets 15µL and 20µL Figure 3.10 (c) and (d) suggests that oil gives stability to the droplets.

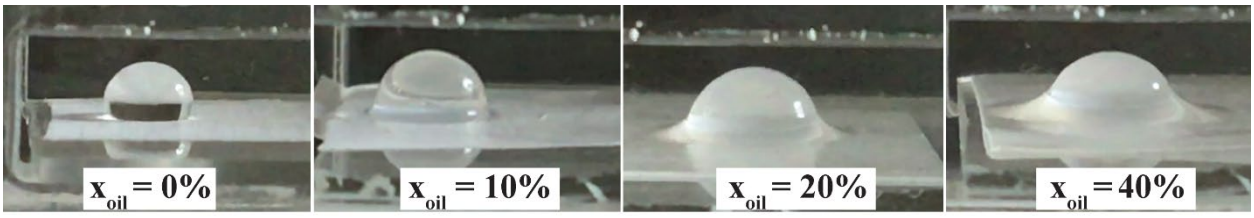

Figure 3.9: Wetting ridge formation with oil concentration

However smaller droplets are an exception for this observation as the amount of oil present in this case is less. Reduced deformation in droplet would mean two things. Either the droplet has deformed to maximum values. Further increases in fluid velocity will break the liquid droplets or the liquid droplet is at its point of incipient motion and it will start oleoplaning (droplet sliding under the influence of oil).

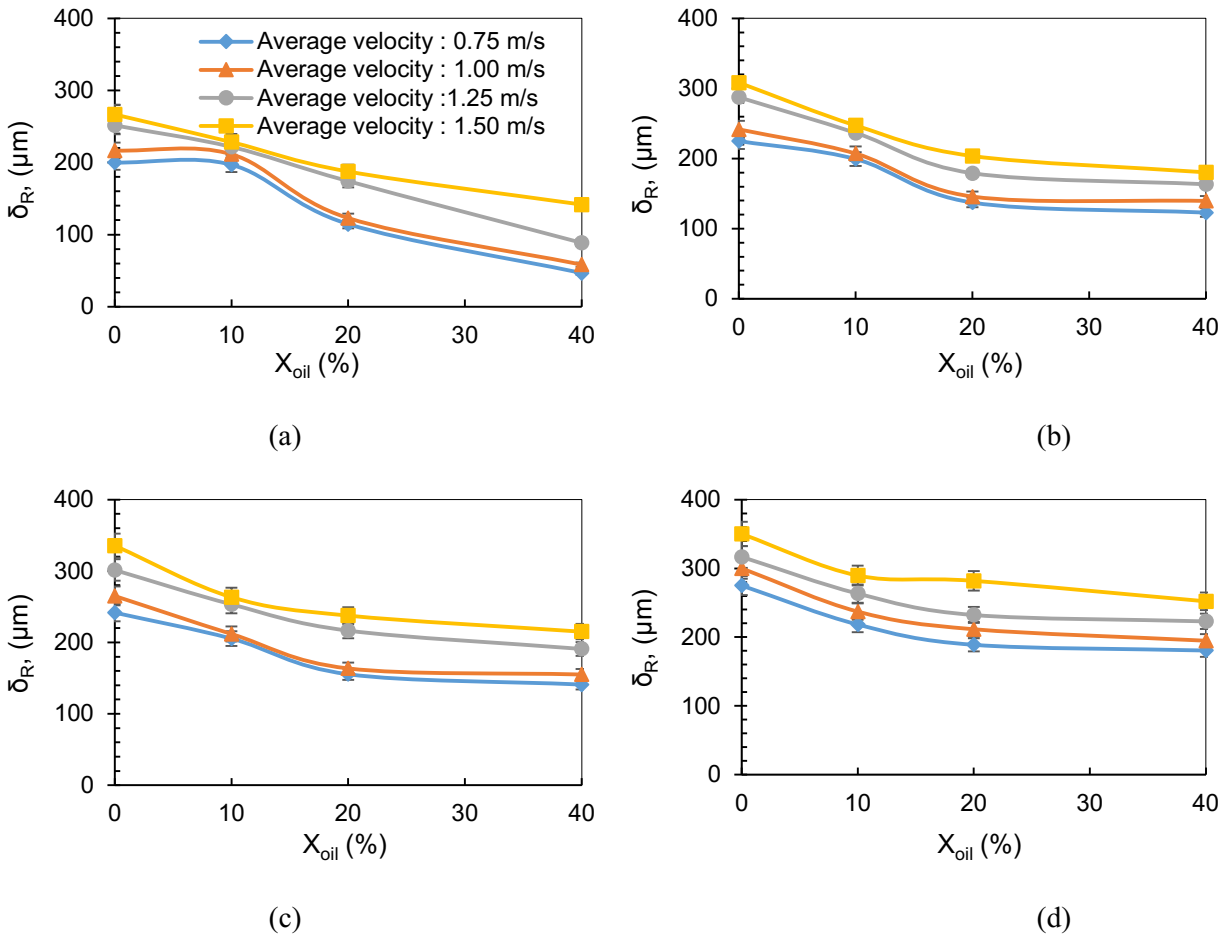

Figure 3.10: Deformation of water droplet as function of oil concentration (a) V_d = 5µl, (b) V_d = 10µl, (c) V_d = 15µl and (d) V_d = 20µl

Evaporation of water due to air flow is inevitable. Shape change of droplet due to evaporation should also be considered to accurately estimate the deformation of droplet. Hence, shape change of droplet at both advancing and receding end were checked. Overall deformation in receding end (δ_R) is sum of evaporation and deformation due to air flow (δ_d) while the same at the advancing end (δ_A) is due to evaporation only, Droplet deformation schematic shown in Figure 3.11. Testing the shape change of droplet at advancing end enables to accurately assess actual droplet deformation. A term φ, defined as $\frac{\delta_R - \delta_A}{\delta_R}$, is used to explain the shape change of droplet due to pure deformation. Value of φ ranges between 0 (i.e $\delta_R = \delta_A$, only evaporation)

to 1 (δ_A = 0 or δ_R >>δ_L, shape change is only due to deformation or droplet deformation is principally responsible for shape change of droplet).

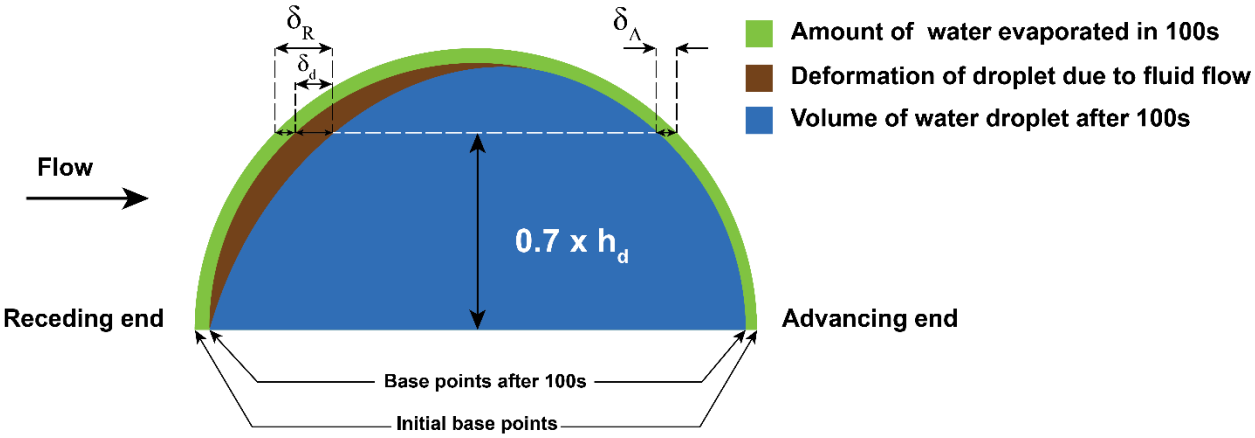

Figure 3.11: Droplet deformation schematic

Evaporation of water is mainly due to the air flow. Air at room temperature 22° C and relative humidity 30 % is blown past oil coated droplet for 100s. Rate of evaporation is function of surface area (A_{ps}), fluid velocity (v_{avg}) and room temperature (T_r). Laboratory room is air conditioned space, hence rate of evaporation is primarily function of surface area of the droplet and fluid velocity. Surface area of the droplet increases with droplet volume (V_d). Figure 3.12 shows the change in droplet shape at receding end. The evaporation is higher in the case where X_{oil} = 0%. Droplet evaporation drops significantly as the oil coating is introduced. Silicone oil is less volatile than water, rate of vaporization is very low as compared to droplets where X_{oil} = 0%. As it can be observed from Figure 3.12 where the deformation of the droplet in the receding end δ_R, is large and significant as compared to deformation at the advancing end, δ_A. Values of φ is close to 0.8 for X_{oil} =0% while φ values are above 0.9 for rest of the droplet samples with X_{oil} = 10%, 20% and 40%. After considering the evaporation of water, a surface plot is presented. Figure 3.13 shows the deformation of droplet without oil coating (X_{oil} =0%). The droplet deformation (δ_d) values are slightly lower than the deformation at the receding end (δ_R) since data presented in Figure 3.13 considers the effect of vaporization. Similarly Figure 3.14, Figure 3.15 and Figure 3.16 shows the droplet deformation values for X_{oil} = 10%, X_{oil} = 20% and X_{oil} = 40% respectively.

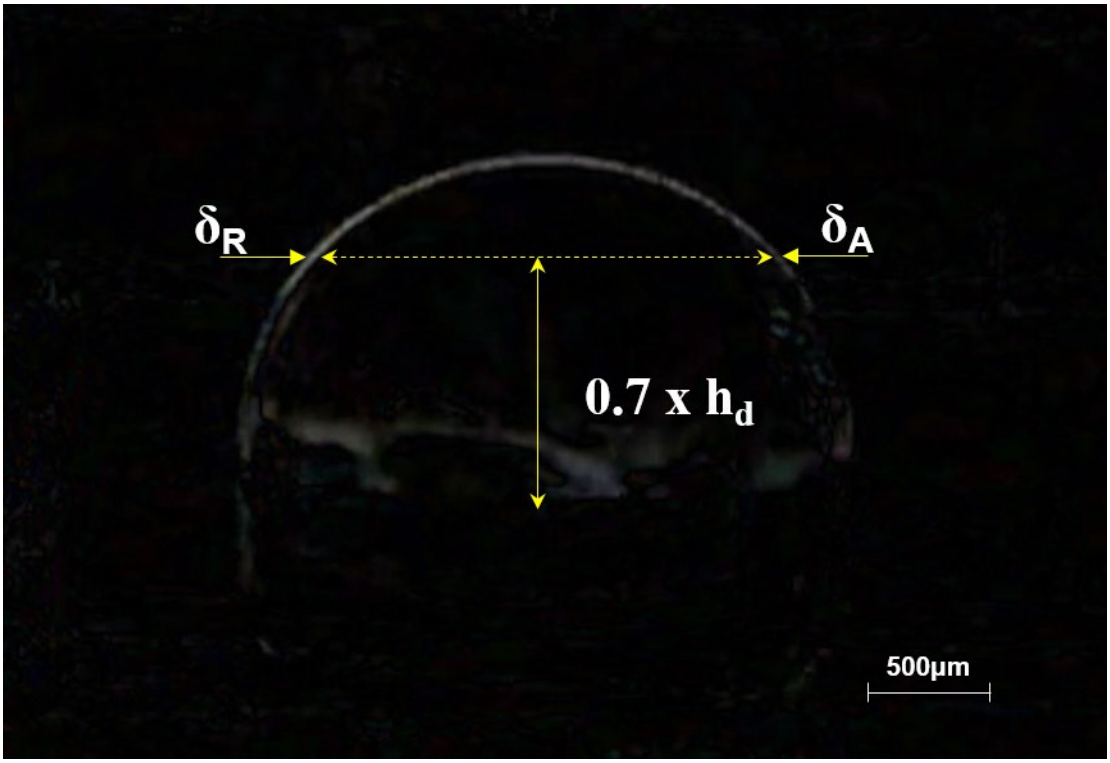

Figure 3.12: Droplet deformation vs Droplet vaporization for 20µl droplet under v_{avg}: 1.5m/s

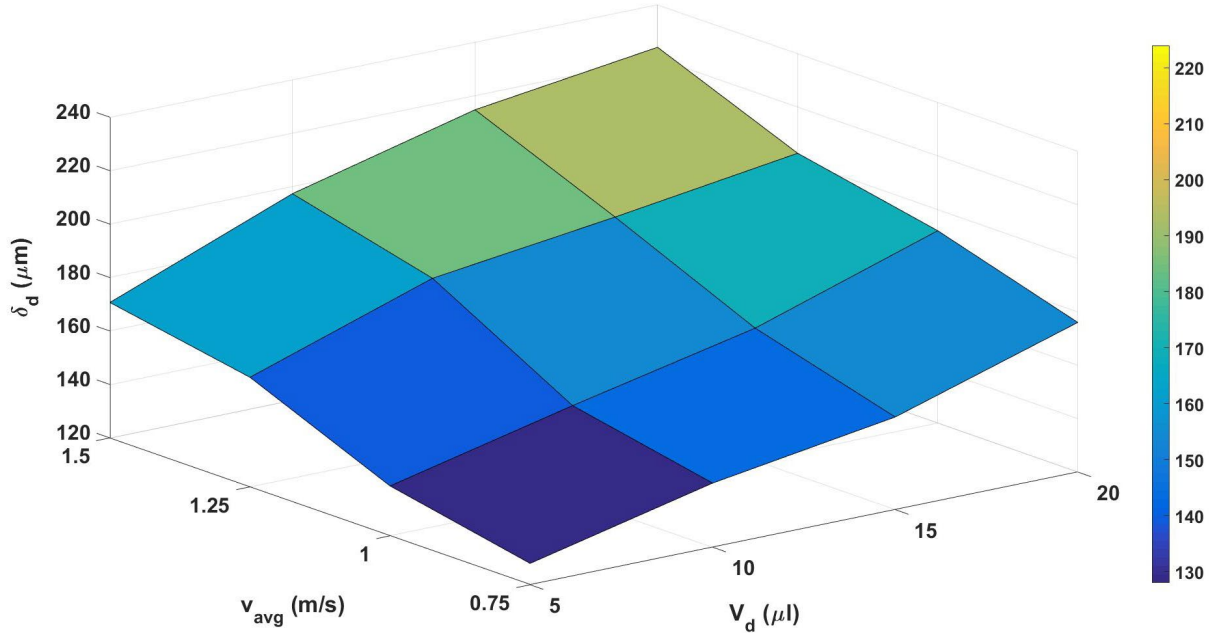

Figure 3.13: Surface plot of droplet deformation, fluid velocity and droplet volume for X_{oil} = 0%

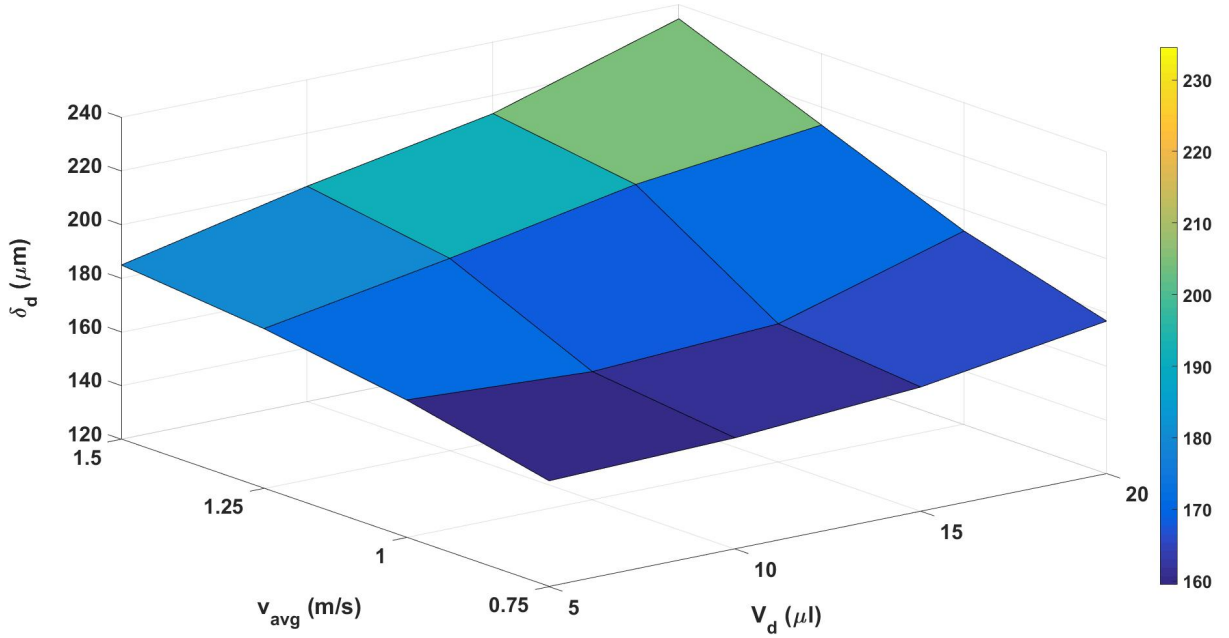

Figure 3.14: Surface plot of droplet deformation, fluid velocity and droplet volume for X_{oil} = 10%

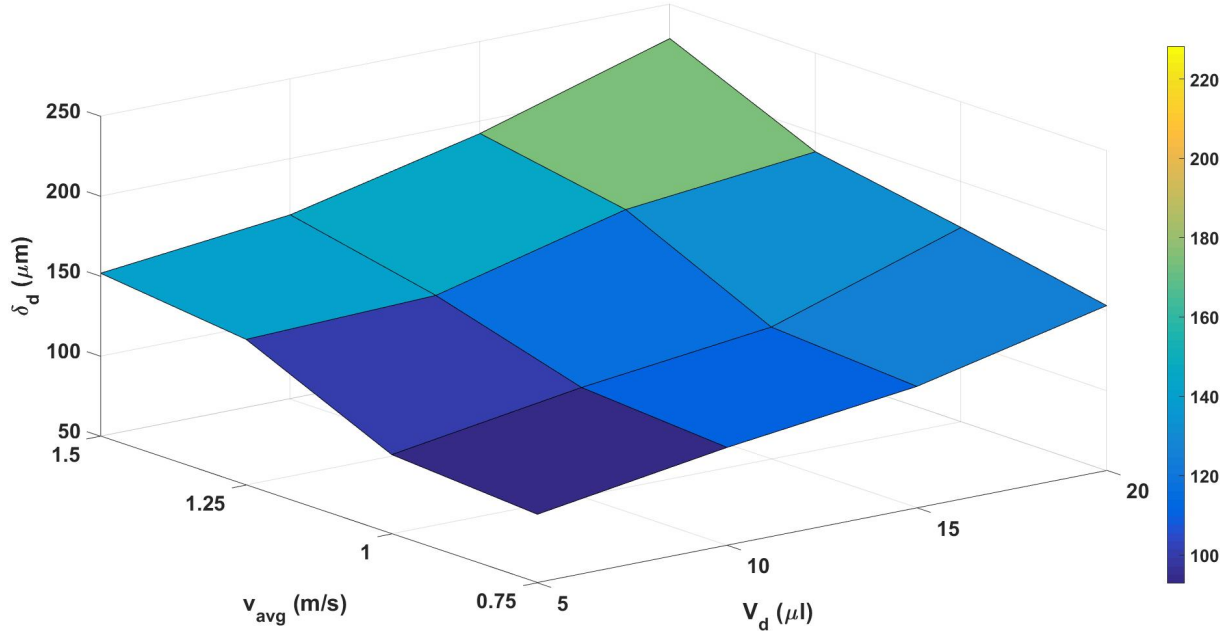

Figure 3.15: Surface plot of droplet deformation, fluid velocity and droplet for X_{oil} = 20%

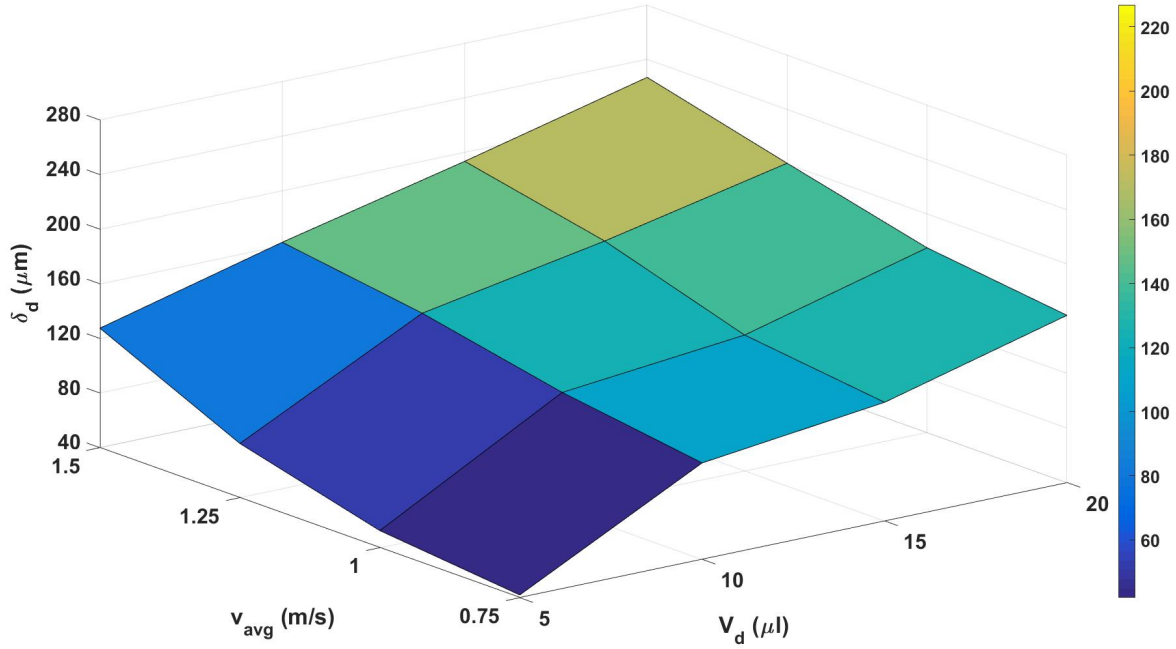

Figure 3.16: Surface plot of droplet deformation, fluid velocity and droplet for X_{oil} = 40%

3.4.4 Study of effect of fluid flow and oil concentration on dynamic contact angle

Three contact angles, static (θ_s), advancing (θ_A) and receding (θ_R) belonging to two categories static and dynamic stage were studied. Initially static contact angle of droplets were found. Oil coated droplet has two interfaces, one between oil and parafilm and second between oil and water. Silicone oil spreads in the parafilm surface, hence contact angle is measured at the oil and water interface. MATLAB based image processing technique was used to measure contact angle. Obtained values are tabulated and presented in a 2D plot. Figure 3.17 shows the changes in θ_s with respect to droplet volume for all four oil concentrations (X_{oil} = 0, 10, 20 and 40%). Static contact angle of the oil coated droplets are much lower than the one without oil ranging less than 50˚ for all the three different oil concentrations (10%, 20%, and 40%). θ_s for water over parafilm was found to be 112˚ ± 3˚ for the droplet size between 5µL to 20 µl With increase in X_{oil} static contact angle decreases. θ_s roughly dropping from 50, 45and 30˚ for oil concentration 10%. 20% and

40% respectively. Experimental study from Peter et al [58] shows that the interfacial tension of silicone oil-water mixture is lower than water (γ = 0.072mN) and closer to silicone oil (0.023mN).

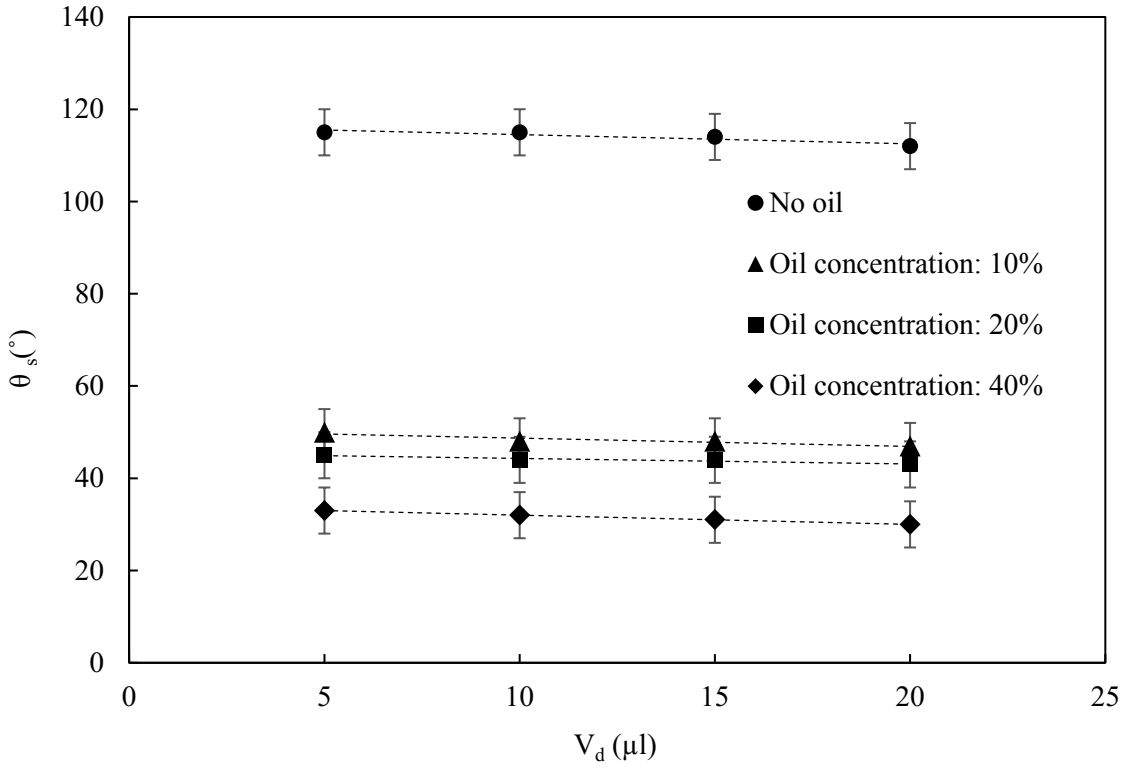

Figure 3.17: Effect of volume over θ_s

Variation of dynamic contact angles, and contact angles are studied by measuring each value with and without fluid flow. Fluid velocity (v_{avg}) at which the angles are measured were 0.75, 1.0, 1.25 and 1.5 m/s. Increasing fluid velocity increases the drag force, thus pushing the droplet further in the direction of fluid flow while the droplet is still under the influence of surface force. To resist from breaking, droplet finds a new equilibrium shape, by virtue of surface tension, in the form of a deformed droplet.

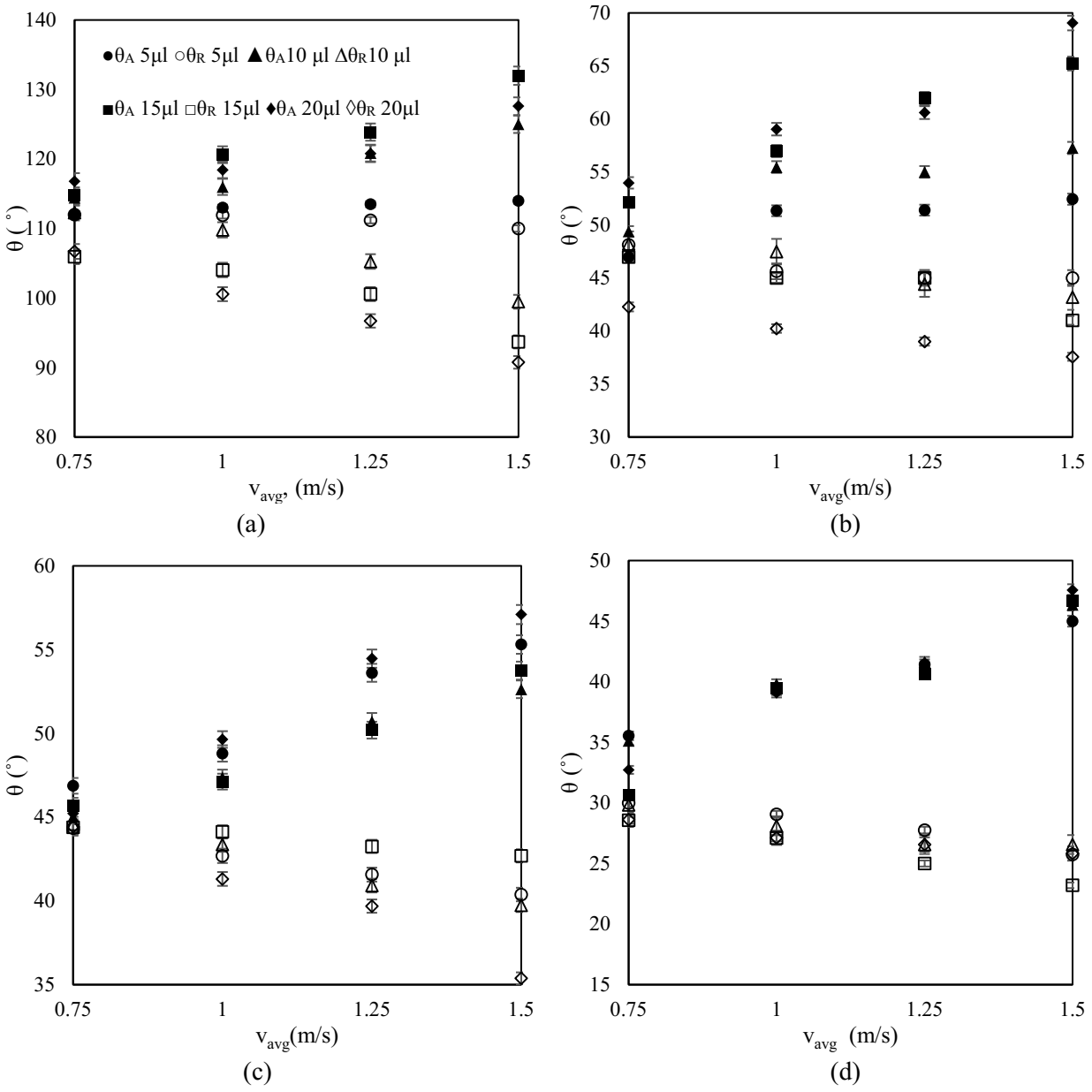

Figure 3.18: Dynamic contact angle variation with fluid velocity (a) X_{oil} = 0%, (b) X_{oil} = 10%, (c) X_{oil} = 20% and (d) X_{oil} = 40%

This deformation initiates changes in dynamic contact angle. Receding angle decreases with increase in drag force while advancing angle increases with increase in drag force. Figure 3.18 (a) shows the changes in dynamic angle with respect to flow rate for X_{oil} =0%. The dynamic angle varies with respect to flow velocity. Advancing angle increases from 112˚ to 118˚ while receding angle drops from 112˚ to 110˚.The difference between θ_A and θ_R is more for the larger droplets. This observation is consistent for droplets of

other oil concentration as well. It should be noted that $(\theta_s-\theta_R) \neq (\theta_A-\theta_s)$. Extent of rearrangement of droplet is different at either end. This change can be attributed to the viscoelastic nature the drop and the force is not completely transmitted. Figure 3.18 (b)(c)(d) show that contact angel of the oil coated droplet for X_{oil} = 10%, X_{oil} = 20%, X_{oil} = 40%. Contact angle of water at X_{oil} = 40% is less than 30° in Figure 3.18(d) suggesting that further increase in oil concentration will result spreading of water over silicon oil.

3.5 Conclusions

Experimental study on deformation of oil coated water droplets was performed using a low speed open loop mini wind tunnel. Parafilm surface, which offers intermediate wetting was used for the study. Steady increase in drag force induces greater deflection in droplets. Droplets with volume 5μL, 10μL, 15μL and 20μL were tested to examine the effect of droplet volume over deformation, it was found that smaller droplets are under the influence of surface forces. This results in less deformation as compared to larger droplets. Thus, droplet volume is inversely proportional to stability.

Effect of viscosity over droplet deformation was examined by varying oil concentration in droplets from 0% to 40%. Droplets with higher oil concentration deforms less. Viscosity of the silicone oil holds the droplet pinned to parafilm surface. Droplet has less flexibility since increase in fluid flow initiates shedding phenomena, and dislodgement of water droplet.

Chapter 4| Effect of different surface wettabilities on oleoplaning of droplets studied in mini wind tunnel

Abstract

At critical velocity water drop starts sliding along the direction of fluid flow. Oil coating on water droplets reduces the critical velocity. In this study shedding of oil coated water droplet is investigated using a low speed mini wind tunnel. Average shedding velocity of water droplet between the sizes 5-20µl was found for flow velocity of 2m/s. It was found that larger drops will shed at higher velocity. Shedding experiments were carried on two different surfaces- Parafilm and Teflon. Results suggest that Teflon surface is smooth and offers less resistance to droplet shedding. Furthermore, effect of oil concentration was studied by increasing the oil concentration from 0%-40%. It was found that average shedding velocity of water droplets with higher oil concentration is higher. However, at post optimum oil concentration the oil layer resists shedding.

4.1 Introduction

Droplet shedding is droplet dislodgement phenomena due to external fluid flow. Detailed study of droplet shedding is useful in understanding the processes, not limited to, such as cell adhesion [13], oil recovery, ice formation in plane wings [25], and water drop movement in proton exchange fuel cell [20] [21]. Droplet resting on horizontal surface will be under the influence of surface force there by sticking on to the surface. This force is called adhesive force (F_{Ad}). An external force has to be applied to dislodge the resting droplet. An external fluid flow will dislodge the droplet. However, the magnitude of drag force provided by the external fluid flow should be greater than surface forces, with which the droplet is held in horizontal surface. The drag force is a strong function of fluid velocity ($F_D \propto v_{avg}^2$) and can be increased by increasing flow velocity. It is imperative to understand the v_{avg} at which $F_D = F_{Ad}$, because large value of F_D will break the droplet into several tiny droplets, which are now more stable and making the droplet removal process tedious. The v_{avg} at which $F_D = F_{Ad}$ is called critical velocity. Critical velocity is function of droplet volume, surface roughness etc [59] [60]. Hence droplet of different volume will shed at different

velocities. Although numerous droplet shedding studies have been carried out, present study is first of its kind where the average shedding velocity of the droplet is found.

Shedding phenomena has been studied widely for various applications. In most of the cases these studies were done to understand the ice formation in aircraft wings. Naturally the shear flow that were considered were >5m/s. Mogahtadernejad et al [25] studied water drops under shear flow on surfaces with different wettability. This study mainly focuses on icing formation on airplane wings and study was mainly focused towards the wetting length, transient behavior of water drops before forming rivulets. A.J.B. Milne studied water drop shedding under shear flow inside the wind tunnel. Different surfaces such as Teflon, PMMA, SHS (Super Hydrophobic surface) were considered for the study. Shear velocities were in the range >5m/s [51] . C. Antonini established a method to analyze the adhesion force using image. Two forces acting on a drop under shear flow were considered. Adhesion force between drop and surface on which it is resting and drag force due to the flow. Antony did mathematical formulation and studied the factors that are affecting the droplet deformation. Also, he arrived at final equilibrium shape of water drop before breaking its shape [24]. P. Dimitrakopoulos did theoretical study on deformation of liquid droplets attached to a solid surface. Droplets of circular contact line were studied at different shear flows. [55]. Deepak et al studied water drops shedding on different solid surfaces under icing condition, and experimentally found the critical air velocity [26] .Periklis Papadopoulos et al found that introducing lubrication to the liquid drop helps the drop to slip at lower critical angle of tilt. Micro structured solid surface was considered for their experiment [13].

Interestingly, droplets on lubricated surface will possess lower critical velocity. This phenomenon of droplet moving under the influence of oil is called *Oleoplaning*. Joanna Aizenberg et al worked on "oleoplaning" (sliding due to oil) of droplets on lubricated surfaces. Horizontal surfaces were considered for their experiment and silicone oil was used as lubrication. They have experimentally shown that droplet moving in lubricated surfaces follows the Landau-Levich-Derjaguin law [61]. Depending on the solid surface energy, densities of liquid and lubrication liquid there can be several wetting configurations. Smith et al [28] derived theoretically several thermodynamically stable wetting configurations. Each wetting

configuration has different liquid three phase contact line [28]. An oil coated droplets presents the condition of droplet sliding under oil coated surfaces and also their shape mimics the shape of a cell there by enabling a path to study cellular behavior while in motion.

4.2 Theory

4.2.1 Droplet shedding

In general, forces involved in droplet shedding are adhesive force and drag force. They can be found using Equations (4.1)-(4.2) [28]

Adhesion force

$$F_{Ad} = l_c \gamma_{LV} (\cos\theta_R - \cos\theta_A) \tag{4.1}$$

where,

l_c - contact line

γ_{LV} - Surface tension of liquid

θ_R - Receding contact angle

θ_A - Advancing contact angle

Drag force

$$F_D = \frac{1}{2} . \rho_a . {v_{avg}}^2 . A_{ps} . C_D \tag{4.2}$$

where

ρ_a - Density of the air

v_{avg}- Air velocity

A_{ps} - Projected surface area facing air flow

C_D - Drag Coefficient

4.2.2 Oleoplaning of water droplet

There exist two interfaces in the case of oleoplaning of water droplet, as shown Figure 4.1. One, between oil and solid surface and the second interface is between water and silicone oil. While Equation (4.3) can be used to find adhesive force between Interfaces I, Equation (4.1)-(4.2)can be used to find adhesive force

between immiscible liquids, silicone oil and water. Adhesive force is defined as work of adhesion (W_{Ad}) given in the Equation (4.3)

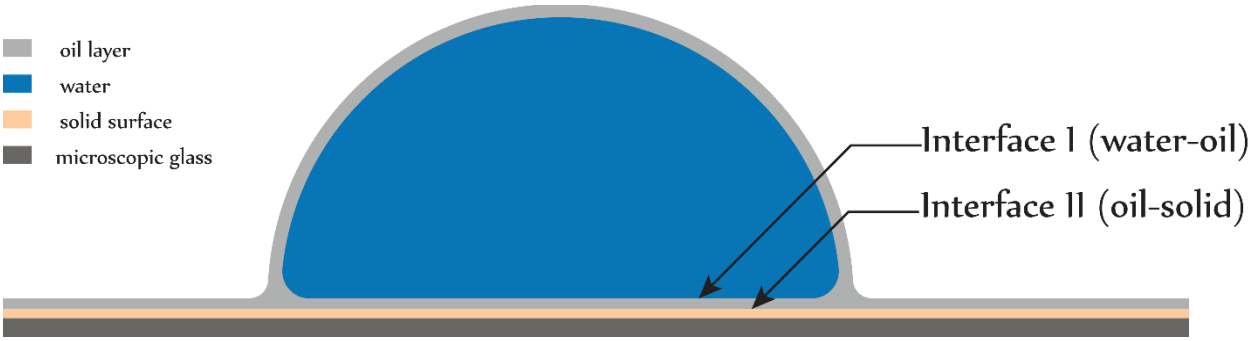

Figure 4.1: Water, oil and solid interfaces

$$W_{Ad} = \gamma_w + \gamma_{Oil} - \gamma_{int} \quad (4.3)$$

4.3 Experimental Setup

Experiments on oil coated water droplets to study average shedding velocity were performed in a mini wind tunnel. Oil coated water droplets were placed on test surface. Two test surfaces were used for the study, Parafilm and Teflon. Test surfaces were prepared by attaching respective film on to a 15x18mm thin microscopic glass slide. Droplet sizes of 5 µl, 10 µl, 15 µl and 20µl were tested at fluid flow of 2m/s. Different concentrations of oil coated droplet samples were prepared by mixing water and silicon oil on different volume ratios. Oil concentrations of 10%,20% and 40% were prepared. A 10% v-v concentration was prepared by mixing 0.5ml oil and 4.5 ml water. Figure 4.2 shows the schematic of experimental setup. Mini wind tunnel was set to an average flow of 2 m/s inside the test section. Droplet shedding under fluid flow was recorded using a high-speed camera. Droplet was placed inside the test section. A time of 10s time was allowed to reach equilibrium between the interfaces. Flow was initiated by switching on DC power supply.

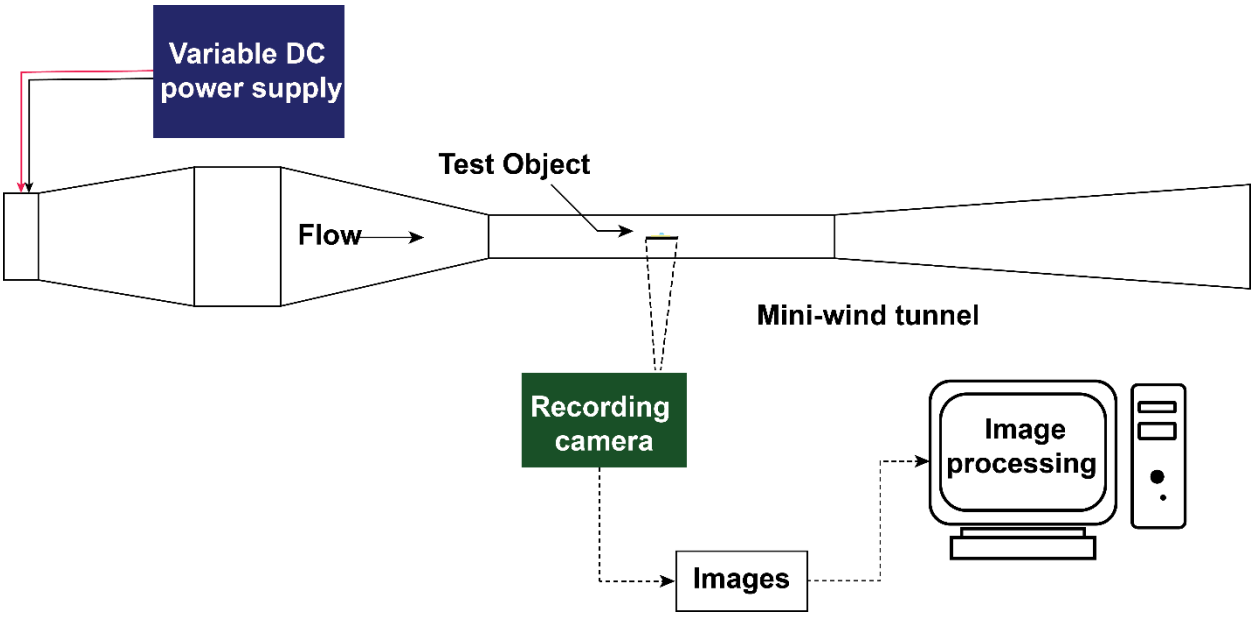

(a)

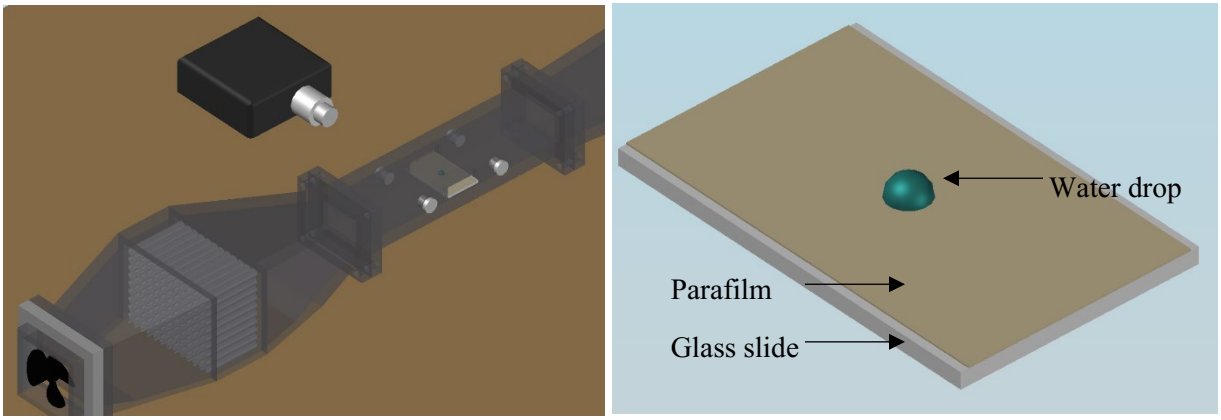

(b) (c)

Figure 4.2: (a) Schematic of experimental setup, (b) Experimental setup close up, (c) sample inside test section

Droplet shedding was recorded for 100s. Recorded video was used for image processing. In image processing initial frame at t= 0s and final frame at t=100s were taken. Changes in the positions of droplet were noted between the frames in pixels, as shown in Figure 4.3. This pixel difference was converted to actual distance by multiplying with a conversion factor. Distance travelled in 100 seconds was used to find average velocity. Using Equation (4.4)

$$v_{s,avg} = \left(\frac{(px_{x_2 y_1} - px_{x_1 y_1}) cf}{100} \right) \quad (4.4)$$

where,

$v_{s,avg}$ is average shedding velocity (mm/s),

$px_{x1, y1}$ - position of droplet at t=0, px

$px_{x2, y1}$ - final position of droplet t=100, px

cf - Conversion factor mm/px

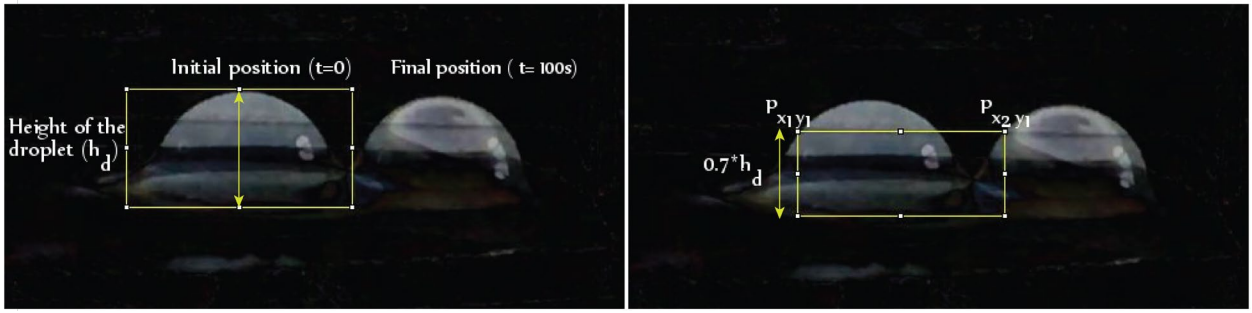

Figure 4.3: Experimental determination of average shedding velocity ($v_{s,avg}$) using image processing technique

4.4 Results and Discussion

Three parameters were studied in droplet shedding experiment. They are droplet volume (V_d), oil concentration (X_{oil}) and surface roughness.

4.4.1 Effect of droplet volume

Liquid drop on Parafilm and Teflon were tested for droplet shedding velocities. Bond number, which is the ratio of gravitational force to surface force, increases with droplet volume. Higher Bond number indicates that the influence of surface force over droplet is less. Hence larger droplets shed at higher average velocities. Figure 4.4 and Figure 4.5 show the effect of droplet volume over average shedding velocity. The error bars in the Figures cover the range of values obtained over three trials. 5µl has least $v_{s,avg}$ across all oil concertation and either test surfaces. Droplet with X_{oil} = 10% and V_d =5µl has $v_{s,avg}$ = 0.1778 mm/min on parafilm surface. $v_{s,avg}$ on parafilm increases with increase in volume. (As shown in Figure 4.4). For the given X_{oil} = 10%, $v_{s,avg}$ increases as 0.1178,0.2162,0.3097 and 0.475 mm/min for 5 µl, 10 µl,15 µl and 20 µl respectively. Similarly, $v_{s,avg}$ of droplet with higher oil concentration increases with volume as well. For

example, $v_{s,avg}$ of droplets with X_{oil} = 20%, increases as 0.2389,0.28875,0.5244 and 0.76 mm/min for 5 µl, 10 µl,15 µl and 20 µl, respectively.

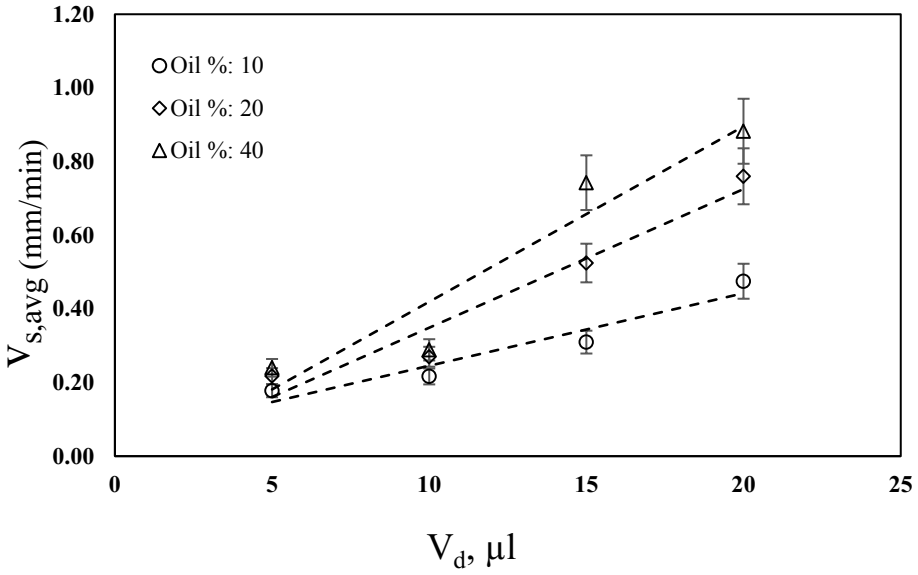

Figure 4.4: Effect of volume over average shedding velocity (Parafilm surface)

Droplets have higher $v_{s,avg}$ on Teflon surface. However, their $v_{s,avg}$ increases with V_d. Droplets of X_{oil} = 10% , has $v_{s,avg}$ of 0.43,0.95833, 1.1461 and 1.25 mm/min for 5 µl, 10 µl,15 µl and 20 µl, respectively. It can be understood from this study that larger droplets can be removed with less difficulty. Droplets of different sizes are analogous to cells of assorted sizes. As these cells shed at different $v_{s,avg}$, relative shedding velocity can be used to distinguish cells based on their sizes.

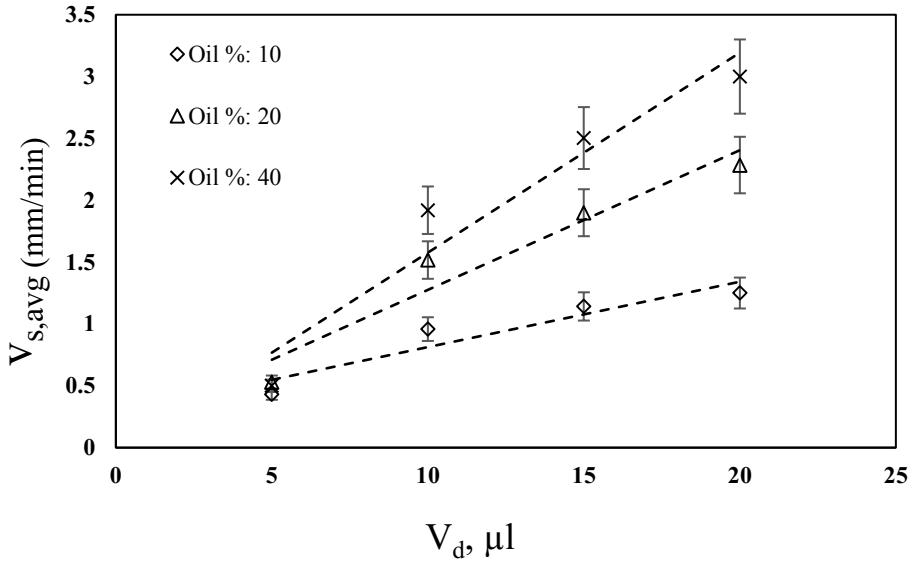

Figure 4.5: Effect of volume over average shedding velocity (Teflon surface)

4.4.2 Effect of oil concentration

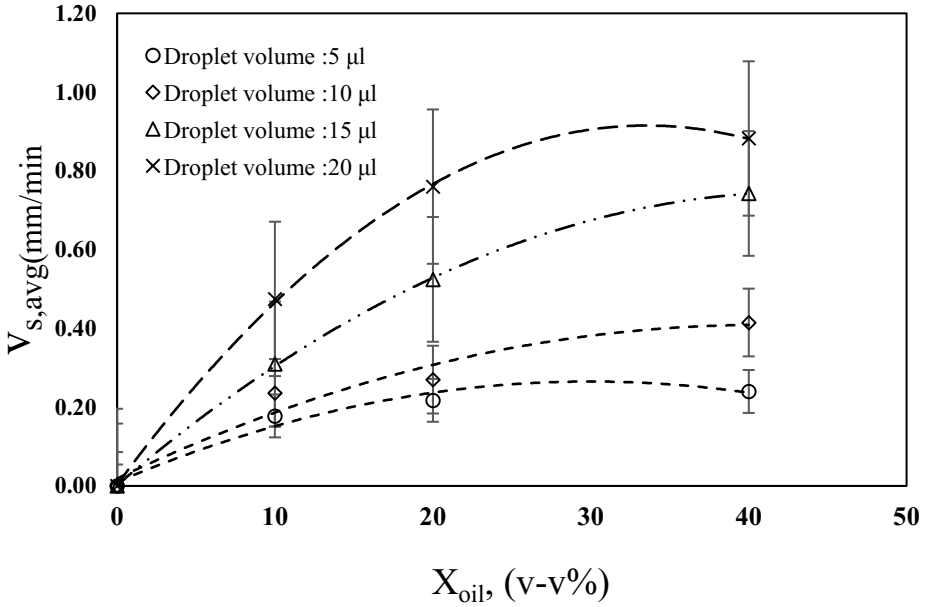

Figure 4.6: Effect of oil concentration over average shedding velocity (Parafilm surface)

Droplets are held on to surfaces with adhesive force. When oil coating is introduced, due to the properties of oil such as density, viscosity and surface tension, oil layer comes in between water and solid surface like a lubricant layer. This layer diminishes the influence of surface forces exhibited by solid surface as the

molecules from the solid surface are mostly engaged with oil molecules. Also, the adhesive force between oil and water is lower than that of solid and water. Thus droplet requires less drag force to dislodge, and droplet sheds at lower v_{avg}. Increasing oil coating will bring in more oil molecules to engage with the surface. Thus if the v_{avg} is held constant, droplets with higher oil concentration will not only dislodge but also dislodge at higher velocities ($v_{s,avg}$) . This hypothesis is experimentally confirmed when droplets of same V_d with higher oil concentration were subjected to v_{avg} = 2m/s. On parafilm surface, 5µl droplet with X_{oil} = 0% stays still while droplets of other oil concentration X_{oil} = 10% X_{oil} =20% X_{oil} = 40% sheds with $v_{s,\,avg}$ = 0.1777, 0.2173, 0.2399 mm/min, respectively. Shedding behavior of droplets is identical in Teflon surface as well.

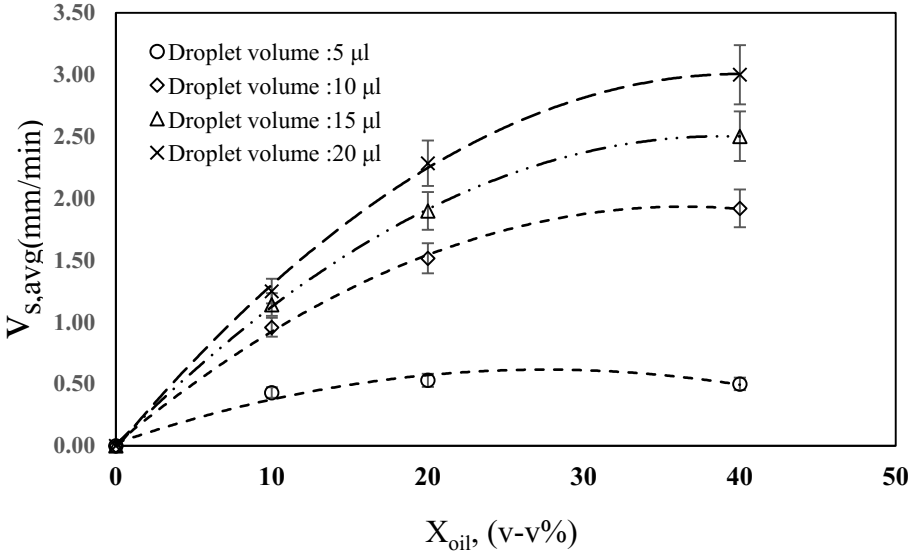

Figure 4.7: Effect of oil concentration over average shedding velocity over (Teflon surface)

As it can be observed from Figure 4.6 and Figure 4.7, $v_{s,\,avg}$ reaches saturation, indicated by almost flat curve between points X_{oil} = 20% and 40%, with increase in oil concentration. Although the $v_{s,avg}$ is higher for X_{oil} = 40% than that of X_{oil} = 20%, the slope indicates that droplet shedding velocity reached saturation. There is no strong increase in $v_{s,avg}$ between X_{oil} = 20% from X_{oil} = 40% . Point of saturation happens relatively at lower oil concentration for smaller droplets, because excess oil hinders the droplet shedding process due to the formation of wetting ridge [62]. Slipping nature can be perfectly exhibited when droplets

are still under surface forces. Once they are completely out of surface forces water droplets tend to spread on oil, evident from contact angle studies, shown in Figure 4.8 and Figure 4.9, thus decreasing the $v_{s,\,avg.}$

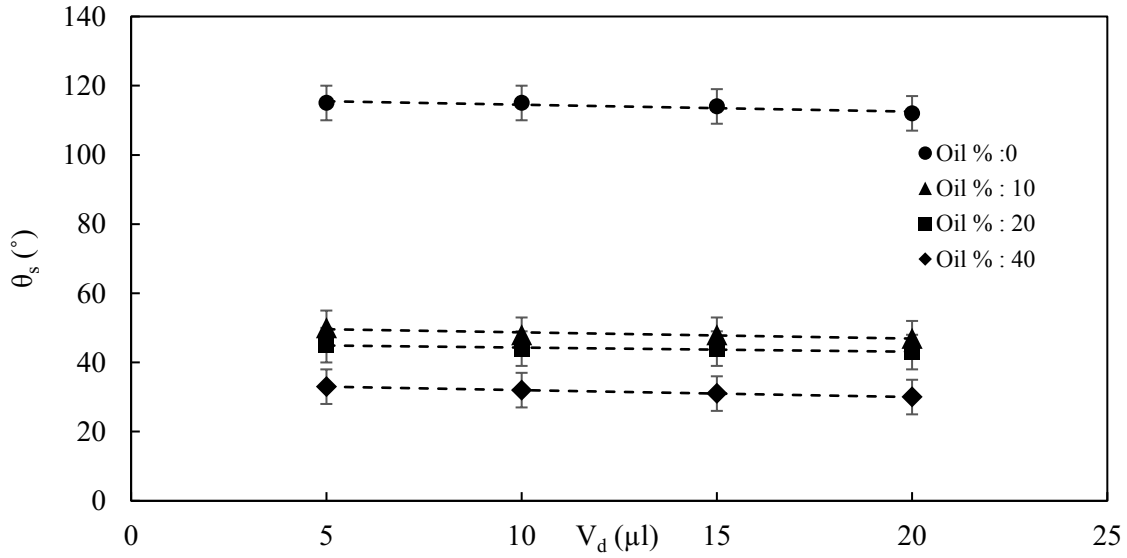

Figure 4.8: Static contact angle over parafilm surface

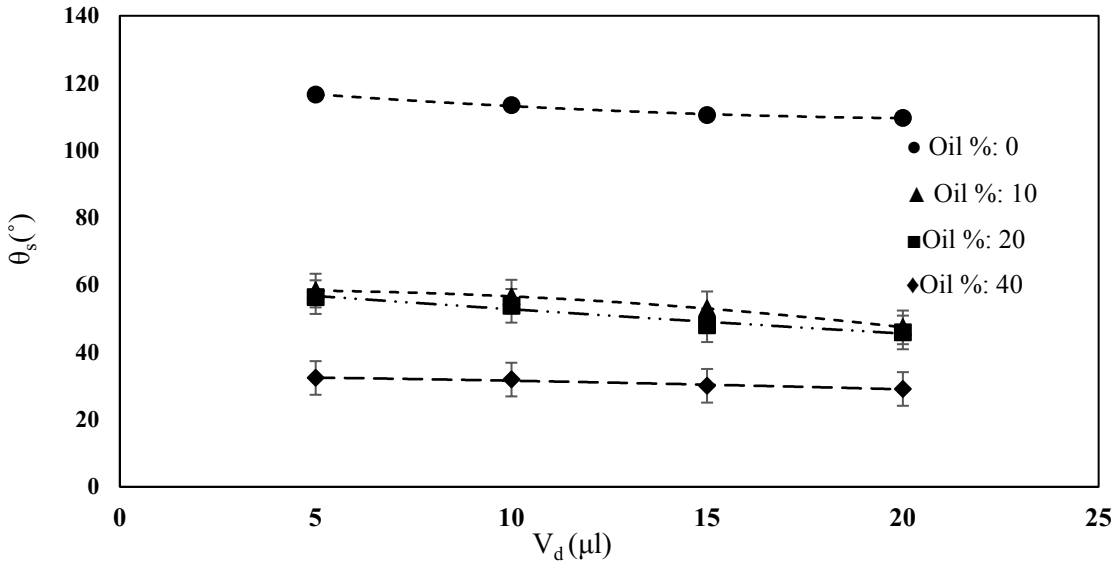

Figure 4.9: Static contact angle over Teflon surface

Shedding occurs as a result of rearrangement of contact line of the droplet to fall under equilibrium condition $\theta_{min} \leq \theta \leq \theta_{min}$, more precisely $\theta_{min} \leq \theta_R$ and $\theta_{max} \geq \theta_A$. Due to the application of drag force this condition is violated, with $\theta_A > \theta_{max}$ and $\theta_R < \theta_{min}$. Droplet will slip until it follows equilibrium condition. Factors that influence $v_{s,avg}$, in addition to surface roughness, are surface tension, viscosity and difference

in θ .Their relation with $v_{s,avg}$ can be grouped as shown in Equation (4.5). Surface tension is directly proportional to $v_{s,avg}$, because it is the force with which the molecules rearrange and it is a reactive force. It decides how quickly the droplet re -arranges. The arrangement of molecules should overcome viscous force, due to the slipping of fluid layer during the course of rearrangement, which acts in the opposite direction of droplet shedding. Thus, viscosity (μ) is inversely proportional to $v_{s,avg}$. $\Delta\theta$ factor which measures of how much the droplet has violated the equilibrium condition in terms of contact angle (θ_{min} - θ_R and θ_A -θ_{max}). Δθ decides the distance travelled for rearrangement. Higher $\Delta\theta$ would induce droplet to travel longer distance for rearrangement while smaller $\Delta\theta$ would result in shorter distance. Droplet cannot travel longer distance for a given F_D, because with time droplet volume will reduce gradually due to evaporation. As volume decreases higher F_D is required to shed the droplet further. Since, decrease in droplet volume due to evaporation favor adhesive force to strengthen its influence over droplet and making it stop. Droplet experiencing higher F_D will have higher $\Delta\theta$ thereby making it to travel longer distance which results in higher *average* shedding velocity (Note that $v_{s,avg}$ is measured as distance travelled in 100s) . Hence it is expected that liquid with higher surface tension, say Mercury, tend to rearrange quickly which will result in a higher $v_{s,avg}$. Silicone oil not only has lower surface tension but also higher viscosity, making it the slowest to move. Role of silicone oil in this experiment is to reduce the friction between surface and water, thereby making oil coated water droplet easy to slip. Post optimum concentration the wetting ridge formation acts as brakes for water droplets to move.

$$v_{s,avg} \propto \frac{\gamma_{LV}\Delta\theta}{\mu} \tag{4.5}$$

Deceased cells undergo structural changes during the stages of disease. Complex bio-chemical reactions, fungal growth in cell etc. changes the transport properties of the cell. Thus, relative shedding velocity can be used to distinguish cells based on their transport properties.

4.4.3 Effect of surface roughness

Out of two test surfaces used for the current study Teflon is smoother than parafilm. Hence the average shedding velocity is higher in Teflon. However, $v_{s,avg}$ of droplets reaches saturation relatively at lower oil

concentration on Teflon surface, because water droplets come out of influence of surface force at low oil concentration. Surface roughness of tissues, on which cells travel, do vary. Thus study helps in understanding the fact that although cells slip easily on smoother surfaces excess lubrication will hinder the movement of cells.

4.5 Conclusions

Experimental study of droplet shedding and oleoplaning was carried out to find average shedding velocity. It was found that lubrication that is provided in the form of silicone oil has profound influence over average shedding velocity. At low concentration, oil layer helps the droplet to overcome from adhesive force at lower drag force. However, post optimum concentration, oil layer retards the droplet slipping and reduces the droplet shedding velocity. This behavior will also depend on transport property of the oil used. Other than oil concentration, size of the droplet also has effect over droplet shedding velocity. It was found that volume is directly proportional to droplet shedding velocity. Among the two-solid surfaces that were tested (Parafilm and Teflon) it was found that droplet translates faster in Teflon surfaces as compared to Parafilm, since Teflon is smoother. Both the solid surfaces that are tested, are hydrophobic and gives consistent shape to the Sissle droplet.

Chapter 5| Fluid load augmented micro balance

Abstract

Micro- cantilever based micro weighing balance was studied using polydimethylsiloxane (PDMS) micro-cantilever beam and water droplet. In this system, micro-cantilever beam acts as spring balance while the droplet acts as weight. Initially, tip defection of cantilever beam under the body load provided by water droplets of sizes 4, 5, 6 and 7 µl were found experimentally. For this study, droplets were placed at dimensionless length ξ =0.8 from the clamped end. Fluid load augmentation was studied by studying the tip deflection of the beam with droplet under flow velocities between 0.75 m/s-1.5m/s. A mini wind tunnel is used to provide fluid load with air flow occurring along the length of the beam. Experimental results show an increase in tip deflection with flow velocity, suggesting the phenomena of fluid load augmentation. In addition to experimental results, this chapter also presents modelling of natural frequency of the micro-cantilever beam with added mass using Rayleigh's energy method.

5.1 Introduction

Over the years, weighing balance has been adapted into several designs and modifications yielding reasonably good improvements in performance. For measuring lighter objects, a micro weighing scale can be suitably used. However, measuring extremely lighter samples in µg ranges, becomes difficult with conventional method of spring based weighing balance as they reach limitations in precision. Thus a micro-cantilever based weighing balance for detecting slight mass changes is studied and their details are explained. The sensitivity of the spring governs the range of a weighing balance. It is comparable to sensitivity of the beam in a cantilever based weighing balance. The sensitivity of the beam can be increased by increasing the deflection of the beam for a given load. Several methods have been proposed to enhance the deflection of the beam such as changing the dimensions, changing shape of the beam [63] [64] [65]. A.-R.A. Khaled et al [64] studied advantages of modified beams in epsilon shape. They have studied the deflection of micro-cantilever beam under fluid flow. Turbulence in the flow creates disturbances in the beam. The epsilon beam possesses large effective stiffness making the beam stable under flow turbulence.

Large deflection was observed in the center beam in epsilon beam assembly. In addition A.-R.A. Khaled et al [65] performed analytical and numerical studies to find the deflection of cantilever beams. Three types of the beam were considered for the study, namely, regular rectangular beam, modified triangular beam and epsilon beam. These beams were subjected to different types of concentrated force, concentrated moment and constant surface stress. It was reported that the deflection values of modified triangular beam and the epsilon beam are 280% above than deflection values of a regular rectangular beam under concentrated moment and 425% above the beam deflection values of regular rectangular beam for surface stress load. The deflection at the free end of the intermediate epsilon beam is 200% above the deflection values of modified triangular beam. G. Zhang et al [66] studied analytically the deflection and resonant frequency of 12 geometrically distinct micro-cantilever beams. These geometry modifications were carried out to study the effect of mass near the free end and the effect of clamping width at the fixed end. It can be concluded from this study that minimizing effective mass near the free end and reducing the clamp width at fixed will increase the micro cantilever sensitivity. Deflection of geometrically modified beam can go up to 343%.

It is interesting to study the deflection of the beam when it is under more than one type of load. A combination of load where point load and fluid load are acting simultaneously, higher tip deflection would be observed. Since the beam is already under point load, additional fluid load excites the beam resulting a forced vibration. For a given fluid load, deflection due to forced vibration will depend on point load. Thus, mass changes can be transduced into mechanical signal in the form of tip deflection. The suggested mode of deflection enhancement is shown in Figure 5.1 .

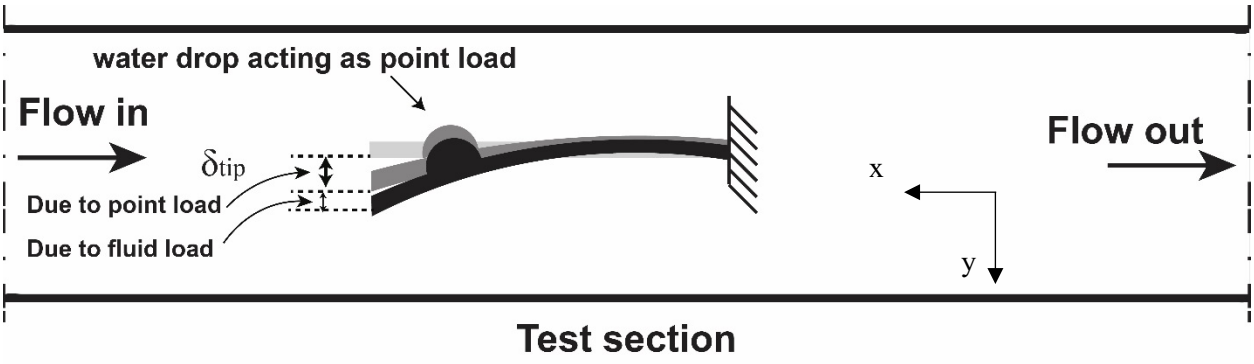

Figure 5.1: Fluid load augmentation of microcantilever beam

5.2 Theory

Static deflection of the cantilever beam is given in Equation (5.1)

$$\delta_{tip}=\frac{m_d\, g\, a^2}{6EIyy}(3l_b-a) \tag{5.1}$$

where,

δ_{tip} -Tip deflection

m_d - Mass of water droplet

g - Acceleration due to gravity

l_b - Length of the beam

E -Young's modulus

Iyy-Moment of inertia about the neutral axis

a- Position of water droplet from the fixed end

When the point load acts at the free end ($a=l_b$) δ_{tip} will be maximum. Substituting $a=l_b$ in Equation (5.1) results Equation (5.2)

$$\delta_{tip}=\frac{m_d g\, l_b^3}{3EIyy} \tag{5.2}$$

Fluid flow is along the length of the micro-cantilever. Hence micro-cantilever acts as an airfoil. It will experience lift and drag forces from fluid flow. Lift force will act on micro-cantilever making it to bend further along y-direction.

Lift provided by fluid load is given by Equation (5.3)

$$L=\frac{1}{2}\rho_a v^2 A_{sf} C_L \tag{5.3}$$

where

L - Lift

ρ_a- Density of the air

v_a - Velocity of the air

A_{sf} - Surface area of the beam

C_L - Lift coefficient

Overall bending due to Point load and fluid is given by

$$\delta_{overall}=\delta_{tip}\pm\text{Deflection due to L} \tag{5.4}$$

Fluid load is provided using a fan. The natural frequency of the beam and blade pass frequency of the fan under the given flow condition are discussed below.

5.3 Modeling of natural frequency (ω_n) of the micro-cantilever beam carrying point mass using Rayleigh's method

Rayleigh's method is based on the principle of conservation of energy. The energy in a dynamic system consists of the kinetic energy (T) and the potential energy (U). Total energy of the system is constant.

$$T + U = \text{Constant} \tag{5.5}$$

The kinetic energy is stored in the mass and is proportional to the square of the velocity. The potential energy includes strain energy which is proportional to elastic deformations and the work done by the applied forces. The total energy will always remain constant. When the micro-cantilever beam is undergoing

vibrations there is conversion of one type of energy to other. When the beam reaches any of the two extreme positions the velocity is zero and all the kinetic energy is converted in to potential energy. Because the kinetic energy is zero, potential energy is maximum in this case. When the beam is at neutral axis potential energy is zero and kinetic energy is maximum, thus we can write, $T_{max} = U_{max}$

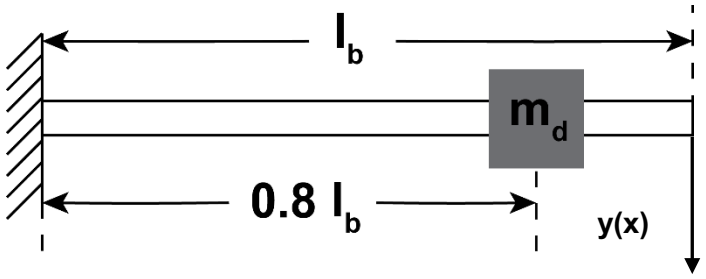

Figure 5.2: Cantilever beam under point load

Assuming deflection shape function as $y(x) = x^2$ [67]

$$U_{max} = \frac{1}{2} EIxx \int_0^{l_b} (y'')^2 \, dx \tag{5.6}$$

$$T_{max} = \frac{1}{2} m_b {\omega_n}^2 \int_0^{l_b} y^2 \, dx + \frac{1}{2} m_d {\omega_n}^2 y^2 \tag{5.7}$$

$${\omega_n}^2 = \frac{U_{max}}{T^*_{max}} \tag{5.8}$$

here, m_b is mass of the beam per unit length, m_d mass of the droplet and $T_{max} = \omega_n^2 T^*_{max}$. First and second derivative of y(x) with respect to x is written as y' and y'' respectively. $y` = 2x$, $y'' = 2$

Considering a term ξ, dimensionless length, defined as $\xi = \frac{x}{l_b}$

Now, $dx = d\xi \, .l_b$

when $x = 0$, $\xi = 0$

$x = l_b$, $\xi = 1$, changing the limits and dx in Equation (5.6) and (5.7)

$$U_{max} = \left(\frac{1}{2}\right) EIxx \int_0^1 4 \, (d\xi . l_b)$$

$$U_{max} = \left(\frac{1}{2}\right) 4 . E . Ixx . l_b$$

$$T^*_{max} = \left(\frac{1}{2}\right) m_b \int_0^1 ((\xi l_b)^2)^2 \ (d\xi . l_b) + \frac{1}{2} m_d y^2$$

$$T^*_{max} = \left(\frac{1}{2}\right) m_b \ l_b \int_0^1 \xi^4 (l_b)^4 \ d\xi + \frac{1}{2} m_d x^4$$

$$T^*_{max} = \left(\frac{1}{2}\right) m_b (l_b)^5 \frac{1^5}{5} + \frac{1}{2} m_d (\xi l_b)^4$$

Substituting U_{max} and T^*_{max} in Equation (5.8)

$$\omega_n{}^2 = \frac{\left(\frac{1}{2}\right) 4.E.Ixx.l_b}{\left(\frac{1}{2}\right) m_b (l_b)^5 \frac{1^5}{5} + \frac{1}{2} m_d (\xi l_b)^4}$$

$$\omega_n{}^2 = \frac{4.E.Ixx}{\frac{m_b (l_b)^4}{5} + m_d \xi^4 (l_b)^3}$$

$$\omega_n = 4.4721 \sqrt{\frac{EIxx}{m_b (l_b)^4 + 5\xi^4 m_d (l_b)^3}} \qquad (5.9)$$

Table 5.1: Properties of the microcantilever beam and droplet

Properties	**Values**
Beam length (l_b)	7 x10^{-03} m
Beam width (w_b)	3 x10^{-03} m
Beam thickness (t_b)	240 x10^{-06} m
Moment of inertia (I)	3.46x10^{-15} m^4
Beam mass per length (m_b)	6.95x 10^{-04} kg
Young's modulus of PDMS,(E)	802000 Pa
Density of water (ρ_w)	1000 kg/m^3

Table 5.2: Natural frequency of the beam with point load

Droplet volume (V_d) $m^3 x\ 10^9$	Mass of the droplet(m_d) kg $x10^6$	ω_n in Hz
4	4	111.32
5	5	103.50
6	6	97.13
7	7	91.80

5.3.1 Blade pass frequency (BPF)

Blade pass frequency is the rate at which the blades pass by a fixed point. The blades present in the fan produce periodic vibration at frequencies that depend on the speed of rotation, number of blades, and mechanical structure of the system. [68] The BPF of the fan present in the mini windtunnel was found for the vavg 0.75 m/s, 1.00 m/s, 1.25 m/s, 1.50 m/s. Equation (5.10) was used to find BPF of the fan

$$BPF = \frac{B \times RPM}{60} \tag{5.10}$$

where

BPF - Blade pass frequency

RPM- Angular velocity of the fan

B- Total number of blades in the fan = 5

Table 5.3: Blade pass frequency of the fan

V_{avg}(m/s)	RPM	BPF(Hz)
0.75	2610	218
1.00	3434	286
1.25	4120	343
1.50	4922	410

5.4 Experimental set up

The setup consists of a PDMS microcantilever beam attached to a glass slide, a mini wind tunnel, a variable DC power supply and a recording camera. The micro-cantilever used for the experiment was fabricated using spin coating technique.

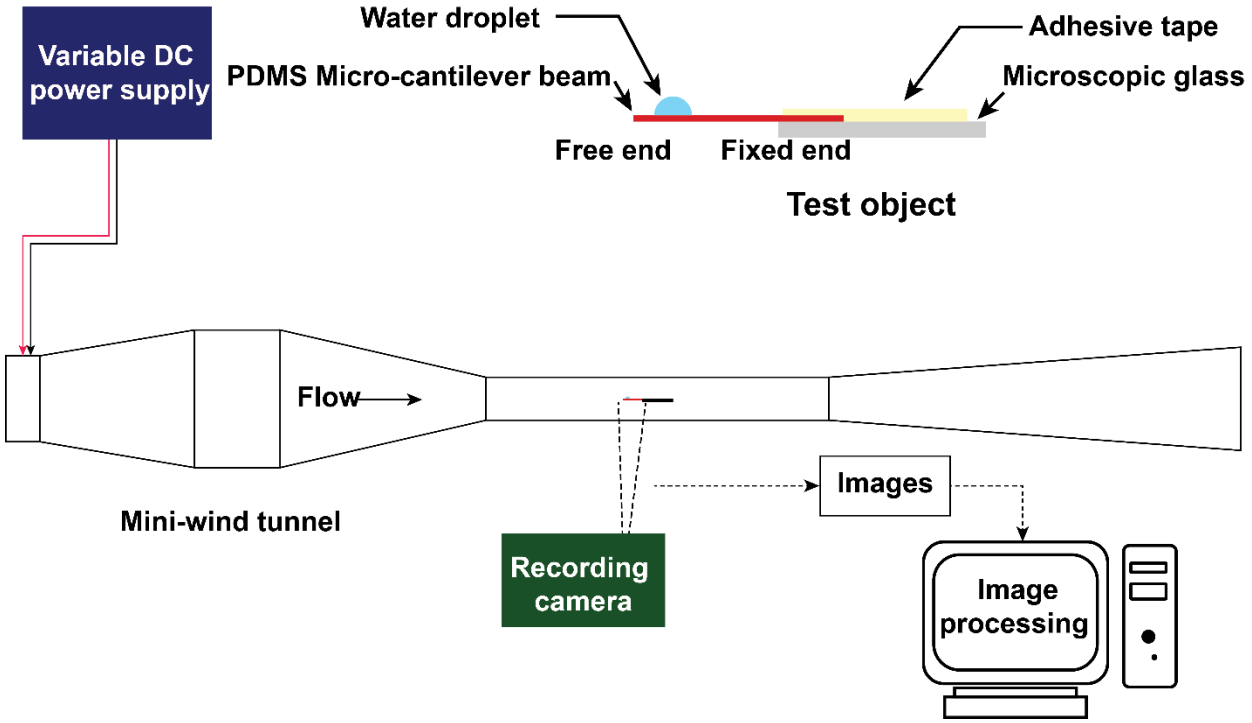

Figure 5.3: Schematic of experimental setup

Dimension of the micro-cantilever used in the experiment is 3x7x0.24 mm. The thin beam is attached to a 10x20x1 mm microscopic glass slide, which acts as base, using an adhesive tape. Micro-cantilever was placed inside the test section of the mini wind tunnel. Water droplet of measured volume was placed over the beam using a micro pipette. The position ξ=0.8 was lightly marked using a marker on transparent PDMS beam. This step was carried to ensure that the droplet is placed at the same position each time. The PDMS beam with droplet attached to glass slide is called test object. Deflection experiment was carried out by initiating the flow. Fluid flow provided by micro fan becomes laminar inside the test section. The micro fan was calibrated with respect to DC voltage to provide specific flow velocity. The cantilever deflection was

captured using a recording camera, as shown in Figure 5.3. The recordings of the experiment were used to extract results.

The experiment consists of two steps. Initially the tip deflections of the microcantilever beam were found for different droplet volumes. For this experiment micro fan was turned off. Images of the beam were taken with and without droplet load. From these images the static tip deflection values were determined by considering the pixel values at the beam tip. As shown in Figure 5.4. Micro fan was switched on to test the tip deflection of the beam under fluid load. Fan has a transient time of 100s. Hence, the fan was switched on and kept running for 100s before placing the test object inside the test section. After 100s of switching the fan on, test object kept inside the test section and fluid structure interaction was captured for 20s. This step was followed to minimize the effect of droplet evaporation over tip deflection. The presented results are average of four trials. Error bars in the results show the range of values obtained over the trials.

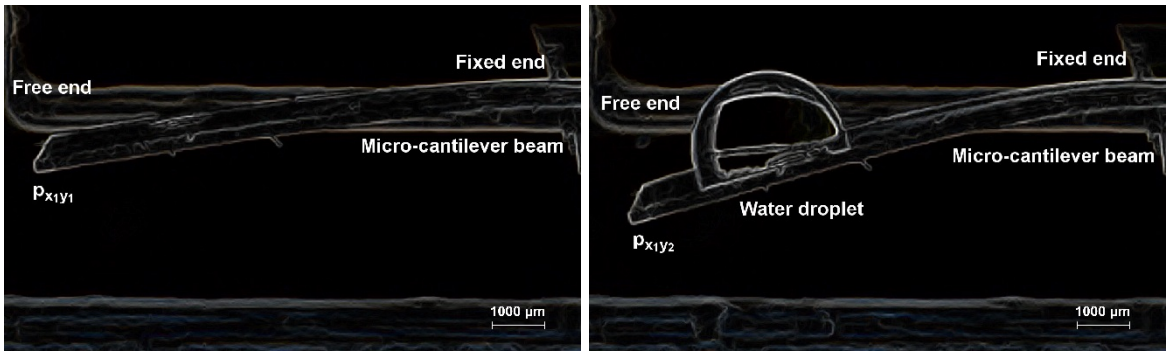

(a) (b)

Figure 5.4: Estimation of tip deflection of micro-cantilever beam under static condition using image processing technique (a) Before point load (b) Under point load

5.5 Results and Discussion

Point load (P) provided by droplet was found from the mass of the droplet (m_d). Experimental values of static deflection of micro cantilever beam under the point load was found and presented in Figure 5.5. 4 µl droplets provides point load of 39.24 µN. Experimental tip deflection for this load was found to be 920 µm, while analytical tip deflection value, found using Equation (5.1) was 920µm. Tip deflection of the beam

increases with increase in droplet size. Tip deflection of beam for droplet size 5 µl, 6 µl and 7 µl were found to be 1323 µm, 1596 µm and 1916 µm, respectively. As shown in Figure 5.5. Measured tip deflection value lies under analytical values found with $\xi = 0.8$ and $\xi = 0.6$.The marginal deviation of experimental results to analytical values are because the Equation (5.1) considers load to be point load while in reality the droplet provides distributed load. Experimental ξ values for the corresponding droplet sizes were found and presented in Table 5.4.

Table 5.4: Experimental ξ values

Droplet volume (µl)	$\xi_{\text{Experimental}}$
4	0.72
5	0.74
6	0.73
7	0.73

Tip deflection of micro cantilever under fluid load were found. Fluid loading increases the tip deflection. As it can be observed from Figure 5.6 with increase in fluid load, tip deflection (δ_{tip}) of the beam increases. For a point load of 39.24µN, δt_{ip} increase from 920 µm for $v_{avg} = 0$ m/s , to 936, 950, 966 and 996 µm, respectively for v_{avg} of 0.75 m/s, 1.00 m/s,1.25 m/s and 1.5 m/s. This observation is consistent with other droplet sizes. Maximum value of δ_{tip} is observed for v_{avg} of 1.5 m/s. The maximum value were 996, 1467, 1731, 2051µm, respectively for point load of 39.24, 49.05, 58.86, 68.67 µN.

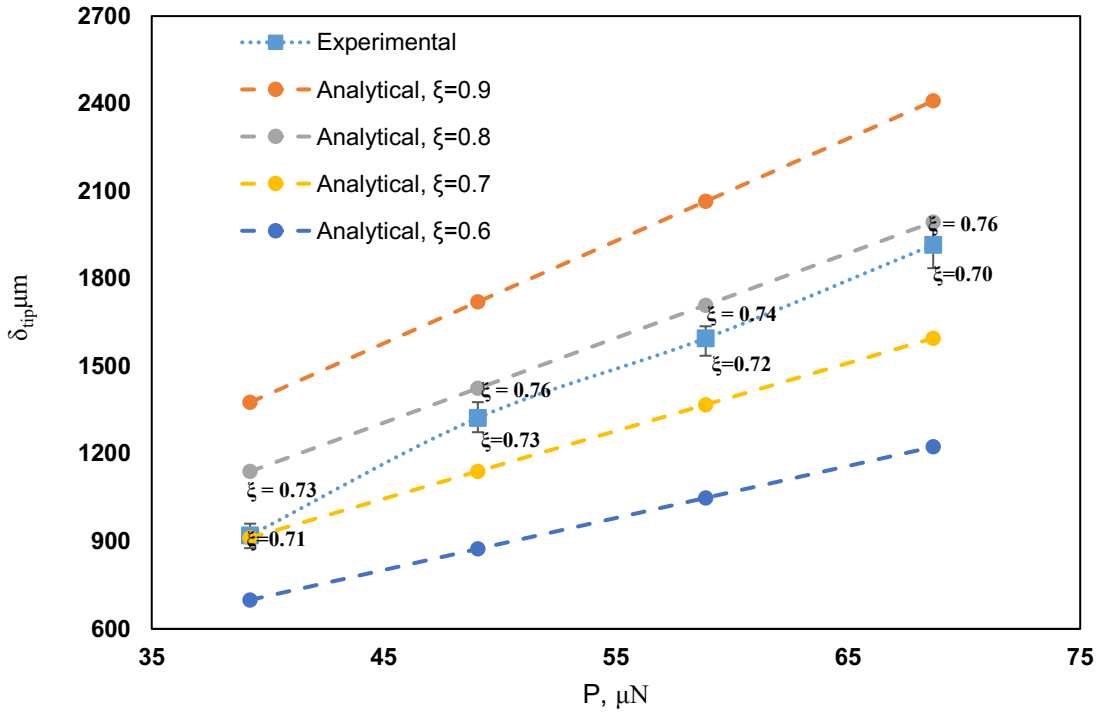

Figure 5.5: Static deflection of microcantilever beam under point load

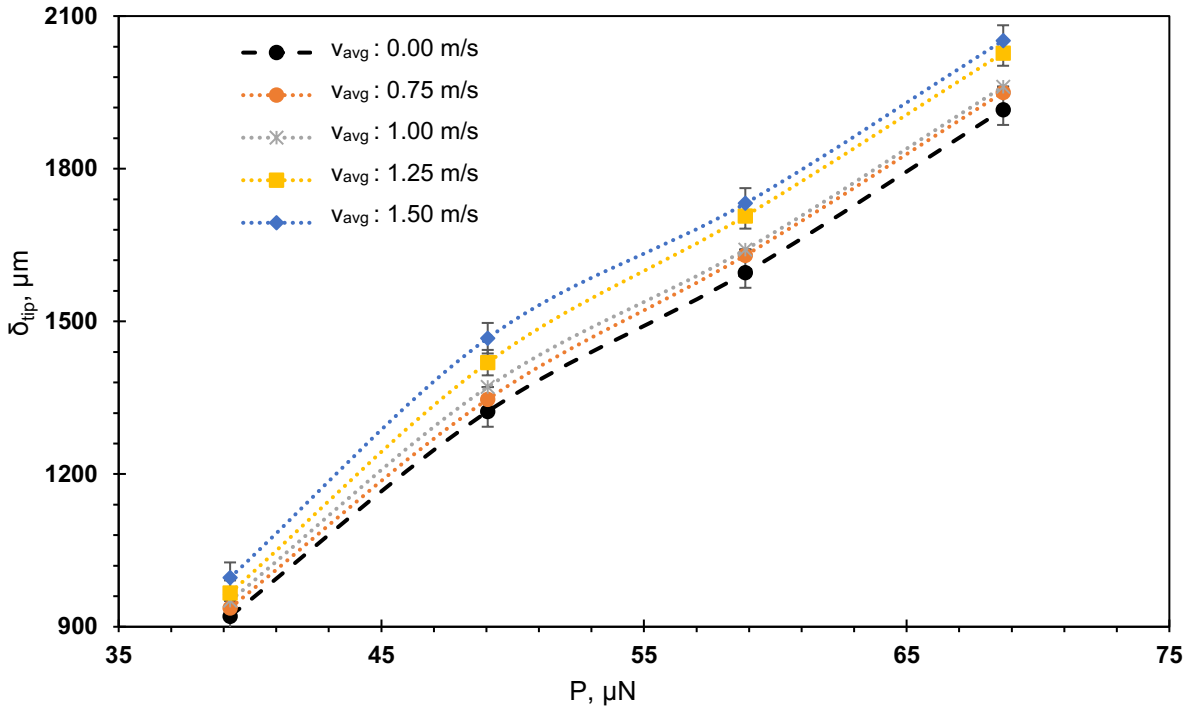

Figure 5.6: Tip deflection of cantilever beam under fluid load

5.6 Conclusions

Tip deflection of micro-cantilever under simultaneous point load and fluid load was studied using a mini wind tunnel. Fluid load is provided by the fan attached in wind tunnel. Equation to find natural frequency of the cantilever beam with point load was modelled using Rayleigh's energy method. Blade pass frequency of the fan was found to ensure the microcantilever beam is not operating at resonant frequency. Experimental results suggest that tip deflection of the micro cantilever beam is enhanced under fluid load thus, suggesting the phenomena of deflection augmentation in the presence of flow. This simple model provides a method to develop micro cantilever based micro balance to detect slight mass changes.

Chapter 6| Conclusions and suggestions for future work

6.1 Summary and Conclusions

The aim of this work is to study fluid interaction with microstructures in microfluidic environment using oil coated droplets and to analyze the cellular behavior under drag force. This work is mainly experimental. A low speed mini wind tunnel was designed, built and tested to perform fluid interaction studies involving microstructures. The microstructures used in the study are oil coated water droplets, of 4µl to 20µl, and Polydimethylsiloxane (PDMS) micro cantilevers. Experimental set up consists of a mini wind tunnel powered using a variable DC power supply, test objects (microstructures) and a recording camera. The fluid interaction of micro structures is recorded using a recording camera and experimental results are obtained using an image processing technique.

Initially, design of mini wind tunnel was validated by performing deflection experiments on micro cantilever beams. PDMS micro-cantilevers of sizes 3- 5mm in width, 8-12mm in length and 0.160-0.24mm in thickness were tested under fluid flow. Micro cantilevers were inserted inside the test section so that the flow occurs perpendicular to the beam. Micro cantilever beams were tested between the flowrates 160-360ml/s. Fluid interaction of micro-cantilever beams were recorded using a camera attached to an optical microscope. The recordings from the camera were used to extract tip deflection of the cantilever beam. A MATLAB based pattern matching method was adopted to find experiential deflection values.

Secondly, droplet deformation experiment, which involves testing of deformation oil-coated water droplets under fluid flow was carried. Droplets of volume 5-20µl were tested in this experiment. Measured volume of droplet was placed over a test surface. Test surface is prepared by attaching parafilm over a 10x20x1 mm microscopic glass slide. Test surface with droplet was kept inside the mini wind tunnel and deformation of droplets were tested for the flow rates 0.75 m/s – 1.5 m/s. Fluid interaction of microstructure was recorded using a recording camera. From the recordings deformation of the droplets were found using image processing technique.

Third experiment is about finding the average shedding velocity of the oil coated water droplets over two different test surfaces, namely, Teflon and Parafilm. Test surface were prepared by attaching respective film to 10x20x1 mm microscopic glass slides. Droplet was placed over the test surface and shedding velocity of the droplets were found for the air velocity of 2 m/s. The droplet motion is recoded for 100s and average shedding velocity were found using image processing technique which involves finding the droplet position in pixels at t=0 and the same at t=100s. Converting the difference in pixel value to actual length gives the distance travelled by the droplet in 100s.

Fourth experiment is a novel method of developing a flow augmented cantilever based weighing balance. In this experiment tip deflection of the PDMS cantilever beam is enhanced using two loads that are acting simultaneously. For this experiment a 240μm thick PDMS cantilevers were fabricated and attached to a 3x20x1mm microscopic glass slide to form a cantilever beam. The final dimensions of micro-cantilever beam are 3x7x0.240 mm. Micro-cantilever beam was kept inside mini-windtunnel so that flow occurs along the length of the beam. Droplets of 4-7μl were used to provide point load to the beam. Micro-cantilever beam was subjected to point load with load acting at ξ =0.8. Additionally a fluid velocity of 0.75m/s to 1.5 m/s was provided to deflect the beam further. The cantilever deflection was captured using a recording camera and experimental deflection was found using the recordings.

The essence of findings in this work is summarized below

- Tip deflection of the cantilever beam is function of beam stiffness. In addition to material properties, geometry of the cantilever beam has importance in determining tip deflection. Beam length favors tip deflection and the effect of beam length over tip deflection is significant. Beam thickness and width also govern tip deflection. Although both these dimensions are inversely proportional to tip deflection beam thickness is the prevailing factor which determines the tip deflection. This significance is due to the fact that the beam stiffness equation has beam thickness as a cubic term.
- Deformation of oil-coated droplets is function of drag force, droplet volume and oil concentration. It is observed that bigger droplets deform more. Since smaller droplets are under the influence of

surface force and they deform less. Also oil concentration contributes to the droplet deformation. Oil layer covers the droplets from all sides. Hence the drag force is not completely transferred to the water droplet within. Water droplet experiences less force and thus less deformation is observed.

- Average shedding velocity of oil coated water droplet is function of surface roughness, droplet volume and oil concentration. Even though, oil layer assists the water drop to slip easily over solid surface, excess amount of oil hinders the droplet shedding process. The average shedding velocity of oil coated water droplet is higher in smoother surface such as Teflon as compared to relatively rough surface parafilm. Bigger droplets are easy to dislodge as they are under less influence of surface forces. In addition, bigger droplets provide greater surface area for the drag force to act. Hence larger droplets have higher average shedding velocity.
- When cantilever beam with point load is under an additional fluid load, a phenomena involving flow augmentation occurs. Where, tip deflection of the cantilever beam increases with fluid loading.

6.2 Scope for Research and Future Work

The present thesis serves as a starting point to study fluid interaction of microstructure under micro fluidic environment using a mini windtunnel. Several other fluid microstructure interaction studies can be conducted using presented experimental setup. A list of proposed future work is suggested below

- *Droplet mixing and Nano reactor:* Laminar flow provided in the test section enables us to study several experiments which requires low fluid flow. Droplet mixing, where time required for complete mixing of two droplets of known size can be studied.
- *Slotted micro-cantilever deflection studies;* Tip deflection of the micro cantilever depends on applied point load. Weight of the cell changes based on the health of the cell. Hence a cantilever based sorting method can be developed to distinguish healthy and dead cells.

- *Theoretical modeling of deformation of oil coated water droplets.* Findings from present research are based on experimental work. Using theoretical modelling one can study the effect of individual parameters such as drag force, droplet volume, oil concentration , surface properties etc in greater detail
- *Theoretical modelling of shedding of oil coated water droplets;* in the current study average shedding velocity of oil coated water droplets were studied and the effect of surface roughness, droplet volume and oil concentration were studied experimentally. A theoretical modelling of the same would be helpful in understanding the effect of the same in greater detail.

REFERENCES

[1] R. D. Kamm, J. Lammerding and M. R. K. Mofrad, "Cellular Nanomechanics," in *Springer Handbook of Nanotechnology*, B. Bhushan, Ed., Berlin, Heidelberg, Springer Berlin Heidelberg, 2010, pp. 1069-1100.

[2] E. Moeendarbary and A. R. Harris, "Cell mechanics: Principles, practices, and prospects," *Wiley Interdisciplinary Reviews: Systems Biology and Medicine,* pp. 371-388, 2014.

[3] P. A. Janmey and C. A. McCulloch, "Cell Mechanics: Integrating Cell Responses to Mechanical Stimuli," *Annual Review of Biomedical Engineering,* pp. 1-34, 2007.

[4] J. Shemesh, I. Jalilian, A. Shi, G. Heng Yeoh, M. L. Knothe Tate and M. Ebrahimi Warkiani, "Flow-induced stress on adherent cells in microfluidic devices," *Lab Chip,* vol. 15, pp. 4114-4127, 2015.

[5] D. Brindley, K. Moorthy, J.-H. Lee, C. Mason, H.-W. Kim and I. Wall, "Bioprocess Forces and Their Impact on Cell Behavior: Implications for Bone Regeneration Therapy," *Journal of Tissue Engineering,* pp. 1-13, 2011.

[6] T. J. Vaughan, M. G. Haugh and L. M. McNamara, "A fluid-structure interaction model to characterize bone cell stimulation in parallel-plate flow chamber systems," *Journal of The Royal Society Interface,* 2013.

[7] W. Helfrich, "Elastic Properties of Lipid Bilayers Elastic Properties of Lipid Bilayers: Theory and Possible Experiments," *Z. Naturforsch,* vol. 28, no. 6, pp. 3-7, 1973.

[8] A. Janshoff and C. Steinem, "Mechanics of lipid bilayers: What do we learn from pore-spanning membranes?," *Biochimica et Biophysica Acta (BBA) - Molecular Cell Research,* vol. 1853, no. 11, pp. 2977-2983, 2015.

[9] H. J. Deuling and W. Helfrich, "The curvature elasticity of fluid membranes : A catalogue of vesicle shapes," *Journal de Physique,* vol. 37, no. 11, pp. 1335-1345, 1976.

[10] S. Suresh, "Mechanical response of human red blood cells in health and disease Some structure-property-function relationships," *Journal of Materials Research,* vol. 21, no. 8, pp. 1871-1877, 2006.

[11] M. Lekka, "Discrimination Between Normal and Cancerous Cells Using AFM," *BioNanoScience,* vol. 6, no. 1, pp. 65-80, 2016.

[12] M. Tartibi, Y. X. Liu, G. Y. Liu and K. Komvopoulos, "Single-cell mechanics - An experimental-computational method for quantifying the membrane-cytoskeleton elasticity of cells," *Acta Biomaterialia,* vol. 27, no. 1, pp. 224-235, 2015.

[13] S. P. Wankhede, Z. Du, J. M. Berg, M. W. Vaughn and Tim Dallas, "Cell Detachment Model for an Antibody-Based Microfluidic Cancer Screening," *Biotechnol. Prog,* vol. 22, pp. 1426-1433, 2006.

[14] X. Zeng and S. Li, "Multiscale modeling and simulation of soft adhesion and contact of stem cells," *Journal of the Mechanical Behavior of Biomedical Materials,* vol. 4, pp. 180-189, 2011.

[15] S. R. Hodges and O. E. Jensen, "Spreading and peeling dynamics in a model of cell adhesion," *Journal of Fluid Mechanics,* vol. 460, no. 1, pp. 381-409, 2002.

[16] Y. Yuan and T. R. Lee, Contact angle and wetting properties, Berlin, Heidelberg.: Springer, 2013, pp. 3-34.

[17] M. E. R. Shanahan, "The influence of solid micro-deformation on contact angle equilibrium," *Journal of Physics D: Applied Physics,* vol. 20, no. 7, pp. 945-950, 1987.

[18] G. C. Gainer, "Silicone Oils for Lubricating Steel Versus Steel," *Industrial & Engineering Chemistry,* vol. 46, no. 11, pp. 2355-2362, 1954.

[19] E. Kumbur, K. Sharp and M. Mench, "Liquid droplet behavior and instability in a polymer electrolyte fuel cell flow channel," *Journal of Power Sources,* vol. 161, no. 1, pp. 333-345, 2006.

[20] J.G.Cartona, V.Lawlor, A.G.Olabi, C.Hochenauer and G.Zauner, "Water droplet accumulation and motion in PEM (Proton Exchange Membrane) fuel cell mini-channels," *Energy,* vol. 39, no. 1, pp. 63-73, 2012.

[21] B. Mondal, K. Jiao and X. Li, "Three-dimensional simulation of water droplet movement in PEM fuel cell flow channels with hydrophilic surfaces," *Int. J. Energy Res.,* vol. 35, pp. 1200-1212, 2011.

[22] L. Gao and T. J. McCarthy, "Contact Angle Hysteresis Explained," *Langmuir,* vol. 22, no. 14, pp. 6234-6237, 2006.

[23] Y. S. Yu and Y. P. Zhao, "Elastic deformation of soft membrane with finite thickness induced by a sessile liquid droplet," *Journal of colloid and interface science,* vol. 339, no. 2, pp. 489-494, 2009.

[24] C. Antonini, F. J. Carmona, E. Pierce, M. Marengo and A. Amirfazli, "General Methodology for Evaluating the Adhesion Force of Drops and Bubbles on Solid Surfaces," *Langmuir,* vol. 25, no. 11, pp. 6143-6154, 2009.

[25] S. Moghtadernejad, M. Mohammadi, M. Jadidi, M. Tembely and A. Dolatabadi, "Shear Driven Droplet Shedding on Surfaces with Various Wettabilities," *SAE Int. J. Aerosp.,* vol. 6, no. 2, pp. 459-464, 2013.

[26] D. K. Mandal, A. Criscione, C. Tropea and A. Amirfazli, "Shedding of Water Drops from a Surface under Icing Conditions," *Langmuir,* vol. 31, pp. 9340-9347, 2015.

[27] P. Wang, A. Anderko and R. D. Young, "Modeling surface tension of concentrated and mixed-solvent electrolyte systems," *Industrial and Engineering Chemistry Research,* vol. 50, no. 7, pp. 4086-4098, 2011.

[28] J. D. Smith, R. Dhiman, S. Anand and E. Reza-Garduno, "Droplet mobility on lubricant-impregnated surfaces," *Soft Matter, ,* vol. 9, pp. 1772-1780, 2013, .

[29] P. &. M. R. Bradshaw, "Design Rules for Small Low-Speed Wind Tunnels," *The Aeronautical Journal of The Royal Aeronautical Society,* vol. 73, no. 1, pp. 443-449, 1979.

[30] Y.-H. Wang, C.-Y. Lee and C.-M. Chiang, "A MEMS-based Air Flow Sensor with a Free-standing Microcantilever," *Sensors ,* vol. 7, no. 10, pp. 2389-2401, 2007.

[31] C.-A. Jong, T.-S. Chin and W. Fang, "micro-cantilever method," *Thin Solid Films,* vol. 401, pp. 291-297, 2001.

[32] F. Shen, P. Lu, S. J. O'Shea, K. H. Lee and T. Y. Ng, "Thermal effects on coated resonant microcantilevers," *Sensors and Actuators, A: Physical,* vol. 95, no. 1, pp. 17-23, 2001.

[33] K. M. Hansen and T. Thundat, "Microcantilever biosensors," *Methods,* vol. 37, no. 1, pp. 57-64, 1 9 2005.

[34] K. Chien-Yuan., T. Chun-Ta., H. Ming-Chin. and L. Chi-Ming., "Wind Tunnel Studies of a Pedestrian-Level Wind Environment in a Street Canyon between a High-Rise Building with a Podium and Low-Level Attached Houses.," *Energies,* vol. 8, no. 10, pp. 10942-10957, 2015.

[35] Y. Watanabe, S. Suzuki, M. Sugihara and Y. Sueoka, "An experimental study of paper flutter," *Journal of Fluids and Structures,* vol. 16, no. 4, pp. 529-542, 1 5 2002.

[36] L. Yu., H. Cheng., Y. Zhan. and S. Li., "Study of parachute inflation process using fluid–structure interaction method," *Chinese Journal of Aeronautics,* vol. 27, no. 2, pp. 272-279, 2014.

[37] M. Bastankhah and F. Porté-Agel, "Wind tunnel study of the wind turbine interaction with a boundary-layer flow: Upwind region, turbine performance, and wake region," *Physics of Fluids,* vol. 29, no. 6, p. 065105, 2017.

[38] R. Howell., N. Qin., J. Edwards. and N. Durrani, "Wind tunnel and numerical study of a small vertical axis wind turbine,," *Renewable Energy,* vol. 35, no. 2, pp. 412-422, 2010.

[39] J. B. Barlow, W. H. Rae and A. Pope, Low-speed wind tunnel testing., 3 ed., John Wiley and Sons, Inc., 1999, pp. 61-68.

[40] B. Munson, D. Young, O. T.H. and &. H. W.W, Fundamental of Fluid Mechanics, John Wiley & Sons, Inc., 2010, pp. 316,347,396.

[41] B.B.Daly, Woods Practical Guide To Fan Engineering, Colchester: Woods of Colchester Limited, 1992, pp. 88-93,297.

[42] R. Basak, D. Mitra and A. Mazumdar, "Design of Various Components of an Open Circuit Blower Tunnel without Exit Diffuser.," *International Journal of Advances in Science and Technology,* vol. 2, no. 6, pp. 88-93., 2011.

[43] J. Bell and R. Mehta, "Contraction Design for Small Low-Speed Wind Tunnels," Stanford University, Stanford, 1988.

[44] R. Mehta, "The aerodynamic design of blower tunnels with wide-angle diffusers," *Progress in Aerospace Sciences,* vol. 18, pp. 59-120, 1979.

[45] J. H. Bell and R. D. Mehta, "Boundary-layer predictions for small low-speed contractions," *AIAA Journal,* vol. 27, no. 3, pp. 372-374, 1989.

[46] A. S. Nezhad, M. Ghanbari, C. G. Agudelo, M. Packirisamy and R. B. Bhat, "PDMS Microcantilever-Based-Flow Sensor Integration for Lab-on-a-Chip," *IEEE SENSORS JOURNAL,* vol. 13, no. 2, pp. 601-609, 2013.

[47] L. L. Bucciarelli, "Deflections due to Bending.," in *Engineering Mechanics for Structures.*, Massachusetts, Dover publications, 2004, p. 268.

[48] S. P. Thampi, R. Adhikari and R. Govindarajan, "Do liquid drops roll or slide on inclined surfaces?," *Langmuir,* vol. 29, no. 10, pp. 3339-3346, 2013.

[49] C. Lv, C. Yang, P. Hao, F. He and Q. Zheng, "Sliding of water droplets on microstructured hydrophobic surfaces," *Langmuir,* vol. 26, no. 11, pp. 8704-8708, 2010.

[50] E. B. White and J. A. Schmucker, "A Runback Criterion for Water Drops in a Turbulent Accelerated Boundary Layer," *Journal of Fluids Engineering,* 2008.

[51] A. J. B. Milne and A. Amirfazli, "Drop Shedding by Shear Flow for Hydrophilic to Superhydrophobic Surfaces," *Langmuir,* vol. 25, no. 24, pp. 14155-14164, 2009.

[52] S. Madani and A. Amirfazli, "Oil drop shedding from solid substrates by a shearing liquid," *Colloids and Surfaces A: Physicochemical and Engineering Aspects,* vol. 441, pp. 796-806, 2013.

[53] Z. Keshavarz-Motamed, L. Kadem and A. Dolatabadi, "Effects of dynamic contact angle on numerical modeling of electrowetting in parallel plate microchannels," *Microfluidics and Nanofluidics,* vol. 8, no. 1, pp. 47-56, 2010.

[54] A. D. Schleizer and R. T. Bonnecaze, "Displacement of a two-dimensional immiscible droplet adhering to a wall in shear and pressure-driven flows.," *J. Fluid Mech,* vol. 383, pp. 29-54, 1999.

[55] P. Dimitrakopoulos, "Deformation of a droplet adhering to a solid surface in shear flow: Onset of interfacial sliding," *J. Fluid Mech,* vol. 580, pp. 451-466, 2006.

[56] P. Dimitrakopoulos, "Gravitational effects on the deformation of a droplet adhering to a horizontal solid surface in shear flow," *Physics of Fluids,* vol. 19, no. 12, p. 122105, 2007.

[57] M. Miwa, A. Nakajima, A. Fujishima, K. Hashimoto and T. Watanabe, "Effects of the surface roughness on sliding angles of water droplets on superhydrophobic surfaces," *Langmuir,* vol. 16, no. 13, pp. 5754-5760, 2000.

[58] F. Peters and D. Arabali, "Interfacial tension between oil and water measured with a modified contour method," *Colloids and Surfaces A: Physicochemical and Engineering Aspects,* vol. 426, pp. 1-5, 2013.

[59] P. Dimitrakopoulos and J. J. L. Higdon, "Displacement of fluid droplets from solid surfaces in low-Reynolds-number shear flows," *Journal of Fluid Mechanics,* vol. 336, pp. 351-378, 1997.

[60] I. V. Roisman, A. Criscione, C. Tropea, D. K. Mandal and A. Amirfazli, "Dislodging a sessile drop by a high-Reynolds-number shear flow at subfreezing temperatures," *Physical Review E,* vol. 92, no. 2, p. 023007, 2015.

[61] D. Daniel, J. V. I. Timonen, R. Li, S. J. Velling and J. Aizenberg, "Oleoplaning droplets on lubricated surfaces," *Nature Physics,* vol. 13, pp. 1020-1025, 2017.

[62] F. Schellenberger, J. Xie, N. Encinas, A. Hardy and M. Klapper, "Direct observation of drops on slippery lubricant-infused surfaces," *Soft Matter,* vol. 11, pp. 7617-7626, 2015.

[63] A. R. A. Khaled and K. Vafai, "Analysis of detection enhancement using microcantilevers with long-slit-based sensors," *Sensors,* vol. 13, no. 1, pp. 681-702, 2013.

[64] A. R. A. Khaled, K. Vafai, M. Yang, X. Zhang and C. Ozkan, "Analysis, control and augmentation of microcantilever deflections in bio-sensing systems," *Sensors and Actuators B: Chemical,* vol. 94, no. 1, pp. 103-115, 2003.

[65] A. R. A. Khaled and K. Vafai, "Analysis of Deflection Enhancement Using Epsilon Assembly Microcantilevers Based Sensors," *Sensors,* vol. 11, no. 10, pp. 9260-9274, 2011.

[66] G. Zhang, L. Zhao, Z. Jiang, S. Yang, Y. Zhao, E. Huang, X. Wang and Z. Liu, "Surface stress-induced deflection of a microcantilever with various widths and overall microcantilever sensitivity enhancement via geometry modification," *Journal of Physics D: Applied Physics,* vol. 44, no. 42, p. 425402, 2011.

[67] R. Bhat, "Natural frequencies of rectangular plates using characteristic orthogonal polynomials in rayleigh-ritz method," *Journal of Sound and Vibration,* vol. 102, no. 4, pp. 493-499, 1985.

[68] Y. Park, M. Jeong, S. B. Lee, J. A. Antonino-Daviu and M. Teska, " Influence of blade pass frequency vibrations on MCSA-based rotor fault detection of induction motors," *IEEE Transactions on Industry Applications,* vol. 53, no. 3, pp. 2049-2058., 2017.

Appendix I

Operating Procedure to fabricate PDMS micro-cantilever beam

Preparation of thin PDMS layer (Thickness of PDMS layer = thickness of micro-cantilever beam)

1. Select the suitable silicon wafer 4" or 6"
2. Silanaize the silicon wafer

Silanization of silicon wafer is done by adding two drops of silane solution over silicon wafer and place it over hot plate for two hours at 60°. Cover the silicon wafer during the process

3. Measure the weight of PDMS required to prepare the Thin PDMS layer.

Find the mass of PDMS mixture using following Equation

$$m_{PDMS}=\frac{\pi x\, d_{sw}^{2} x\, t_{PDMS}\, x\, \rho_{PDMS}}{4}$$

Where, $\mathbf{m_{PDMS}}$ is mass of PDMS mixture (g), $\mathbf{d_{sw}}$ is diameter of the silicon wafer (mm), $\mathbf{t_{PDMS}}$ is required thickness of PDMS (μm) and $\boldsymbol{\rho_{PDMS}}$ is density of PDMS mixture (~ 965 kg/m^3)

Example: Mass of PDMS mixture required to fabricate 240 μm PDMS layer using 4" Silicon wafer

d_{sw} = 4x 25.4 = 100.56 mm

ρ_{PDMS} = 965 kg /m^3

t_{PDMS} = 240 μm

$$W_{PDMS}=\frac{\pi\,(100.56x10^{-3})^{2}\,240x\,10^{-6}x\,965\,x\,10^{3}}{4}=1.84 \text{ grams}$$

Total weight of PDMS mixture = 1.84 grams.

PDMS mixture is 10:1 ratio of base to curing agent

Weight of base agent = 1.84 x (10/11) = 1.67 grams

Curing agent = 1.84x (1/11) = 0.167~ 0.17 grams

4. Measure the base and curing agent individually and mix thoroughly using a glass rod ensuring uniform mixing.
5. After mixing, place the container inside the desiccator to remove air bubble.

6. Switch on the vacuum pump and run for 10-15 mins approx. (To prevent the pump from overheating switch on/off the pump in pulses of 5 mins)
7. After ensuring no visible air bubble (transparent liquid) place the silicon wafer in the spin coating machine. Make sure the silicon wafer is placed symmetrically over the spin coating machine.
8. Select the RPM of spin coater using thickness vs RPM curve
9. After spin coating place the silicon wafer inside the hot air oven at 80°, for baking, approximately 8 hours.
10. Cut the PDMS layer to desired dimension and attach to PDMS base

To prepare colored PDMS mix suitable dye at step 4.

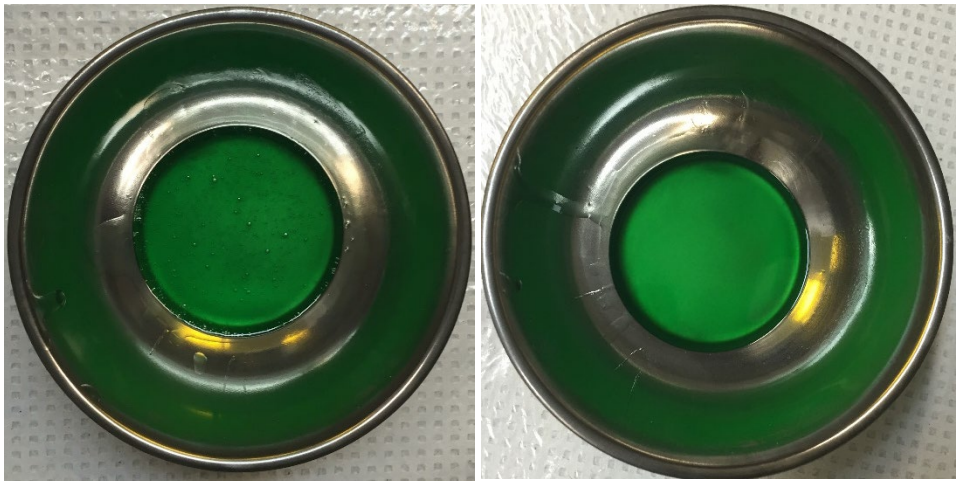

(a) (b)

Figure A1: Colored PDMS mixture (a) before desiccation (b) after desiccation for 10 mins